Activation of Dioxygen on Isolated Transition Metal Ions in Nitrogen-Doped Carbon

---

A

Dissertation

Presented to

the faculty of the School of Engineering and Applied Science

University of Virginia

---

in partial fulfillment

of the requirements for the degree

Doctor of Philosophy

by

Colby A. Whitcomb

August 2023

APPROVAL SHEET

This

Dissertation

is submitted in partial fulfillment of the requirements
for the degree of

Doctor of Philosophy

Author: Colby A. Whitcomb

This Dissertation has been read and approved by the examing committee:

Advisor: Robert J. Davis

Advisor:

Committee Member: Christopher Paolucci

Committee Member: William Epling

Committee Member: Gary Koenig

Committee Member: T. Brent Gunnoe

Committee Member:

Committee Member:

Accepted for the School of Engineering and Applied Science:

Jennifer L. West, School of Engineering and Applied Science

August 2023

Abstract

The activation of O_2 is an important process for a variety of reactions from the electrochemical reduction of O_2 for fuel cells to thermochemical oxidative dehydrogenation reactions. Platinum particles supported on carbon are often reported to be highly active catalysts for these reactions, but their high costs limit their large-scale use. This high cost has prompted research into atomically efficient transition metal ions (M) doped into a conductive nitrogen-carbon support (N-C). These M-N-C catalysts have shown promise for comparable activity on the same magnitude as platinum electrodes for the electrochemical oxygen reduction reaction (ORR) and Pt nanoparticles for the thermochemical oxidative dehydrogenation of alcohols. Although the M-N-C catalysts facilitate O_2 activation for both thermal and electrochemical reactions, the coordination environment surrounding the active site and the mechanism for O_2 activation remain elusive. To avoid the complications of solvent and applied potential, CO oxidation and 2-propanol oxidative dehydrogenation were used as probe reactions in this dissertation.

A catalyst with isolated Co ions in nitrogen-doped carbon (Co-N-C) was synthesized and imaged by scanning transmission microscopy, confirming the presence of isolated Co ions. The Co-N-C catalyst converted CO at temperatures as low at 198 K, with a negative apparent activation energy at low temperatures, whereas low temperature catalytic activity was not observed for the other Co-containing materials (mixed Co oxide, Co on carbon black, and Co on silica). Comparison of the reaction orders measured over the Co-containing catalysts revealed nearly first-order behavior in both CO and O_2 over the Co-N-C catalyst compared to zero order in CO and positive order in O_2 for the other Co-containing catalysts. Isotope transient analysis indicated the surface coverage of reactive intermediates leading to CO_2 on Co-N-C was low relative to CO and the turnover frequency was high (exceeding 0.3 s^{-1}), even at 273 K.

Quantum chemical density functional theory (DFT) calculations indicated weak binding of both CO and O_2 to the Co ion surrounded by 4 pyridinic N atoms. Molecular dynamic simulations with CO and O_2 resulted in a plausible reaction path for CO oxidation whereby CO assisted the activation of O_2 with the carbon support without involving a redox cycle on the Co ion. The reaction path was consistent with the experimental kinetic parameters for low temperature CO oxidation on the Co-N-C catalyst.

A quantum chemical DFT screening of other M-N-C catalysts for similar interactions between the transition metal and reactants CO and O_2 suggested that the transition metals in the same column as Co are potentially good catalysts for low temperature O_2 activation. Thus, a Rh-N-C catalyst was synthesized and tested for CO oxidation activity. Steady-state CO oxidation at low temperature over Rh-N-C had positive reaction orders in both CO and O_2 as well as a nearly zero apparent activation energy, whereas supported Rh nanoparticles were not active at these low temperatures. The experimental observation of low temperature CO oxidation catalyzed by Rh-N-C validates the results from the DFT screening study.

The gas phase oxidative dehydrogenation of 2-propanol was also explored on Co-N-C. High initial activity for the Co-N-C catalyst at 473 K sharply deactivated to a steady-state rate that was similar to a metal free N-C catalyst. The similar steady-state rates of a Co-containing material and a Co-free material indicate that Co sites may not turn over at the steady state. The reaction was also tested in aqueous solvent and similar to the gas phase reaction, the Co-N-C catalyst had high initial activity but deactivated completely by 15 min. The observed performance of highly active species (associated with Co) and the less active N-C (Co-free) warrant further study.

Acknowledgements

I would thank my doctoral advisor, Dr. Robert J. Davis. He has taught me so much as a researcher while allowing me space to grow and explore. I am grateful for the many opportunities he has given me to learn, be it through national lab trips or the lab environment he has cultivated. His guidance has kept me motivated in research and allowed me to enjoy my time in lab. I would also like to thank Dr. Christopher Paolucci for his patience and guidance in teaching me how to do quantum chemical calculations. He has become a great mentor and I really appreciate the opportunities for growth he provided me. Before I came to the University of Virginia (UVA), I always said I was going to avoid computational research. Five years later and a lot of skills learned and I am happy to report that it can be very interesting and almost fun. I would also like to thank the other members of my committee, Dr. William Epling, Dr. Gary Koenig, and Dr. Brent Gunnoe for their helpful discussions.

I have had the privilege to work with many amazing collaborators during my doctoral studies, including Dr. Raymond R. Unocic at Oak Ridge National Laboratory (BNL), Dr. Eli Stavitski at Brookhaven National Lab, and Dr. Helge Heinrich at the Nanomaterial Characterization Facility at the UVA. I would also like to thank the amazing UVA Chemical Engineering department staff, especially Jennifer Davis, Jen Lamb, and Ricky Buchanan who have facilitated so much of the day-to-day work. It has also been great to interact with many of the graduate student coordinators and counselors during my time at UVA, including Dr. Amy Clobes, Dr. Priya Date, and Elizabeth Ramirez-Weaver.

I have been very lucky to be part of a tremendous research community at UVA. I would like to thank all of the Davis lab members, both past and present, who have supported and taught me so much. It is great to have such a supportive group that has continued to stay in touch even

when they graduate. Dr. Jiahan Xie, Dr. James Kammert, and Tyler Prillerman were instrumental in getting me set up in the lab and teaching me the fundamentals of all the work that I did in this dissertation. Dr. Gordon Brezicki is acknowledged for his patience in teaching me how to work 8-ID at Brookhaven National Lab. I would like to thank Dr. Lu Yang for being a supportive mentor to me and being a great resource in lab. His questioning is some of the hardest I have faced, and I am a better researcher because of it. I would like to thank Dr. Naomi Miyake for being a great friend and always supporting me when I was stressed or needed to complain about failed experiments. I have also learned and grown with current students Konstantin Mamedov, Dipesh Advikari, Dr. Weijie Zhang, and Dr. Pardeep Kumar. You have made the last couple of years some of the best of my life.

I also would like to acknowledge the whole catalysis community at UVA. The Paolucci group has had incredible patience for my antics and the constant bombardment of questions that I hurled at them when learning how to do DFT calculations. I would especially like to thank Anna Sviripa for running a molecular dynamic simulation that opened a lot of doors for the work in this dissertation. Dr. Kevin Gu, Silvia Marino, and Sugandha Verma have also been great collaborators and I have always enjoyed our discussions (and trips to BNL!). I am also very glad to have been able to learn with my classmates Keka Mandal and Natalia Diaz Montenegro.

The people at UVA have really made my time here special. My classmates at UVA have become some of my best friends and have constantly supported and motivated me during my time here. I want to thank my roommates, Vince Gray, William Hart, and Eric Holmgren, for always being down to play board games or disc golf. I would like to thank Dr. Mara Kuenen and Jamie Soderlund (and Avery!) for their constant friendship. I would like to thank Dr. Erica Hui and Dr. Jenna Sumey for always being down to eat lunch. Dr. Jenna Sumey, thank you for all of the long

walks where we discussed the highs and lows of grad school. Thank you to Natalie Smith, Madison Mann, and Greg Grewal for all the game nights, hangouts, and good times. I would also like to thank Dr. Naomi Miyake, Dr. Erica Hui, Dr. Zack Young, Dr. Devanshi Gupta, Dr. Kate Dagnall, Dr. Lucas Kimerer, and Sam Crowl for all of the BBQs and winery/brewery trips.

Lastly, I could not have done this work without the love and support of my family. My parents, Edward and Paula Whitcomb, have supported me so much as I have pursued my degrees. They provide a constant supply of confidence and have instilled in me the importance of both education and service. I am so appreciative of all the time you have spent caring for me and teaching me through my life. I also want to thank my siblings, Curtis and Kayla, who have been so kind in supporting me as I moved away from New England. I am proud of your accomplishments and cannot wait to see where life takes you. Finally, to my significant other, Aditi Gourishankar, thank you for being there for me this last year. It is always comforting to know you are always there for me and are down to binge watch TV or go on nice hikes around Virginia. I cannot wait to watch your journey in getting your doctorate!

The work in this dissertation was also supported by the National Science Foundation under grant # CBET-1802482 with partial funding for the computational hours supported by the donors of the American Chemical Society Petroleum Research Fund.

Contents

List of Figures

List of Tables

Chapter 1 Introduction

1.1 Importance of Dioxygen Activation

The activation of O_2 is a critical step in many heterogeneous oxidative processes such as some thermocatalytic and electrocatalytic reactions.[1-8] The importance of O_2 activation has only increased due to new demands for storing renewable energy, producing fuels, and converting these fuels into electricity. Electrochemical fuel cells have been investigated intensively since they can operate at efficiencies exceeding those of combustion engines with small levels of emission.[9] Specifically, the proton-exchange fuel cell consists of a negative electrode (anode) and positive electrode (cathode) with an electrolyte in between. The cathodic process involves the reduction of O_2 to H_2O or H_2O_2 (Fig. 1). The electrochemical oxygen reduction reactions (oxygen reduction reaction (ORR) and oxygen evolution reaction (OER)) on the cathode are sluggish and inefficient relative to the hydrogen evolution reaction (HER) on the anode due to the difficulty in O_2 activation and oxide removal.[10-12] The difficulty in O_2 activation has focused research on increasing the efficiency of the cathode.[10-12] The highest reported activity for the ORR is on platinum catalysts supported on conductive carbon substrates.[2, 8] Although highly active and efficient, the high costs of Pt limits large scale industrial and consumer applications. These Pt catalysts typically sinter into larger nanoparticles on the carbon support (Pt/C) under reaction conditions, which renders many Pt atoms inaccessible and thus causes inefficient use of the already expensive metal.[13-16] Furthermore, the often-acidic environment of the electrolyte has been shown to negatively impact the Pt activity for the ORR.[8] Competitive adsorption of acids such as HCl, HBr, HI and inorganic acids such as sulfuric and phosphoric diminishes the activity of the catalysts.[8] These problems

surrounding using Pt catalysts have motivated exploration of earth-abundant elements in tunable chemical environments for stable and efficient O_2 activation.

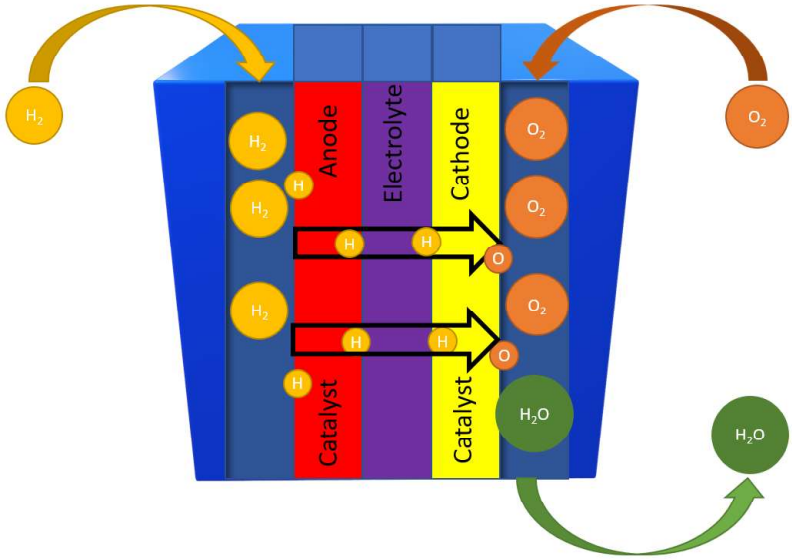

Figure 1.1. Activation of O_2 occurs on the cathode during the ORR (yellow portion of the figure).

1.2 Metal Ions in Nitrogen-Doped Carbon

1.2.1 Introduction to Materials with Metal Ions in Nitrogen-Doped Carbon

Although platinum group metals (PGM) are still regarded as having the highest activity for reactions involving molecular oxygen, newer earth abundant catalysts have recently been developed with transition-metal atoms (M) deposited onto nitrogen-doped carbon (N-C).[17] The most commonly synthesized M-N-C catalysts use first-row transition-metal ions such as Fe, Co, and Cu but a wide variety of transition metal ions in nitrogen-doped carbon have been synthesized.[17-19] The synthesized graphene-supported single-atom catalysts include Au, Co, Fe, Mn, Ni, Pd, Pt, Ru, and Rh.[17] These M-N-C catalysts are the heterogeneous analog of the

homogeneous porphyrin catalysts (for example, a Co phthalocyanine is depicted in Figure 1.2 a) that are abundant in nature and known for their tunable redox potentials and ability to catalyze reactions involving O_2.[20, 21] Although the porphyrin complexes have shown activity for O_2 activation reactions, heterogeneous catalysts are preferred for industrial applications. Heterogeneous catalysts account for ~ 80 % of the industrial catalytic processes since they are generally more robust and are easier to recover than their homogeneous counterparts.[22] The desire to make heterogeneous versions of enzymatic and homogeneous catalysts have led to the deposition of porphyrin structures onto the surface of carbon.[23] These anchored M-N-C catalysts have gained stability through the nitrogen-carbon substrate and have resistance to harsh redox environments.[21] Beyond being stable, the tunability of these metal centers with ligands in different environments is a feature that researchers hope to utilize to catalyze a wide variety of reactions.[24, 25] Indeed, these metals can catalyze reactions such as the ORR,[26] oxidation of alcohols,[27-31] decomposition of formic acid,[32, 33] and CO_2 reduction reaction.[34, 35] Moreover, some transition metals such as Co and Fe doped in N-C have promise in replacing Pt/C catalysts.[36, 37] The synthesis of these catalysts, however, leads to many issues in determining the active species and quantifying the number of active sites.

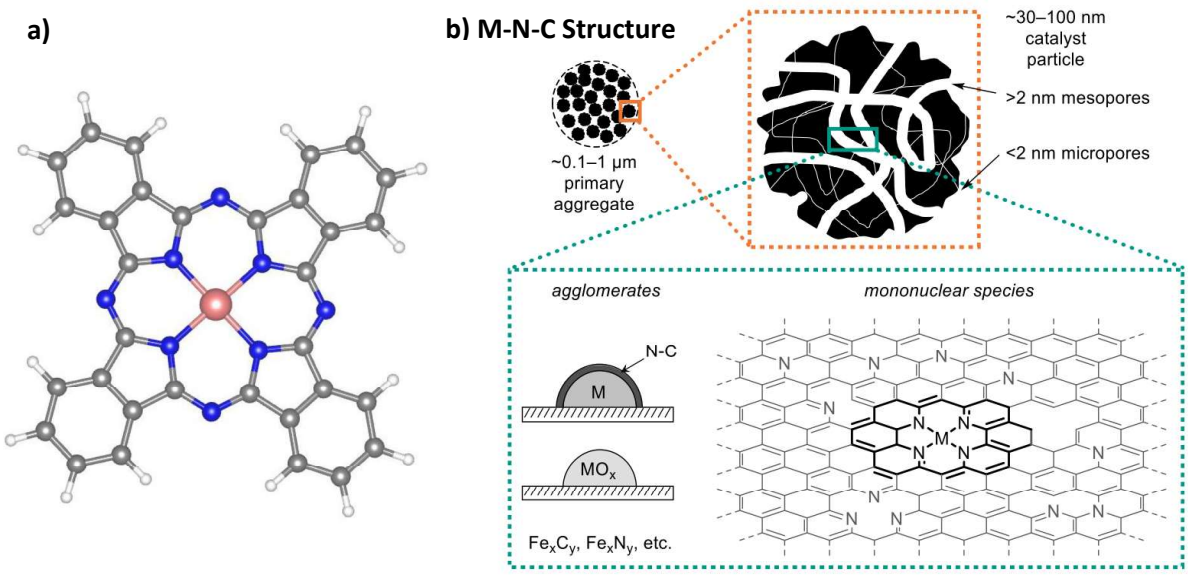

Figure 1.2. a) An example of a Co phthalocyanine complex (CoPc). b) An example of the structure often seen after the synthesis of M-N-C catalysts.
Panel a was generated using VESTA with the structure a reference to one described in Ref. 38.[38] Panel b is reprinted with permission from *Chem. Rev.* **2023.** *123* (9), 6233-6256. Copyright 2022 American Chemical Society.[19]

1.2.2 Synthesis of Metal Ions in Nitrogen-Doped Carbon Materials

Many different synthesis methods have been used to make M-N-C catalysts with different structures and compositions.[39] Figure 1.2 b shows a common visual of the materials with a sheet of carbon with defect sites and metal doping.[19] The use of a thermal treatment is the most common component of a synthesis method to form these M-N-C materials.[19] The thermal treatment process involves the use of high temperatures between ~ 873 - 1273 K under a flow of inert gas (such as Ar or N_2) or a reactive gas (such as NH_3 or H_2) to decompose a mixture of transition metal salt in the presence of nitrogen precursor deposited onto a carbon substrate. The high temperature causes volatilization of the decomposed precursors, which incorporates the components into the carbon structure. The high temperature results in an unpredictable heterogeneity of structures formed in the material. This heterogeneity causes catalysts with similar metal weight loadings to exhibit

different reaction rates, indicating that not all sites formed have the same activity.[40] For example, the effect of thermal treatment temperature on the activity for both Co and Cu N-C materials was studied and revealed that there was an optimal temperature for decomposition and active site formation.[40] Beyond just site distributions, the volatilization of metal complexes often leads to the aggregation of transition metal ions into nanoparticles.[18, 19, 41] Without the removal of the nanoparticles via techniques such as acid leaching, further characterization and active site determination becomes difficult.[19, 40, 42] Removal of the nanoparticles is imperative since both metal nanoparticles and isolated sites have been proposed to be active.[43, 44] To remove nanoparticles, a post-treatment of these catalysts in acid is often used with a second high temperature thermal treatment to clean the surface and produce the final catalyst.[40, 45] Although these acid washed catalysts are often assumed to be devoid of accessible nanoparticles, the decomposition at high temperatures means it is possible that some nanoparticles become buried under the surface carbon layer even as pores are created in the carbon structure.[41, 46, 47] The resulting materials are both mesoporous[48] and microporous with sites that may also become inaccessible in the pores.[41, 46, 47] Nanotubes have been synthesized to avoid burying sites but these materials often still have nanoparticles on them after synthesis. [49-51] Further complications with nanotubes include possible ligand formation on the bottom of the sites when they are not anchored on other carbon planes.[49-51] In order to make more well-defined materials, other synthesis methods have been investigated.

Synthesis of M-N-Cs using templates and metal organic frameworks (MOFs) attempt to avoid site heterogeneity by making specific sites before thermal treatment.[52-54] This templating synthesis strategy involves using high temperature decomposition of MOFs, polymeric precursors, or sacrificial supports to form well defined sites. Templating with MOFs typically involves using

a sacrificial Zn species to spatially distribute transition metal ions before evaporating the lower boiling point Zn atoms at high temperature and subsequently decomposing the 3-D structure.[55, 56] Residual Zn from the synthesis complicates both characterization as well as kinetic studies since the activity can be the convolution of multiple transition metals.[56] Another variation of the templating synthesis method involves sacrificial templating with silica particles.[48, 57] The use of silica particles for templating requires HF to dissolve them in the post treatment.[57] These catalysts are ideally free of buried species and have a higher amount of exposed sites.[57] However, the left-over silica and the leaching of active sites from the carbon structure can cause further problems with characterization or activity respecitvely.[57] Similar to the silica templating method, sacrificial templates can be used to localize the transition metal on the surface of a nitrogen-containing template before thermal treatment to decompose the structure.[58] This method still suffers from the same nanoparticle formation as other methods involving thermal treatments but has a benefit in specific nitrogen coordination of the transition metal with the aniline backbone structure.[58] Regardless of the way that these catalysts are synthesized, it is important to characterize them to help understand their site structure and quantify the number of sites.

1.2.3 Characterization of M-N-Cs

As previously discussed, the heterogeneity of M-N-C catalysts complicates the exploration of the active site for reactions involving O_2 activation. Thus, many characterization methods are used to understand the nature of active sites. For example, high-angle annular dark field scanning transmission electron microscopy (HAADF-STEM) is often used to understand the isolated nature of transition metals since there is high z-contrast between the "bright" heavier metal atoms and the "darker" lighter N and C atoms.[59] Elemental mapping and analysis techniques such as electron

dispersive X-ray (EDX) and electron energy loss spectroscopy (EELS) have been used in conjunction with STEM to investigate the composition of the M-N-C catalysts, the isolated nature of the transition metal, and the N content surrounding the metal atom.[30] Although useful for investigating the presence of isolated metal ions with N nearby, it is difficult to confirm the coordination number of N around the singular metal atoms through elemental mapping. The low resolution complicates the differentiation of N or C moieties coordinating to the metal atom and the quantification of these ligands.[60, 61] The difficulty in understanding the bulk composition of isolated transition metal sites requires that multiple spectroscopic techniques be utilized. Thus, even when confirming the isolated nature of the sites with STEM, groups still utilize X-ray absorption spectroscopy (XAS) to understand the coordination environment around the metal ion.

Both the near edge (XANES) and extended X-ray absorption fine structure (EXAFS) regions of XAS are often collected for the K or L_3 edges of transition metals to assist in understanding the coordination environment. The coordination environment is analyzed by fitting the first shell scattering path of the M with light elements N/C/O. It is difficult to differentiate the light element scattering paths due to their small backscattering amplitudes.[62] Thus when fitting the first-shell that is commonly found in the EXAFS region of M edges for M-N-C catalysts, the light element could be N, C, or O. The N atoms are most commonly associated with the scattering due to the presence of excess amounts of N needed to for site formation being present when synthesizing M-N-Cs. The MN_x species (where X is the number of N atoms coordinated to the M) is therefore reported as the most abundant species formed during high temperature thermal treatment.[24, 40, 63] Phthalocyanine structures have been used as a standard for fitting the first-scattering shell due to their structure being similar to the sites formed during synthesis of M-N-Cs and thus could be helpful for understanding the coordination number.[40] A coordination number

greater than 3 is typically reported and thus the MN_4 motif is often assumed to be the most abundant site for M-N-C catalysts.[24, 64, 65] Investigations of the active sites usually begin with the MN_4 site even if a minority site may be more active. Although this M-N path is typically the only scattering path observed, occasionally a first shell scattering path for M-M moieties is present if nanoparticles have not been leached.[40] After leaching the catalyst, this M-M scattering path is often absent from EXAFS, which may indicate the absence of or the small contributions of nanoparticles.[40] However, since XAS is a bulk technique, the presence of nanoparticles and other minority sites may be missed. The focus of activity still remains on the MN_4 sites with another spectroscopic technique such as X-ray photoelectron spectroscopy (XPS) often used to determine the type of nitrogen in the material, such as pyridinic, pyrrolic, and graphitic.

Various groups have utilized XPS to understand the effect of the N ligands on the transition metal ion.[66-69] Since N could be incorporated into the carbon substrate in multiple modes, XPS can assist in determining which are present. For example, Wu and coworkers investigated the presence of graphitic, pyrrolic, and pyridinic N-types by changing the thermal treatment temperature when synthesizing Fe based Fe-N-C catalysts for ORR, as reported in Fig. 1.3.[56] By increasing the temperature, they apparently changed the formation rate of graphitic N and the total N content while keeping Fe content the same after each thermal treatment temperature, therefore ensuring sufficient quantities of the commonly reported pyridinic and pyrrolic N needed to stabilize the Fe.[67, 70] The increased activity with a higher presence of N indicates that there may be another role of the N in activating O_2 beyond forming the isolated sites. Further study into the role of metal-free N-C structures is therefore needed. Recent studies have probed the role of N-C for hydrodeoxygenation of 5-hydroxymethylfurfural to 2,5-dimethylfuran but it was discovered that part per million levels of iron were in the material from the purchased activated carbon and was

likely contributing the most to the activity of the catalyst.[66] Although the presence of metals can complicate the investigation of activity for metal-free N-C, there are many groups that propose interesting O_2 activation paths and sites for activation.[71-76] The investigation of N-C sites is beyond the scope of this dissertation where the activation of O_2 on isolated transition metal sites is explored. Although it has been difficult to understand the presence of the metal sites after synthesis, many groups have attempted to quantify the number of sites and determine the mechanism for O_2 activation.

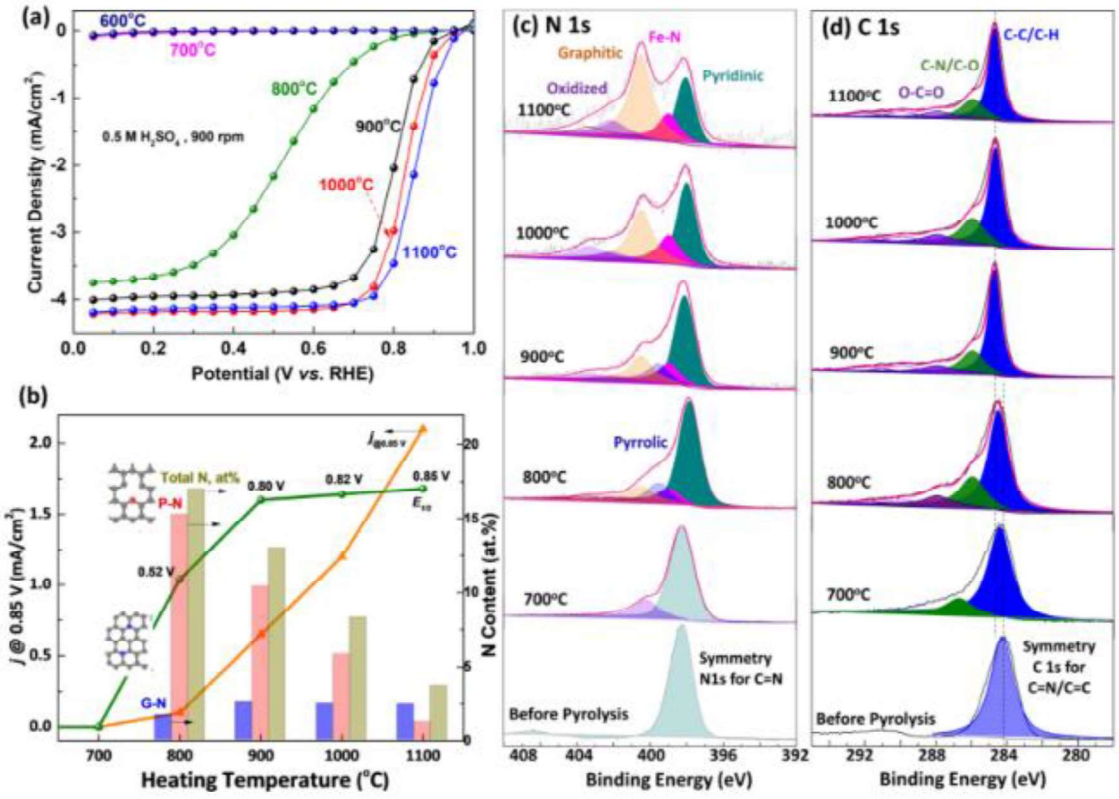

Figure 1.3. Quantification of N-types from XPS are used to normalize ORR activity to determine the effect of the N-types on the activity of catalysts for the ORR.
Reprinted with permission from *J. Am. Chem. Soc.* **2017.** *139* (40), 14143-14149. Copyright 2017 American Chemical Society.[56]

1.3 Determining the Active Site and Mechanism for O_2 Activation on M-N-Cs

The focus of this introduction has mainly been on the extensive electrochemical ORR work, which these catalysts were initially designed for, but features of both the electrocatalytic and aerobic oxidation reactions are similar. In both cases, O_2 needs to bind and reduce on the catalyst surface via protons and electrons from an electrode (ORR) or an organic molecule from the substrate (aerobic oxidation). For the thermochemical aerobic oxidation reaction, two mechanisms have been proposed and are presented in Fig. 1.4.[19] One of these is an inner-sphere reaction (ISR) where there is direct interaction between the organic molecule and O_2.[19] The ISR has been invoked for transformations on various molecular structures with N and O ligands around the transition metal.[77, 78] These molecular structures lack the conductive carbon support and therefore complete the entire reaction at their metal center.[77-80] Although it is clear that molecular catalysts often complete an ISR, heterogeneous catalysts are more complicated. They could complete the first mechanism described (ISR) or an independent redox half-reaction (IHR) where the organic molecule is oxidized separate from the reduction of O_2.[19] For example, two independent studies on benzyl alcohol oxidative dehydrogenation over M-N-C catalysts found different results.[40, 81] One study found that the catalyst surface was saturated by O_2 but was inhibited by the alcohol and product aldehyde.[81] These findings led the authors to invoke an ISR path wherein the competitive adsorption of the O_2 and alcohol to the same site led to inhibition.[81] Conversely, another group found that both alcohol and O_2 had saturated the surface and could not differentiate whether it was occurring at the same site.[40] Another reaction system studied both of the reaction paths (ISR vs IHR) during the aerobic oxidation of hydroquinone (HQ) on Fe-N-C and Co-N-C materials in acidic media.[82, 83] Two different setups were used to probe the reaction path. One involved a suspended slurry in a semibatch reactor while the other involved coating

Nafion-bound film attached to a glassy electrode without applied potential. While the slurry-phase conditions resulted in positive order behavior O_2, the HQ order of reaction was ~0. This zero order dependence pointed to an ISR type path where HQ has high surface coverage and supports direct hydrogen-atom transfer from HQ to O_2. Conversely, for the Nafion-bound system, the Nafion seems to lower the HQ adsorption equilibrium constant, which disfavors the ISR mechanism, as exemplified by more positive order in HQ and near zero order behavior for O_2. While the ISR mechanism may still be applicable to both, the Nafion evidently hindered the ISR mechanism.[19, 82] The complicating effects of liquid phase in all of these examples indicates that gas-phase systems could be better systems for investigating the active sites and mechanism for O_2 activation.

Many of the reactions in the presence of M-N-C catalysts are performed in the liquid phase where additives have been used to try to quantify the active sites.[19, 40, 84, 85] For example, CO has been used to reversibly poison Fe-N-C catalysts during the ORR in 0.5 M H_2SO_4.[84] This poisoning did not completely inhibit the reaction since different sites had various binding energies of CO. Other poisoning experiments have involved cyanide and NO^- stripping, but these were complicated by the overcounting of non-metal sites.[86] Recently, batch reactions used for the oxidative dehydrogenation of benzyl alcohol on M-N-C catalysts revealed that there was an inhibitory effect by the production of benzoic acid and this acid product was useful in poisoning sites during the reaction.[40] However, the addition of benzoic acid did not linearly decrease the activity with higher moles of acid. Instead, the authors proposed that some sites were resistant to poisoning while others were poisoned by the acid.[40] Since not all sites are poisoned, other methods of site quantification are needed.

Strasser and co-workers utilized CO pulse cryo-chemisorption (193 K) to quantify active sites for ORR.[45, 68] As previously described, CO present during the ORR was found to deactivate

an Fe-N-C catalyst under ORR conditions.[84] Although deactivation occurs, the calculated binding energies of CO on M-N-Cs are typically lower than the platinum group metal catalysts that are known to be strong binders of CO and thus cryo-temperatures were chosen.[87] The work by Strasser and co-workers suggested that some metals such as Fe and Mn in N-C could bind CO while others such as Ni-N-C catalysts lacked uptake of CO.[88] Indeed, quantum computational modelling using density functional theory (DFT) from the Mavrikakis group has suggested that metal ions in graphene structures with two vacancy sites and 4 N atoms coordinated to the transition metal have significantly different binding energies of CO (0 to -260 kJ mol^{-1}).[89] Although these results suggest that quantification of active sites with CO on certain metal ions may be difficult, the unique properties of various transition metal ions in N-C have allowed a group to synthesize a catalysts for the oxidation of CO by O_2 to investigate a gas-phase oxidation reaction on the M-N-Cs.[90]

The gas-phase oxidation of CO with O_2 is a well-studied reaction without the complicating effects of solvents and applied potentials that are present with the liquid-phase oxidative dehydrogenation reactions or electrochemical ORR. The catalytic CO oxidation reaction was investigated for Fe-N-C, Co-N-C, and dual metal materials containing both Co and Fe (Co,Fe-N-C).[90] Interestingly, the Co-N-C and Co,Fe-N-C materials had observed activity at temperatures as low as 193 K.[90] The lack of low temperature activity for the Fe-N-C catalyst is consistent with high barriers calculated via DFT for the activation of O_2 on Fe-N-C materials with CO.[89] As evidenced by the activity of the Co-N-C, apparently the specific metal plays a role in the low temperature activity. Although the mechanism for the activity on the Co catalyst was not determined, the authors suggested that the co-doped catalyst utilized both adjacent transition metal sites to activate O_2 with each metal binding a CO or O_2 molecule.[90] The observed low temperature activity for some of these M-N-C catalysts is the main motivation for this dissertation, wherein we

hope to understand how these catalysts are able to activate O_2 at low temperatures. The investigation of these sites will require the use of DFT calculations to complement spectroscopic and experimental observations as the literature suggests a wide range of techniques are essential for validation of a mechanism and active site determination.

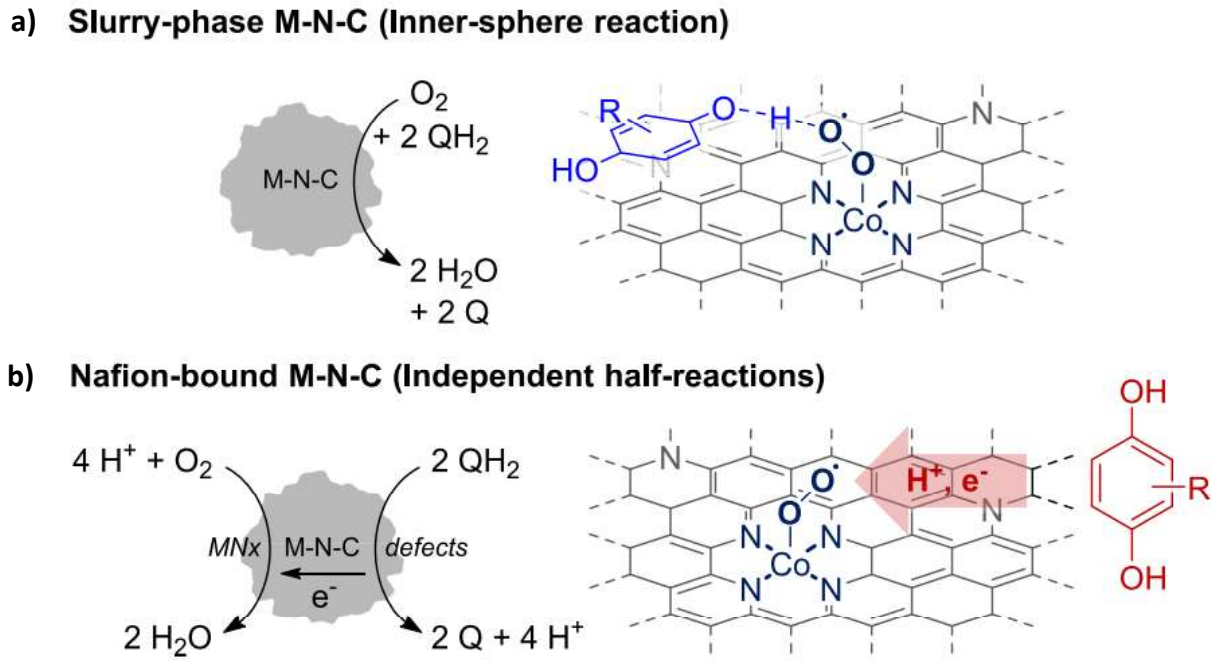

Figure 1.4. Inner-sphere reaction (a) and independent half-reactions (b) on a Co-N-C catalyst. Reprinted with permission from *Chem. Rev.* **2023.** *123* (9), 6233-6256. Copyright 2022 American Chemical Society.[19]

1.4 Quantum Chemical Density Functional Theory Studies of M-N-C Catalysts

The complexity of M-N-Cs and the difficulty in exploring the reaction paths spectroscopically has led many groups to model the active site for oxygen reduction reactions with quantum chemical DFT calculations for both thermochemical and electrochemical systems.[25, 89, 91-96] Calculations with DFT enable fundamental studies using well defined potential active centers to understand which structural motifs may allow for the most energetically favorable paths for O_2 reduction on M-N-C catalysts.[97] Examples of potential active sites can be found in Fig. 1.5.[84] The structures commonly investigated include edge, planar and defect sites. Formation energy studies on transition metals in N-doped carbon have found that N_x species tend to enable the binding of transition metals such as Fe to the support but that weaker binding occurs with decreased numbers of coordinated N. Edge sites are undercoordinated with only N_{0-2} and are likely to bind adsorbates stronger than planar sites since the undercoordination leads to strong interactions with the adsorbates.[84] Computational studies of the edge sites and defect sites have shown that the reactants do indeed bind stronger on these sites compared to planar sites.[84] In particular, a variety of sites were probed for the binding of intermediates (O_2) and known inhibitors (CO) of the ORR.[84] The authors of that study noted that FeN_4/C pyridinic and FeN_4/C pyrrolic planar sites had higher binding energies for CO compared to O_2 and thus would be inhibited by CO during ORR.[84] The stronger binding of CO compared to O_2 matched experimental data which had shown that ORR activity decreased after exposure to CO.[84] The stronger adsorption of reactants was proposed to restrict turnover due to the Sabatier principle.[84] Although experimental studies did not preclude other active sites from being present, as the poisoning with CO was only partial, the results were consistent with FeN_4C sites providing a majority of the activity.[84] While these sites appear to be active, the mechanism was not thoroughly explored.

One of the major questions regarding the mechanism for O_2 activation is how the molecule activates on an isolated transition metal site. Computational studies on the mechanism for O_2 activation on M-N-C often involve the binding of O_2 first with the isolated transition metal breaking the bond through interaction with liquid or gas molecules of reductant as previously discussed with the ISR.[92, 93, 98] Binding energy calculations for O_2 on Fe-N-C found that O_2 could bind in a bidentate mode to the isolated transition metal and subsequently interact with the hydrogen atoms in the bulk fluid to reduce one oxygen atom at a time.[99] This mechanism is similar to Eley-Rideal (ER) type mechanisms where an adsorbate on the surface can interact with liquid or gas molecules above the surface.[100] Although the ER mechanism with bidentate O_2 on the surface has been proposed, not all transition metals contain the necessary bonds to form bidentate complexes of O_2 in their isolated state in nitrogen-doped carbon.[89] Cobalt ions are only able to form monodentate structures under typical conditions which then is reduced by hydrogen first interacting with the oxygen furthest away from the surface and then either forms a hydroxyl group on the surface or reduces the oxygen bound to Co and forms H_2O_2.[101] Computational modelling of the ORR has proven to be difficult to compare with experimental results due to the complicating effects of solvents (i.e. hydrogen bonding or formation of hydroxyl groups) and potentials (since the carbon support is conductive) and so fundamental studies on mechanistic activation of O_2 is lacking in the literature.

The difficulty of studying the ORR has led groups to explore the activation of O_2 through CO oxidation using DFT. These computational studies have looked at the binding of adsorbates to the surface of the transition metal to understand the mechanism for CO oxidation.[100, 102, 103] For example, Yang and coworkers studied both the Langmuir-Hinshelwood (LH) and ER mechanisms for CO oxidation on CoN_3-pyridinic graphene and found that O_2 preferentially bound to the Co

ion and the ER mechanism had higher barriers the LH mechanism.[100] The LH mechanism involved the binding of both CO and O_2 to the same Co ion, which is unlikely due to bond order conservation, and also resulted in a high transition state barrier (83 kJ mol^{-1}).[104] Although the barrier could be overcome at high temperatures, it is not consistent with the previously reported low temperature activity for Co-N-C.[89] Similar to the reported high barrier for Co-N-C, other studies on mechanisms of CO oxidation for Fe and Mn in N-C have found similar results with barriers above 60 kJ mol^{-1}.[102] These barriers are fairly high and may not be representative of mechanisms that facilitate low temperature CO oxidation. Clearly, complementary DFT and experimental studies are needed to support a mechanism.

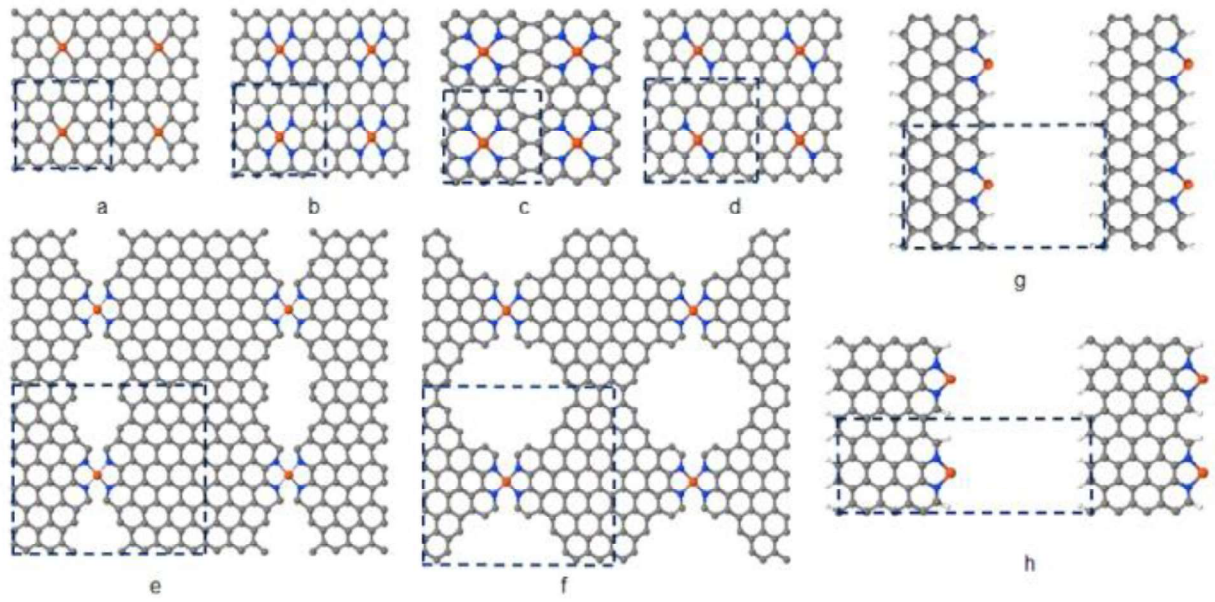

Figure 1.5. Structures a through h are proposed planar, edge, and defect structures of transition metal sites that could be formed during synthesis.
This figure is not all inclusive of possible motifs with other motifs possibly forming but are not commonly studied. Reprinted with permission from *J. Phys. Chem. C* **2016.** *120* (28), 15173-15184. Copyright 2016 American Chemical Society.[84]

1.5 In this Work

Although M-N-C catalysts have reported activity and selectivity comparable to expensive Pt-based electrodes for the ORR and Pt nanoparticles in the catalytic oxidative dehydrogenation of alcohols, the mechanism of O_2 activation and the quantification of active sites remains elusive in many cases. The known heterogeneity of M-N-C catalysts with different potential structural motifs of the isolated transition metal ions complicates the characterization and computational modeling of the system and requires a wide range of techniques to propose a mechanism of O_2 activation. This dissertation attempts to clarify the nature of O_2 activation on isolated M sites. By combining reaction kinetics with characterization and quantum chemical modelling, a mechanism for low temperature O_2 activation is proposed. In Chapter 2 of this dissertation, a Co-N-C catalyst was investigated for CO oxidation since the gas-phase reaction does not have the complicating effects of solvents and applied potentials. Extensive characterization such as STEM, XAS, and steady-state isotopic transient kinetic analysis was combined with DFT calculations to propose a mechanism for O_2 activation. In Chapter 3, the mechanism proposed for O_2 activation during CO oxidation on Co-N-C was investigated for a variety of other metals through screening of descriptors using DFT. Based on the screening results, a Rh-N-C catalyst was selected for synthesis, characterization, and evaluation in low temperature CO oxidation. In Chapter 4, a Co-N-C catalyst was investigated for the oxidative dehydrogenation of 2-propanol in both a down-flow, continuous gas flow, packed bed reactor and in a liquid phase batch reactor with aqueous solvent.

The objectives of this work are as follows:

1. Gain mechanistic insights on the activation of O_2 on isolated transition metal ions in Co-N-C.
2. Understand if the mechanism for O_2 activation for Co-N-C is consistent across other transition metals.
3. Apply the knowledge of the O_2 activation mechanism to an oxidative dehydrogenation reaction with complicating effects of solvent and substrate.

The findings presented in this dissertation will enable a deeper understanding of a facile O_2 activation path. The tools designed in this dissertation can serve as a guide for future exploration of other M-N-C catalysts for various other reactions involving O_2 activation.

1.6 References

1. Montemore, M. M.; van Spronsen, M. A.; Madix, R. J.; Friend, C. M., O_2 Activation by Metal Surfaces: Implications for Bonding and Reactivity on Heterogeneous Catalysts. *Chemical Reviews* **2018,** *118* (5), 2816-2862.

2. Wang, X.; Li, Z.; Qu, Y.; Yuan, T.; Wang, W.; Wu, Y.; Li, Y., Review of Metal Catalysts for Oxygen Reduction Reaction: From Nanoscale Engineering to Atomic Design. *Chem* **2019,** *5* (6), 1486-1511.

3. Roberts, M. W., Chemisorption and Reaction Pathways at Metal Surfaces: The Role of Surface Oxygen. *Chem. Soc. Rev.* **1989,** *18*, 451-475.

4. Stampfl, C.; Soon, A.; Piccinin, S.; Shi, H.; Zhang, H., Bridging the Temperature and Pressure Gaps: Close-Packed Transition Metal Surfaces in an Oxygen Environment. *J. Phys. Condens. Matter* **2008,** *20* (18) 184021.

5. Huang, W.; Sun, G.; Cao, T., Surface Chemistry of Group IB Metals and Related Oxides. *Chem. Soc. Rev.* **2017,** *46* (7), 1977-2000.

6. Hill, C. L.; Weinstock, I. A., On The Trail Of Dioxygen Activation. *Nature* **1997,** *388* (6640), 332-333.

7. Gómez-Marín, A.; Feliu, J.; Edson, T., Reaction Mechanism for Oxygen Reduction on Platinum: Existence of a Fast Initial Chemical Step and a Soluble Species Different from H_2O_2. *ACS Catal.* **2018,** *8* (9), 7931-7943.

8. Kamat, G. A.; Zamora Zeledón, J. A.; Gunasooriya, G. T. K. K.; Dull, S. M.; Perryman, J. T.; Nørskov, J. K.; Stevens, M. B.; Jaramillo, T. F., Acid Anion Electrolyte Effects on Platinum for Oxygen and Hydrogen Electrocatalysis. *Commun. Chem.* **2022,** *5* (1), 1-10.

9. Gray, N.; O'Shea, R.; Wall, D.; Smyth, B.; Lens, P. N. L.; Murphy, J. D., Batteries, Fuel Cells, or Engines? A Probabilistic Economic and Environmental Assessment of Electricity and Electrofuels for Heavy Goods Vehicles. *Adv. Appl. Energy* **2022,** *8*, 100110.

10. Chen, Y.; Ji, S.; Zhao, S.; Chen, W.; Dong, J.; Cheong, W. C.; Shen, R.; Wen, X.; Zheng, L.; Rykov, A. I.; Cai, S.; Tang, H.; Zhuang, Z.; Chen, C.; Peng, Q.; Wang, D.; Li, Y., Enhanced Oxygen Reduction with Single-Atomic-Site Iron Catalysts for a Zinc-Air Battery and Hydrogen-Air Fuel Cell. *Nat. Commun.* **2018,** *9*.

11. He, Y.; Liu, S.; Priest, C.; Shi, Q.; Wu, G., Atomically Dispersed Metal-Nitrogen-Carbon Catalysts for Fuel Cells: Advances in Catalyst Design, Electrode Performance, and Durability Improvement. *Chem. Soc. Rev.* **2020,** *49*, 3484-3524.

12. Wang, X. X.; Swihart, M. T.; Wu, G., Achievements, Challenges and Perspectives on Cathode Catalysts in Proton Exchange Membrane Fuel Cells for Transportation. *Nat. Catal.* **2019,** *2*, 578-589.

13. Liu, J.; Jiao, M.; Lu, L.; Barkholtz, H. M.; Li, Y.; Jiang, L.; Wu, Z.; Liu, D. J.; Zhuang, L.; Ma, C.; Zeng, J.; Zhang, B.; Su, D.; Song, P.; Xing, W.; Xu, W.; Wang, Y.; Jiang, Z.; Sun, G., High Performance Platinum Single Atom Electrocatalyst for Oxygen Reduction Reaction. *Nat. Commun.* **2017,** *8*, 1-9.

14. Huang, L.; Wei, M.; Qi, R.; Dong, C. L.; Dang, D.; Yang, C. C.; Xia, C.; Chen, C.; Zaman, S.; Li, F. M.; You, B.; Xia, B. Y., An Integrated Platinum-Nanocarbon Electrocatalyst for Efficient Oxygen Reduction. *Nat. Commun.* **2022,** *13* (1).

15. Schuurman, Y.; Kuster, B. F. M.; van der Wiele, K.; Marin, G. B., Selective Oxidation of Methyl A-D-Glucoside on Carbon Supported Platinum: III. Catalyst Deactivation. *Appl. Catal. A: General* **1992,** *89* (1), 47-68.

16. Mallat, T.; Baiker, A., Oxidation Of Alcohols With Molecular Oxygen On Platinum Metal Catalysts In Aqueous Solutions. *Catal. Today* **1994,** *19* (2), 247-283.

17. Kaiser, S. K.; Chen, Z.; Faust Akl, D.; Mitchell, S.; Pérez-Ramírez, J., Single-Atom Catalysts across the Periodic Table. *Chem. Rev.* **2020,** *120*, 11703-11809.

18. Yin, H.; Xia, H.; Zhao, S.; Li, K.; Zhang, J.; Mu, S., Atomic Level Dispersed Metal–Nitrogen–Carbon Catalyst toward Oxygen Reduction Reaction: Synthesis Strategies and Chemical Environmental Regulation. *Energy & Environ. Mater.* **2020,** *4* (1), 5-18.

19. Bates, J. S.; Johnson, M. R.; Khamespanah, F.; Root, T. W.; Stahl, S. S., Heterogeneous M-N-C Catalysts for Aerobic Oxidation Reactions: Lessons from Oxygen Reduction Electrocatalysts. *Chem. Rev.* **2022**.

20. Tahoun, M.; Gee, C. T.; McCoy, V. E.; Sander, P. M.; Müller, C. E., Chemistry of Porphyrins in Fossil Plants and Animals. *RSC Advances* **2021,** *11* (13), 7552-7563.

21. Venegas, R.; Muñoz-Becerra, K.; Candia-Onfray, C.; Marco, J. F.; Zagal, J. H.; Recio, F. J., Experimental Reactivity Descriptors of M-N-C Catalysts for the Oxygen Reduction Reaction. *Electrochim. Acta* **2020,** *332*, 135340.

22. Hübner, S.; de Vries, J. G.; Farina, V., Why Does Industry Not Use Immobilized Transition Metal Complexes as Catalysts? *Ad. Synth. & Catal.* **2016,** *358* (1), 3-25.

23. Wang, J.; Wang, J.; Qi, S.; Zhao, M., Stable Multifunctional Single-Atom Catalysts Resulting from the Synergistic Effect of Anchored Transition-Metal Atoms and Host Covalent–Organic Frameworks. *J. Phys. Chem. C*, **2020**; (124), 17675-17683.

24. Fei, H.; Dong, J.; Feng, Y.; Allen, C. S.; Wan, C.; Volosskiy, B.; Li, M.; Zhao, Z.; Wang, Y.; Sun, H.; An, P.; Chen, W.; Guo, Z.; Lee, C.; Chen, D.; Shakir, I.; Liu, M.; Hu, T.; Li, Y.; Kirkland, A. I.; Duan, X.; Huang, Y., General Synthesis and Definitive Structural

Identification of MN_4C_4 Single-Atom Catalysts with Tunable Electrocatalytic Activities. *Nat. Catal.* **2018,** *1*, 63-72.

25. Ali, S.; Liu, T.; Lian, Z.; Li, B.; Su, D. S., The Tunable Effect of Nitrogen and Boron Dopants on a Single Walled Carbon Nanotube Support on the Catalytic Properties of a Single Gold Atom Catalyst: A First Principles Study of CO Oxidation. *J. Mater. Chem. A* **2017,** *5*, 16653-16662.

26. Liu, Q.; Li, Q.; Chen, S., Metal–Nitrogen Coordination Moieties in Carbon for Effective Electrocatalytic Reduction of Oxygen. *Curr. Opin. Electrochem.*, **2020**, (21), 46-54.

27. Frank, B.; Zhang, J.; Blume, R.; Schlogl, R.; Su, D. S., Heteroatoms Increase the Selectivity in Oxidative Dehydrogenation Reactions on Nanocarbons. *Angew Chem Int Ed Engl* **2009,** *48* (37), 6913-7.

28. Chernov, A. N.; Sobolev, V. I.; Koltunov, K. Y., Propane Dehydrogenation to Propylene Over Co@N-Doped Carbon: Structure-Activity-Selectivity Relationships. *Catal. Commun.* **2022,** *170*.

29. Im, K.; Kim, D.; Jang, J. H.; Kim, J.; Yoo, S. J., Hollow-Sphere Co-NC Synthesis by Incorporation of Ultrasonic Spray Pyrolysis and Pseudomorphic Replication and its Enhanced Activity Toward Oxygen Reduction Reaction. *Appl. Catal. B: Environ.* **2020,** *260*, 118192.

30. Liu, W.; Zhang, L.; Liu, X.; Liu, X.; Yang, X.; Miao, S.; Wang, W.; Wang, A.; Zhang, T., Discriminating Catalytically Active FeN_x Species of Atomically Dispersed Fe-N-C Catalyst for Selective Oxidation of the C-H Bond. *J. Am. Chem. Soc.* **2017,** *139*, 10790-10798.

31. Chen, C.; Wang, Z. Q.; Gong, Y. Y.; Wang, J. C.; Yuan, Y.; Cheng, H.; Sang, W.; Chaemchuen, S.; Verpoort, F., Cobalt Embedded in Nitrogen-Doped Porous Carbon as a Robust

Heterogeneous Catalyst for the Atom-Economic Alcohol Dehydrogenation to Carboxylic Acids. *Carbon* **2021,** *174*, 284-294.

32. Liu, L.; Wang, B.; Gao, R.; Zhang, D.; Xu, W.; Chen, L.; Yan, X.; Li, Y., Biomass-Derived Fe-NC Hybrid for Hydrogenation with Formic Acid: Control of Fe-Based Nanoparticle Distribution. *RSC Adv.* **2020,** *10*, 10689-10694.

33. Yang, H.; Nie, R.; Xia, W.; Yu, X.; Jin, D.; Lu, X.; Zhou, D.; Xia, Q., Co Embedded within Biomass-Derived Mesoporous N-Doped Carbon as an Acid-Resistant and Chemoselective Catalyst for Transfer Hydrodeoxygenation of Biomass with Formic Acid. *Green Chem.* **2017,** *19*, 5714-5722.

34. Meng, Y.; Qu, X.; Li, K.; Yang, Y.; Wang, Y.; Wu, Z., Rhodium and Nitrogen Codoped Graphene as a Bifunctional Electrocatalyst for the Oxygen Reduction Reaction and CO_2 Reduction Reaction: Mechanism Insights. *J. Phys. Chem. C* **2019**, *123* (9), 5176-5187.

35. Matsubu, J. C.; Yang, V. N.; Christopher, P., Isolated Metal Active Site Concentration and Stability Control Catalytic CO_2 Reduction Selectivity. *J Am Chem Soc* **2015,** *137* (8), 3076-84.

36. Liu, Q.; Zhang, J., Graphene Supported Co-g-C_3N_4 as a Novel Metal-Macrocyclic Electrocatalyst for the Oxygen Reduction Reaction in Fuel Cells. *Langmuir* **2013,** *29*, 3821-3828.

37. Lu, B.; Smart, T. J.; Qin, D.; Lu, J. E.; Wang, N.; Chen, L.; Peng, Y.; Ping, Y.; Chen, S., Nitrogen and Iron-Codoped Carbon Hollow Nanotubules as High-Performance Catalysts toward Oxygen Reduction Reaction: A Combined Experimental and Theoretical Study. *Chem. Mater.* **2017,** *29*, 5617-5628.

38. Merkys, A.; Vaitkus, A.; Grybauskas, A.; Konovalovas, A.; Quirós, M.; Gražulis, S., Graph Isomorphism-Based Algorithm for Cross-Checking Chemical and Crystallographic Descriptions. *J. Cheminformatics* **2023,** *15* (1), 25.

39. Bates, J. S.; Khamespanah, F.; Cullen, D. A.; Al-omari, A. A.; Hopkins, M. N.; Martinez, J. J.; Root, T. W.; Stahl, S. S., Molecular Catalyst Synthesis Strategies to Prepare Atomically Dispersed Fe-N-C Heterogeneous Catalysts *J. Am. Chem. Soc.* **2022**, *144* (41), 18797-18802.

40. Xie, J.; Kammert, J. D.; Kaylor, N.; Zheng, J. W.; Choi, E.; Pham, H. N.; Sang, X.; Stavitski, E.; Attenkofer, K.; Unocic, R. R.; Datye, A. K.; Davis, R. J., Atomically Dispersed Co and Cu on N-Doped Carbon for Reactions Involving C–H Activation. In *ACS Catal.*, **2018**, (8), 3875-3884.

41. Quan, B.; Xu, G.; Gu, W.; Sheng, J.; Ji, G., Cobalt Nanoparticles Embedded Nitrogen-Doped Porous Graphitized Carbon Composites with Enhanced Microwave Absorption Performance. *J. Colloid Interface Sci.* **2019,** *533*, 297-303.

42. Tang, C.; Surkus, A.-E.; Chen, F.; Pohl, M.-M.; Agostini, G.; Schneider, M.; Junge, H.; Beller, M., A Stable Nanocobalt Catalyst with Highly Dispersed CoN_x Active Sites for the Selective Dehydrogenation of Formic Acid. *Angew. Chem.* **2017,** *129*, 16843-16847.

43. Wen, X.; Yang, X.; Li, M.; Bai, L.; Guan, J., Co/CoOx Nanoparticles Inlaid onto Nitrogen-Doped Carbon-Graphene as a Trifunctional Electrocatalyst. *Electrochim. Acta* **2019,** *296*, 830-841.

44. Chernov, A. N.; Astrakova, T. V.; Sobolev, V. I.; Koltunov, K. Y., Liquid Versus Gas Phase Dehydrogenation of Formic Acid over Co@N-Doped Carbon Materials. The Role of Single Atomic Sites. *Molecular Catalysis* **2021,** *504*.

45. Leonard, N. D.; Wagner, S.; Luo, F.; Steinberg, J.; Ju, W.; Weidler, N.; Wang, H.; Kramm, U. I.; Strasser, P., Deconvolution of Utilization, Site Density, and Turnover Frequency of Fe-Nitrogen-Carbon Oxygen Reduction Reaction Catalysts Prepared with Secondary N-Precursors. *ACS Catal.* **2018,** *8*, 1640-1647.

46. Xu, D.; Zhao, H.; Dong, Z.; Ma, J., Cobalt Nanoparticles Apically Encapsulated by Nitrogen-doped Carbon Nanotubes for Oxidative Dehydrogenation and Transfer Hydrogenation of N-Heterocycles. *ChemCatChem* **2019,** *11*, 5475-5486.

47. Zhu, D.; Huang, Y.; Cao, J. j.; Lee, S. C.; Chen, M.; Shen, Z., Cobalt Nanoparticles Encapsulated in Porous Nitrogen-Doped Carbon: Oxygen Activation and Efficient Catalytic Removal of Formaldehyde at Room Temperature. *Appl. Catal. B: Environ.* **2019,** *258*, 117981.

48. Liang, H. W.; Wei, W.; Wu, Z. S.; Feng, X.; Müllen, K., Mesoporous Metal-Nitrogen-Doped Carbon Electrocatalysts for Highly Efficient Oxygen Reduction Reaction. *J. Am. Chem. Soc.* **2013,** *135*, 16002-16005.

49. Chen, C.; Zhang, J.; Zhang, B.; Yu, C.; Peng, F.; Su, D., Revealing the Enhanced Catalytic Activity of Nitrogen-Doped Carbon Nanotubes for Oxidative Dehydrogenation of Propane. *Chem Commun* **2013,** *49* (74), 8151-3.

50. Chernyak, S. A.; Kustov, A. L.; Stolbov, D. N.; Tedeeva, M. A.; Isaikina, O. Y.; Maslakov, K. I.; Usol'tseva, N. V.; Savilov, S. V., Chromium Catalysts Supported on Carbon Nanotubes and Graphene Nanoflakes for CO_2-Assisted Oxidative Dehydrogenation of Propane. *Appl. Surf. Sci.* **2022,** *578*.

51. Rebarchik, M.; Bhandari, S.; Kropp, T.; Mavrikakis, M., Insights into the Oxygen Evolution Reaction on Graphene-Based Single-Atom Catalysts from First-Principles-Informed Microkinetic Modeling. *ACS Catal.* **2023,** *13* (8), 5225-5235.

52. Wang, M.; Liu, J.; Guo, C.; Gao, X.; Gong, C.; Wang, Y.; Liu, B.; Li, X.; Gurzadyan, G. G.; Sun, L., Metal–Organic Frameworks (ZIF-67) as Efficient Cocatalysts for Photocatalytic Reduction of CO_2: The Role of the Morphology Effect. *J. Mater. Chem. A* **2018,** *6*, 4768-4775.

53. Wang, Y.; Lan, Z.; Huang, X.; Liu, H.; Guo, J., Study on Catalytic Effect and Mechanism of MOF (MOF = ZIF-8, ZIF-67, MOF-74) on Hydrogen Storage Properties of Magnesium. *Int. J. Hydrogen Energy* **2019,** *44*, 28863-28873.

54. Lü, B.; Qi, W.; Luo, M.; Liu, Q.; Guo, L., Fischer-Tropsch Synthesis: ZIF-8@ZIF-67-Derived Cobalt Nanoparticle-Embedded Nanocage Catalysts. *Ind. Eng. Chem. Res.* **2020,** *59*, 12352-12359.

55. He, Y.; Hwang, S.; Cullen, D. A.; Uddin, M. A.; Langhorst, L.; Li, B.; Karakalos, S.; Kropf, A. J.; Wegener, E. C.; Sokolowski, J.; Chen, M.; Myers, D.; Su, D.; More, K. L.; Wang, G.; Litster, S.; Wu, G., Highly Active Atomically Dispersed Con_4 Fuel Cell Cathode Catalysts Derived from Surfactant-Assisted Mofs: Carbon-Shell Confinement Strategy. *Energy & Environ. Sci.* **2019,** *12*, 250-260.

56. Zhang, H.; Hwang, S.; Wang, M.; Feng, Z.; Karakalos, S.; Luo, L.; Qiao, Z.; Xie, X.; Wang, C.; Su, D.; Shao, Y.; Wu, G., Single Atomic Iron Catalysts for Oxygen Reduction in Acidic Media: Particle Size Control and Thermal Activation. *J. Am. Chem. Soc.* **2017,** *139*, 14143-14149.

57. Zhu, C.; Shi, Q.; Xu, B. Z.; Fu, S.; Wan, G.; Yang, C.; Yao, S.; Song, J.; Zhou, H.; Du, D.; Beckman, S. P.; Su, D.; Lin, Y., Hierarchically Porous M-N-C (M = Co and Fe) Single-Atom Electrocatalysts with Robust MN_x Active Moieties Enable Enhanced ORR Performance. *Adv. Energy Mater.* **2018,** *8*, 1801956.

58. Silva, R.; Voiry, D.; Chhowalla, M.; Asefa, T., Efficient Metal-Free Electrocatalysts for Oxygen Reduction: Polyaniline-Derived N- and O - Doped Mesoporous Carbons. *J. Am. Chem. Soc.* **2013**, *135* (21), 8-11.

59. Liu, W.; Zhang, L.; Yan, W.; Liu, X.; Yang, X.; Miao, S.; Wang, W.; Wang, A.; Zhang, T., Single-atom dispersed Co-N-C catalyst: Structure Identification and Performance for Hydrogenative Coupling of Nitroarenes. *Chem. Sci.*, **2016**, (7), 5758-5764.

60. Cheng, Q.; Han, S.; Mao, K.; Chen, C.; Yang, L.; Zou, Z.; Gu, M.; Hu, Z.; Yang, H., Co Nanoparticle Embedded in Atomically-Dispersed Co-N-C Nanofibers for Oxygen Reduction with High Activity and Remarkable Durability. *Nano Energy* **2018,** *52*, 485-493.

61. Xie, C.; Lin, L.; Huang, L.; Wang, Z.; Jiang, Z.; Zhang, Z.; Han, B., Zn-N_x Sites on N-Doped Carbon for aerobic Oxidative Cleavage and Esterification of C(CO)-C Bonds. *Nat. Commun.* **2021,** *12*, 1-12.

62. Halaka, F. G.; Boland, J. J.; Baldeschwieler, J. D., Identification of Neighboring Atoms in Extended X-ray Absorption Fine Structure. *J. Am. Chem. Soc.* **1984,** *106* (19), 5408-5413.

63. Zitolo, A.; Ranjbar-Sahraie, N.; Mineva, T.; Li, J.; Jia, Q.; Stamatin, S.; Harrington, G. F.; Lyth, S. M.; Krtil, P.; Mukerjee, S.; Fonda, E.; Jaouen, F., Identification of Catalytic Sites in Cobalt-Nitrogen-Carbon Materials for the Oxygen Reduction Reaction. *Nat. Commun.* **2017,** *8*, 957.

64. Luo, F.; Roy, A.; Silvioli, L.; Cullen, D. A.; Zitolo, A.; Tahar Sougrati, M.; Can Oguz, I.; Mineva, T.; Teschner, D.; Wagner, S.; Wen, J.; Dionigi, F.; Kramm, U. I.; Rossmeisl, J.; Jaouen, F.; Strasser, P., P-Block Single-Metal-Site Tin/Nitrogen-Doped Carbon Fuel Cell Cathode Catalyst for oxygen Reduction Reaction. *Nat. Mat*. **2020**, (19), 1215-1223.

65. Asset, T.; Atanassov, P., Iron-Nitrogen-Carbon Catalysts for Proton Exchange Membrane Fuel Cells. *Joule*, **2020**, (4), 33-44.

66. Li, J.; Liu, H.; An, Z.; Kong, Y.; Huang, L.; Duan, D.; Long, R.; Yang, P.; Jiang, Y.-Y.; Liu, J.; Zhang, J.; Wan, T.; Fu, J.; Pan, R.; Wang, X.; Vlachos, D. G., Nitrogen-Doped

Carbon for Selective Pseudo-Metal-Free Hydrodeoxygenation of 5-hydroxymethylfurfural to 2,5-dimethylfuran: Importance of Trace Iron Impurity. *J. Catal.* **2023,** *417*, 396-407.

67. Lu, X.; He, J.; Huang, L.; Qin, J.; Ma, Y.; Liu, X.; Zhao, W.; Liu, B.; Zhang, Z., Synergetic Roles of Pyridinic Nitrogen and Carbonyl Sites in Nitrogen-Doped Carbon for the Metal-Free Transfer Hydrogenation Reactions. *Appl. Catal. B: Environ.* **2023,** *324*.

68. Luo, F.; Choi, C. H.; Primbs, M. J. M.; Ju, W.; Li, S.; Leonard, N. D.; Thomas, A.; Jaouen, F.; Strasser, P., Accurate Evaluation of Active-Site Density (SD) and Turnover Frequency (TOF) of PGM-Free Metal–Nitrogen-Doped Carbon (MNC) Electrocatalysts using CO Cryo Adsorption. *ACS Catal.* **2019,** *9*, 4841-4852.

69. Jain, D.; Zhang, Q.; Hightower, J.; Gustin, V.; Asthagiri, A.; Ozkan, U. S., Changes in Active Sites on Nitrogen-Doped Carbon Catalysts Under Oxygen Reduction Reaction: A Combined Post-Reaction Characterization and DFT Study. *ChemCatChem* **2019,** *11*, 5945-5950.

70. Artyushkova, K.; Serov, A.; Rojas-Carbonell, S.; Atanassov, P., Chemistry of Multitudinous Active Sites for Oxygen Reduction Reaction in Transition Metal-Nitrogen-Carbon Electrocatalysts. *J. Phys. Chem. C* **2015,** *119*, 25917-25928.

71. Quílez-Bermejo, J.; Morallón, E.; Cazorla-Amorós, D., Metal-Free Heteroatom-Doped Carbon-Based Catalysts for ORR: A critical Assessment about the Role of Heteroatoms. *Carbon* **2020,** *165*, 434-454.

72. Silva, R.; Voiry, D.; Chhowalla, M.; Asefa, T., Efficient Metal-Free Electrocatalysts for Oxygen Reduction: Polyaniline-Derived N- and O-Doped Mesoporous Carbons. *J. Am. Chem. Soc.* **2013,** *135* (21), 7823-7826.

73. Ferrero, G. A.; Fuertes, A. B.; Sevilla, M.; Titirici, M.-M., Efficient Metal-Free N-Doped Mesoporous Carbon Catalysts for ORR by a template-Free Approach. *Carbon* **2016,** *106*, 179-187.

74. Chen, J.; Wang, X.; Cui, X.; Yang, G.; Zheng, W., Amorphous Carbon Enriched with Pyridinic Nitrogen as an Efficient Metal-Free Electrocatalyst for oxygen Reduction Reaction. *Chem. Commun.* **2014,** *50* (5), 557-559.

75. Lv, Q.; Si, W.; He, J.; Sun, L.; Zhang, C.; Wang, N.; Yang, Z.; Li, X.; Wang, X.; Deng, W.; Long, Y.; Huang, C.; Li, Y., Selectively Nitrogen-Doped Carbon Materials as Superior Metal-Free Catalysts for Oxygen Reduction. *Nat. Commun.* **2018,** *9* (1), 3376.

76. Jiang, H.; Gu, J.; Zheng, X.; Liu, M.; Qiu, X.; Wang, L.; Li, W.; Chen, Z.; Ji, X.; Li, J., Defect-Rich and Ultrathin N Doped Carbon Nanosheets as Advanced Trifunctional Metal-Free Electrocatalysts for the ORR, OER and HER. *Energy & Environ. Sci.* **2019,** *12* (1), 322-333.

77. Anson, C. W.; Ghosh, S.; Hammes-Schiffer, S.; Stahl, S. S., Co(salophen)-Catalyzed Aerobic Oxidation of p-Hydroquinone: Mechanism and Implications for Aerobic Oxidation Catalysis. *J. Am. Chem. Soc.* **2016,** *138* (12), 4186-4193.

78. Hooe, S. L.; Cook, E. N.; Reid, A. G.; Machan, C. W., Non-Covalent Assembly of Proton Donors and p-Benzoquinone Anions for Co-Electrocatalytic Reduction of Dioxygen. *Chem Sci.* **2021,** *12* (28), 9733-9741.

79. Singha, A.; Mondal, A.; Nayek, A.; Dey, S. G.; Dey, A., Oxygen Reduction by Iron Porphyrins with Covalently Attached Pendent Phenol and Quinol. *J. Am. Chem. Soc.* **2020,** *142* (52), 21810-21828.

80. Boaz, N. C.; Bell, S. R.; Groves, J. T., Ferryl Protonation in Oxoiron(IV) Porphyrins and Its Role in Oxygen Transfer. *J. Am. Chem. Soc.* **2015,** *137* (8), 2875-2885.

81. Huang, K.; Fu, H.; Shi, W.; Wang, H.; Cao, Y.; Yang, G.; Peng, F.; Wang, Q.; Liu, Z.; Zhang, B.; Yu, H., Competitive Adsorption on Single-Atom Catalysts: Mechanistic Insights into the Aerobic Oxidation of Alcohols over Co–N–C. *J. Catal.* **2019,** *377*, 283-292.

82. Bates, J. S.; Biswas, S.; Suh, S. E.; Johnson, M. R.; Mondal, B.; Root, T. W.; Stahl, S. S., Chemical and Electrochemical O(2) Reduction on Earth-Abundant M-N-C Catalysts and Implications for Mediated Electrolysis. *J Am Chem Soc* **2022,** *144* (2), 922-927.

83. Howland, W. C.; Gerken, J. B.; Stahl, S. S.; Surendranath, Y., Thermal Hydroquinone Oxidation on Co/N-doped Carbon Proceeds by a Band-Mediated Electrochemical Mechanism. *J. Am. Chem. Soc.* **2022,** *144* (25), 11253-11262.

84. Zhang, Q.; Mamtani, K.; Jain, D.; Ozkan, U.; Asthagiri, A., CO Poisoning Effects on FeNC and CN_x ORR Catalysts: A Combined Experimental–Computational Study. *J. Phys. Chem. C* **2016,** *120*, 15173-15184.

85. Mamtani, K.; Jain, D.; Co, A. C.; Ozkan, U. S., Investigation of Chloride Poisoning Resistance for Nitrogen-Doped Carbon Nanostructures as Oxygen Depolarized Cathode Catalysts in Acidic Media. *Catal. Lett.* **2017,** *147*, 2903-2909.

86. Teng, H.; Suuberg, E. M., Chemisorption of Nitric Oxide on Char. 1. Reversible Nitric Oxide Sorption. *J. Phys. Chem.* **1993,** *97* (2), 478-483.

87. Koper, M. T. M.; Shubina, T. E.; Santen, R. A. V., Periodic Density Functional Study of CO and OH Adsorption on Pt - Ru Alloy Surfaces : Implications for CO Tolerant Fuel Cell Catalysts. *J. Phys. Chem. B* **2002**, *106* (3) 686-692.

88. Luo, F.; Wagner, S.; Onishi, I.; Selve, S.; Li, S.; Ju, W.; Wang, H.; Steinberg, J.; Thomas, A.; Kramm, U. I.; Strasser, P., Surface Site Density and Utilization of Platinum Group

Metal (PGM)-Free Fe-NC and FeNi-NC Electrocatalysts for the Oxygen Reduction Reaction. *Chem. Sci.* **2021,** *12*, 384-396.

89. Kropp, T.; Mavrikakis, M., Transition Metal Atoms Embedded in Graphene: How Nitrogen Doping Increases CO Oxidation Activity. *ACS Catal.* **2019,** *9*, 6864-6868.

90. Wang, J.; You, R.; Zhao, C.; Zhang, W.; Liu, W.; Fu, X. P.; Li, Y.; Zhou, F.; Zheng, X.; Xu, Q.; Yao, T.; Jia, C. J.; Wang, Y. G.; Huang, W.; Wu, Y., N-Coordinated Dual-Metal Single-Site Catalyst for Low-Temperature CO Oxidation. *ACS Catal.* **2020,** *10*, 2754-2761.

91. Esrafili, M. D.; Mousavian, P., A DFT Study on the Possibility of Using a Single Cu Atom Incorporated Nitrogen-Doped Graphene as a Promising and Highly Active Catalyst for Oxidation of CO. *Int. J. Quantum Chem* **2019,** *119*, 25857.

92. Luo, M.; Liang, Z.; Liu, C.; Qi, X.; Chen, M.; Yang, H.; Liang, T., Density Functional Study on the CO oxidation Reaction Mechanism on MnN_2-Doped Graphene. *RSC Adv.* **2020,** *10*, 27856-27863.

93. Zhang, P.; Chen, X. F.; Lian, J. S.; Jiang, Q., Structural Selectivity of CO Oxidation on Fe/N/C Catalysts. *J. Phys. Chem. C* **201**, *116* (33), 17572-17579.

94. Mohammadi-rad, N.; Esrafili, M. D.; Sardroodi, J. J., CuN_3 Doped Graphene as an Active Electrocatalyst for Oxygen Reduction Reaction in Fuel Cells: A DFT Study. *J. Mol. Graphics Modell.* **2020,** *96*, 107537.

95. Wang, Q.; Jin, B.; Hu, M.; Jia, C.; Li, X.; Sharman, E.; Jiang, J., N-Doped Graphene-Supported Diatomic Ni-Fe Catalyst for Synergistic Oxidation of CO. *J. Phys. Chem. C* **2021,** *125*, 5616-5622.

96. Patel, A. M.; Ringe, S.; Siahrostami, S.; Bajdich, M.; Nørskov, J. K.; Kulkarni, A. R., Theoretical Approaches to Describing the Oxygen Reduction Reaction Activity of Single-Atom Catalysts. *J. Phys. Chem. C* **2018,** *122*, 29307-29318.

97. Chen, M.; He, Y.; Spendelow, J. S.; Wu, G., Atomically Dispersed Metal Catalysts for Oxygen Reduction. *ACS Energy Letters* **2019,** *4*, 1619-1633.

98. Lin, R.; Albani, D.; Fako, E.; Kaiser, S. K.; Safonova, O. V.; López, N.; Pérez-Ramírez, J., Design of Single Gold Atoms on Nitrogen-Doped Carbon for Molecular Recognition in Alkyne Semi-Hydrogenation. *Angew. Chem. Int. Ed.* **2019,** *58*, 504-509.

99. Liu, K.; Qiao, Z.; Hwang, S.; Liu, Z.; Zhang, H.; Su, D.; Xu, H.; Wu, G.; Wang, G., Mn- and N- Doped Carbon as Promising Catalysts for Oxygen Reduction Reaction: Theoretical Prediction and Experimental Validation. *Appl. Catal. B: Environ.* **2019,** *243*, 195-203.

100. Wang, S.; Li, J.; Li, Q.; Bai, X.; Wang, J., Metal Single-Atom Coordinated Graphitic Carbon Nitride as an Efficient Catalyst for CO Oxidation. *Nanoscale* **2020,** *12*, 364-371.

101. Zheng, Y.; Jiao, Y.; Zhu, Y.; Cai, Q.; Vasileff, A.; Li, L. H.; Han, Y.; Chen, Y.; Qiao, S. Z., Molecule-Level g-C_3N_4 Coordinated Transition Metals as a New Class of Electrocatalysts for Oxygen Electrode Reactions. *J. Am. Chem. Soc.* **2017,** *139*, 3336-3339.

102. Luo, M.; Liang, Z.; Liu, C.; Qi, X.; Chen, M.; Ur Rehman Sagar, R.; Yang, H.; Liang, T., Single–atom Manganese and Nitrogen Co-Doped Graphene as Low-Cost Catalysts for the Efficient CO Oxidation at Room Temperature. *Appl. Surf. Sci.* **2021,** *536*, 147809.

103. Cui, H.; Liu, Z.; Jia, P., Pd-Doped C_3N Monolayer: A Promising Low-Temperature and High-Activity Single-Atom Catalyst for CO Oxidation. *Appl. Surf. Sci.* **2021,** *537*, 147881.

104. Zhang, X.; Lu, Z.; Yang, Z., Single Non-Noble-Metal Cobalt Atom Stabilized by Pyridinic Vacancy Graphene: An efficient Catalyst for CO Oxidation. *J. Mol. Catal. A: Chem.* **2016,** *417*, 28-35.

Chapter 2 Mechanistic Insights on the Low Temperature Oxidation of CO Catalyzed by Isolated Co Ions in N-Doped Carbon

Reprinted with permission from Whitcomb, C. A.; Sviripa, A.; Schapowal, M. I.; Mamedov, K.; Unocic, R.; Paolucci, C.; Davis, R. J. Mechanistic Insights on the Low Temperature Oxidation of CO Catalyzed by Isolated Co Ions in N-doped Carbon. *ACS Catal.* **2022**, *12* (24), 15529–15540.

Abstract

Isolated cobalt ions on nitrogen-doped carbon (Co-N-C) catalyze CO oxidation at temperatures as low as 196 K, but the active site and mechanism for this reaction remain elusive. In this work, steady-state CO oxidation around 273 K over Co-N-C revealed nearly first order behavior in both CO and O_2 as well as a negative apparent activation energy. Isotopic transient analysis of the reaction confirmed a rapid turnover frequency and low surface coverage of adsorbed intermediates leading to CO_2 (< 10% of the Co). Results from kinetics experiments combined with quantum chemical calculations and molecular dynamics simulations are consistent with a reaction path involving weak adsorption of CO onto Co ions followed by a low barrier for the CO-assisted activation of weakly adsorbed O_2. This proposed mechanism for O_2 activation does not involve a redox cycle with the transition metal ion and may be important in other low temperature catalytic reactions involving O_2.

2.1 Introduction

Transition metal ions (M) isolated in a nitrogen-doped carbon matrix (M-N-C) have demonstrated high activity for both electrocatalytic[1-7] and thermocatalytic[8-12] reactions with molecular oxygen. Some of these M-N-C materials even exhibit activity and selectivity comparable to expensive Pt-based electrodes in the electrochemical oxygen reduction reaction (ORR) and Pt nanoparticles in the catalytic oxidative dehydrogenation of alcohols.[1, 2, 8-10, 13] Although M-N-C catalysts facilitate both thermal and electrochemical reactions involving O_2 activation, both the coordination environment around the isolated metal center and the mechanism for O_2 activation remain controversial.[8-10]

To investigate O_2 activation over M-N-C catalysts in the absence of the complicating effects of solvents and applied potentials, gas phase oxidation of CO by O_2 has been used. Catalytic CO oxidation was recently investigated on Fe-N-C, Co-N-C, and materials containing both Co and Fe (Co, Fe-N-C), with the Co-containing samples promoting oxidation catalysis even at dry-ice acetone temperatures.[14] The reported high conversion achieved at low temperature over Co, Fe-N-C specifically was attributed to the relatively weak but preferential binding of CO to Co simultaneous with O_2 binding on nearby Fe.[14] Strasser and co-workers confirmed with cryo-CO chemisorption measurements that CO indeed adsorbs on Fe and FeNi M-N-C type catalysts strongly while other metals such as Ni catalysts exhibit low heats of adsorption.[15, 16] In the well-studied catalytic oxidation of CO on transition metal particles such as Pt and Pd, chemisorption of reactants to the metal prior to surface reaction is required to form product CO_2 in a Langmuir-Hinshelwood type mechanism (LH).[17, 18] The strong binding of CO to platinum group metals restricts the use of nanoparticle-based catalysts to higher temperatures for CO oxidation as

competitive adsorption of CO at lower temperature actually inhibits catalytic turnover.[18] Other potential reaction paths for CO oxidation are of the Eley-Rideal (ER) type (involving reaction of a gas phase species with an adsorbed species) and the Mars-van Krevelen-type (MvK) (involving transfer of lattice oxygen followed by re-oxidation of the lattice).[19, 20] Very recently, results of studies with isolated Ir atoms supported on Mg/Al_2O_4 are consistent with an interesting mechanism involving a spectator CO molecule binding to the Ir site, while the CO oxidation reaction proceeds through an ER type mechanism involving surface oxygen.[21] Low temperature CO oxidation has also been reported to occur on Au nanoparticles supported on reducible oxides where CO binds weakly to Au and the reducible oxide support is involved in the activation of O_2, which can be considered to occur through an MvK-type mechanism.[22-24]

Some unique formulations of Co oxides also demonstrate catalytic activity in CO oxidation at sub-ambient temperature and the reaction is proposed to occur through an MvK mechanism.[25-27] The catalytic cycle is hypothesized to proceed through a Co^{3+} / Co^{2+} redox cycle involving labile O^{2-} sites from the support.[27-29] As the Co-N-C catalysts with isolated Co^{2+} ions lack labile O^{2-} sites, as well as sites containing multiple Co ions required to activate O_2 through a standard redox process, it is unclear how CO oxidation might occur through a redox cycle on these materials. Given the unusual behavior of a nominally single site M-N-C catalyst that can activate O_2 at temperatures as low as 196 K, there is a need for a molecularly detailed understanding of the reaction mechanism.

Here, we explore a potential mechanism of low temperature CO oxidation on Co-N-C catalysts using steady-state and transient kinetic experiments, quantum chemical calculations, and molecular dynamics simulations. Our experimental and computational results are consistent with a mechanism for O_2 activation involving interactions with weakly adsorbed CO on the Co-N-C

catalyst, emphasizing the important role of co-adsorbates in surface-catalyzed reactions. This proposed mechanism differs from previously described strong binding systems that utilize support oxygen species and redox cycles to catalyze reactions involving O_2 activation.

2.2 Methods

2.2.1 Synthesis of Co Catalysts

The Co-N-C catalyst was synthesized via a modified method of high temperature pyrolysis similar to previously reported methods.[8, 9, 30] Cobalt nitrate hexahydrate (0.492 g) (Sigma-Aldrich Corporation) was dissolved in 10 cm^3 of distilled, de-ionized (DDI) H_2O and added to a solution of 1,10 phenanthroline (0.611 g) (Sigma-Aldrich Corporation) in 15 cm^3 ethanol (Sigma-Aldrich Corporation) to make a 1:2 molar ratio of Co: phenanthroline before stirring for 20 min at 353 K. This mixture was subsequently added dropwise to a 0.1 M NaOH slurry with Carbon Black Pearls 2000 (Cabot Corporation) at 353 K and stirred for 2 h. The slurry was then washed with 3000 cm^3 of DDI H_2O and vacuum filtered before drying overnight at 343 K. The sample with deposited Co phenanthroline complex was then impregnated with 80 wt % dicyandiamide relative to the complex. The solution was vigorously stirred at 343 K and then dried overnight. The impregnated sample was subsequently ramped in ultra-high purity (UHP) N_2 (100 cm^3 min^{-1}) (99.999 %, Praxair) at 10 K min^{-1} and then held at 973 K for a high temperature thermal treatment. To ensure removal of nanoparticles, the Co-N-C catalyst (100 mg) was then acid washed with a vigorously stirred 1 M HCl solution (100 cm^3) at room-temperature for 12 h. The acid washed catalyst was then thoroughly washed and filtered before drying overnight at 343 K. To reduce the possibility of Cl^- ions being deposited on the surface, a second thermal treatment was conducted. The catalyst

was ramped at 10 K min^{-1} to 673 K and held for 2 h in flowing UHP H_2 (100 cm^3 min^{-1}) (5 % H_2/Ar). This catalyst was subsequentially used as synthesized. The nitrogen-carbon (N-C) catalyst without metal was synthesized via impregnation of an aqueous solution of 0.4 g dicyandiamide (Sigma-Aldrich) into 0.5 g of Carbon Black Pearls 2000 using the same thermal treatment method described above for the metal loaded catalyst. The 5 wt % CoO_x/SiO_2 catalyst was synthesized by incipient wetness impregnation wherein cobalt nitrate hexahydrate (0.5 g) was dissolved in 2.5 cm^3 of DDI H_2O and added dropwise to silica gel (2 g) (Davisil 636 Silica Gel).[31, 32] The catalyst was then dried overnight at room temperature before drying for two hours in an oven at 393 K. The catalyst was then ramped at 10 K min^{-1} to 673 K and thermally treated for 2 h in flowing air (Medical Grade, Praxair). The 10 wt % Co/CB catalyst was synthesized by incipient wetness impregnation of cobalt acetate (0.04 g, Aldrich) dissolved in 1 cm^3 DDI H_2O onto Carbon Black Pearls 2000 (0.2 g). The mixture was then dried at 393 K overnight. The catalyst was then thermally treated at 973 K for two hours after ramping at 10 K min^{-1} in UHP He (99.999 %, Praxair). The Co_3O_4 (Co (II, III) Oxide, Alfa Aesar) was used from the bottle and thermally treated for 5 hours at 673 K in 100 cm^3 min^{-1} flowing air after ramping at 10 K min^{-1}.

2.2.2 Characterization of Catalysts

High-angle annular dark-field STEM imaging was performed using an aberration-corrected STEM JEOL NeoARM, operating at 80 kV and using a convergence semi-angle of 27 mrad.

All inductively coupled plasma optical emission spectroscopy (ICP) analyses were completed at Galbraith Laboratories Inc. (2323 Sycamore Drive, Knoxville, TN 37921). The metal

loadings of the Co catalysts were determined using ICP-OES on a PerkinElmer Optima 5300V, 8300DV, or Avio 500 ICP-OES.

X-ray photoelectron spectroscopy (XPS) measurements were performed using a PHI VersaProbe III spectrometer equipped with a Monochromatic Al k-alpha X-rays (1486.6 eV) and a hemispherical analyzer. A 1400 μm sample spot size was utilized with a pass energy of 55 eV and an X-ray beam size of 100 μm for high resolution region scans. A dual neutralization system consisting of an internal electron flood gun (1 eV) and a low energy Ar ion gun was utilized during data collection. Binding energies for all elements were referenced to the C 1s peak at 284.8 eV.

X-ray absorption spectroscopy (XAS) at the Co K edge was performed on beamline 8-ID at the National Synchrotron Light Source II at Brookhaven National Laboratory with a ring energy of 3.0 GeV and a beam current of 400 mA. A Co metal foil (Goodfellow Corporation) was used as a reference for the Co (7709 eV) K edge. Samples were prepared by dilution of catalyst in boron nitride and adjusted to provide an adsorption edge jump of close to unity. The spectra were collected by utilizing a temperature-controlled transmission cell previously described.[33] A flow of H_2 or CO at 10 cm^3 min^{-1} was flowed over the samples that were enclosed in the Kapton window chambers. The XAS data were processed using the Demeter software package.[34] The Co-N amplitude reduction factor was obtained from Xie et al. using Co phthalocyanine as a reference material at the same beamline.[9]

2.2.3 Oxidation of CO

The oxidation of CO was carried out in a stainless-steel, down flow, continuous packed bed reactor (Fig. A1). The catalyst was diluted with 0.25 g of SiC (Universal Photonoics, Inc., 150 mesh) for each reaction. Reaction conditions were: 160 cm^3 min^{-1} total gas flow with 1 % CO

(Praxair 4 % CO/He), 1 or 13 % O_2 (Praxair 20 % O_2/He), 1 % Ar (Praxair UHP, 99.999 %), and balance He (Praxair UHP, 99.999 %) at 3 atm. The He, Ar, and H_2 lines were passed through OMI-2 indicator filters while the CO and O_2 gases were purified through silica traps in a dry ice-acetone bath. Prior to any reaction run, the catalyst was thermally pretreated in situ by ramping at 10 K min^{-1} to 673 K and held for 2 h in He before cooling to the reaction temperature. The reactor effluent was analyzed using a Balzers Quadrupole Mass Spectrometer. Signals associated with masses (m/e) 28, 29, 40, 44, and 45 amu were recorded at a voltage of 1200 V and dwell times of 50 ms for all masses except 44 and 45, which were measured at 100 ms.

2.2.4 Steady-State Isotopic Transient Kinetic Analysis

Transient kinetic experiments were conducted using the same reactor setup and gas flows as for the oxidation of CO (Fig. A1). The Co-N-C catalyst (0.03 g) was loaded with SiC diluent (0.25 g) into the packed bed reactor. A pretreatment in flowing He at 673 K was done before cooling to 273 K for the steady-state isotopic transient kinetic analysis (SSITKA) experiments. A full explanation of the methodology for SSITKA can be found in the review by Shannon and Goodwin.[35] Briefly, integration of the area between the normalized transient responses, F_i, of product $^{12}CO_2$ or $^{13}CO_2$ and Ar (to account for the gas phase holdup of the system) following a switch at equal temperature and pressure allows for the average residence time of surface intermediates leading to product, τ, to be calculated according to:

$$\tau = \int_0^\infty \left[F_{12_{CO_2}} - F_{Ar}\right] dt \quad (1)$$

The τ determined from the transient response of the product can also include the influence of re-adsorption on the catalyst prior to exiting the reactor, causing the calculated τ for CO_2 production

to be a convolution of the intrinsic kinetics of the CO oxidation reaction and a time delay caused by re-adsorption on the catalyst. Evaluation of τ at various flow rates can be helpful to determine if product re-adsorption in the catalyst bed is affecting the measurement.[35, 36] According to Fig. A2 a and b, the conversion of the CO oxidation reaction was strictly proportional to the inverse of the flow rate, confirming the rate of reaction was constant over the range of conversions and flow rates used.

2.2.5 Density Functional Theory Calculations

We performed spin-polarized periodic supercell density functional theory (DFT) calculations with a plane wave basis set and an energy cutoff of 500 eV using the Vienna ab initio simulation package (VASP)[37] version 5.4.4. All structures were converged to a criterion of 10^{-6} eV and 0.01 eV/Å for self-consistent-field (SCF) energies and atomic forces, respectively. We used a 8.5 Å x 9.8 Å graphene supercell with 14 Å vacuum in the z-direction with two vacancies for a total of 31 C atoms (when the number of nitrogen atoms is zero) as well as zero to four pyridinic N atoms and a Co atom (corresponding to a density of 1.2 Co nm^2). All structure files are provided as supporting files to this dissertation. Monkhorst-Pack k-points were used with a 4 x 4 x 1 mesh. We considered multiple binding modes (e.g. monodentate and bidentate O_2 on Co) and spin states for each structure; all structure files are included as a supporting information attachment. To test the sensitivity of our results to the cell size and Co density in the supercell we computed CO and O_2 binding energies in larger supercells that contained 1-2 Co atoms (Table A1) and found they were insensitive to the Co density in the supercell between 0.3 – 1.2 Co nm^2. We report only energies and not free energies because the reaction intermediates are weakly adsorbed and not amenable to standard free energy approximations. To reduce computational cost, we

neglected vibrational zero-point energy corrections, which are expected to have a negligible contribution to our reaction energies for this system.

Recent reports on similar structures[38,39] indicate that reaction energies for these materials are sensitive to functional choice. Therefore, the gas phase CO oxidation reaction energy (Appendix Table A2), CO and O_2 binding energies, and reaction mechanism calculations were performed with a variety of commonly used functionals (Appendix Table A3). The CO and O_2 binding energies on CoN_4 vary from -92 to -50 kJ mol^{-1}, and -82 to -57 kJ mol^{-1}, respectively, depending on the choice of DFT functional (Appendix Table A3). However, the trend of weaker binding energies with increasing N substitution is preserved across all functionals. We chose to report the values computed with the vdW-DF functional[40] in the main text because this functional accounts for nonlocal electron correlation dispersion interactions (important for weak adsorption), reproduces the experimental enthalpy of reaction for gas phase CO oxidation as reported in Appendix Table A2, and the experimental CO binding energy determined by microcalorimetry[14] (-58.8 kJ mol^{-1}) on Co-N-C materials with isolated Co sites.[14] For comparison we also report the corresponding PBE-D3[41] and vdW-DF2[42] reaction coordinate diagrams in Appendix Fig. A3.

Transition states were determined using climbing image nudged elastic band (CI-NEB) calculations per the method of Henkelman et al.,[43, 44] and are reported in Appendix Fig. A4. We calculated TS1 with various spin states and found that although the barrier is sensitive to the choice of spin, and generally decreases with lower spin, the reactant energy varies only weakly with spin state. Therefore, we report the low spin reaction coordinate (magnetic moment = 0) for the reaction corresponding to TS1.

2.2.6 Ab Initio Molecular Dynamic Simulations

For the AIMD simulations we used the PBE-D3 functional for two reasons: 1) it is much less computationally expensive than vdW-DF, and 2) CO and O_2 binding energies are more exothermic with PBE-D3 than vdW-DF (Table A3), which enabled us to run the simulations at temperatures high enough (398 K) to frequently overcome low energy barriers without desorption of the reactants. This temperature is still low enough that direct dissociation of O_2 over Co during the AIMD simulation would be prohibitive based on the 66 kJ mol^{-1} barrier computed with PBE.[45] Appendix Fig. A5 reports the free energies during the AIMD simulations and structural snapshots. Movies and structures for the full trajectories are provided as a supporting information attachment. All AIMD simulations were run in VASP version 5.4.4 at 398 K using a Nose-Hoover thermostat with a time step of 0.5 fs.

2.3 Results

2.3.1 Catalyst Synthesis and Characterization

The 1.89 wt % Co-N-C catalyst was synthesized using a modified high temperature pyrolysis method in N_2.[9] To disperse Co ions in Co-N-C and remove residual nanoparticles, treatment in mild acid solution followed by high temperature treatment in H_2 was conducted. To confirm the presence of isolated Co ions on Co-N-C, we examined the sample by atomic resolution high-angle annular dark-field scanning transmission electron microscopy (HAADF-STEM) which is shown in Fig. 2.1. We did not observe any Co nanoparticles, indicating that washing a freshly pyrolyzed sample in mild acid solution was effective at removing Co nanoparticles without removing Co ions present in the N-C support.

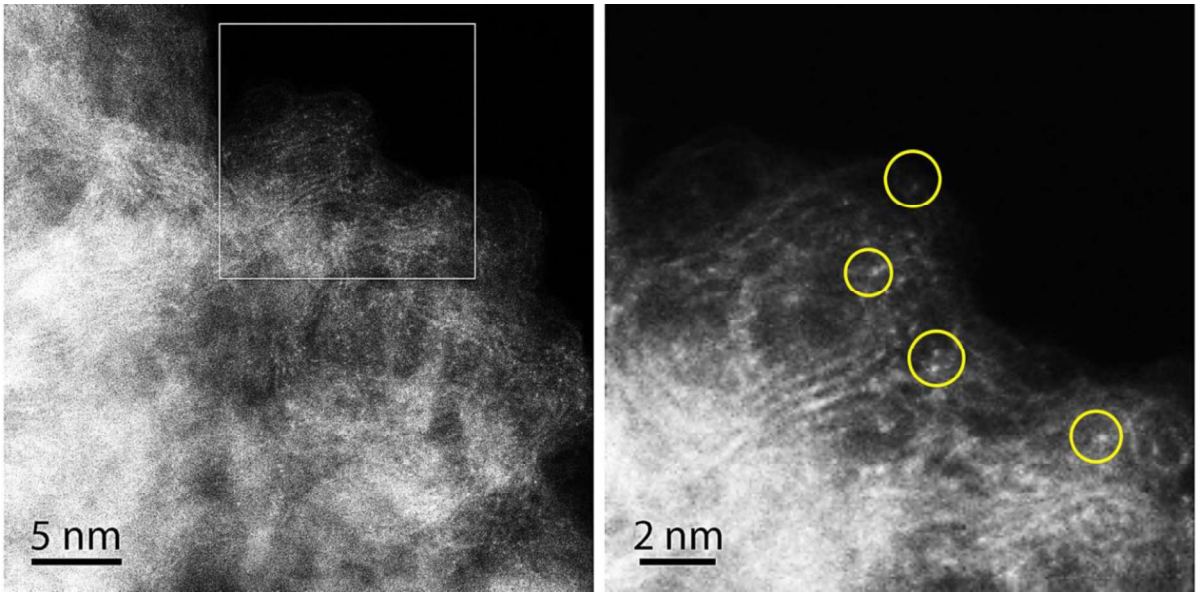

Figure 2.1. Atomic resolution HAADF-STEM images of Co-N-C show single atom distribution of Co atoms.
The right panel is an inset of the boxed area in the left panel. The Co atoms in the expanded area are circled in yellow.

X-ray photoelectron spectroscopy (XPS) was used to determine the chemical state of the Co and N in the catalyst. Spectra associated with the Co $2p_{3/2}$ and the N 1s regions are shown in Figs. A6 and A7, respectively. The presence of a major peak at a binding energy (BE) of 780.9 eV in the Co $2p_{3/2}$ spectrum accompanied by a satellite peak at 785.9 eV at one-third the intensity is consistent with Co^{2+}.[9, 46, 47] Multiple forms of N are usually observed by XPS of similar materials, including pyridinic (BE=398 eV), pyrrolic (BE=400 eV), and graphitic (BE=401 eV), with pyridinic being commonly associated with formation of the Co active site (Fig. A7).[48, 49] Appendix Table A4 shows that the molar ratio of pyridinic N relative to Co^{2+} is ~10:1, which suggests there is sufficient pyridinic N content to form commonly proposed CoN_x sites (x=4,5,6).[6, 50] The surface Co loading measured from XPS is 1.2 $\pm$ 0.1 wt % which differs slightly from the inductively coupled plasma optical emission spectroscopy (ICP-OES) analysis of the bulk catalyst (1.89 wt %

Co) but is consistent with a majority of the Co having a homogeneous distribution throughout the sample. The N:Co ratio and Co loading on the sample were similar to those reported for a sample previously prepared using the same synthesis method and results from characterization of that sample by X-ray absorption spectroscopy (summarized in Fig. 2.2 and Table 2.1) suggest the majority of the Co is bound to ~4 N atoms, which is consistent with earlier work.[9]

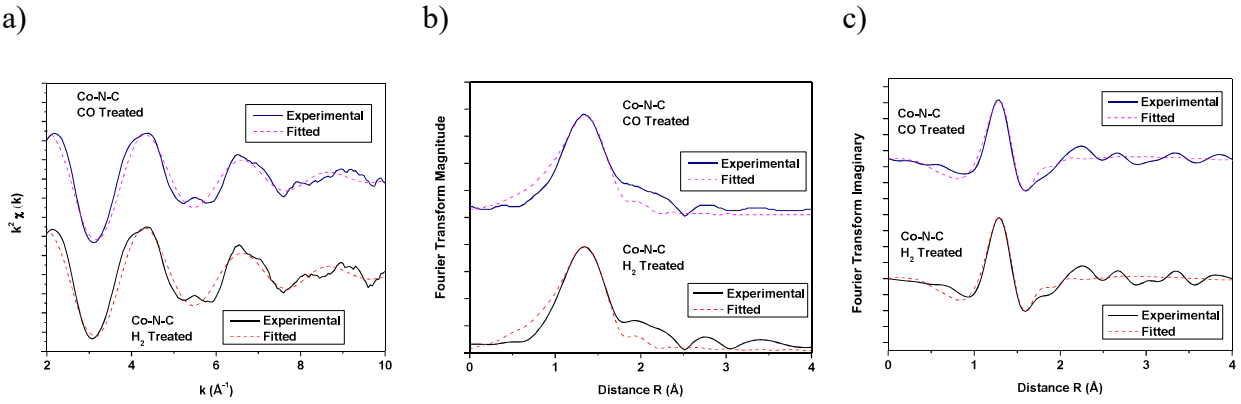

Figure 2.2. Fitting of the extended X-ray absorption fine structure (EXAFS) region of the Co K edge for the Co-N-C catalyst.
a) Contributions of the Co-N path fitted in k space for Co-N-C during H_2 or CO flows (10 cm^3 min^{-1}). The catalyst was initially ramped in H_2 to 738 K and held for 2 hours before cooling to 303 K. b) Fourier transforms (Experimental and Fitted) of k^2-weighted Co EXAFS for Co-N-C under flowing H_2 or CO. c) Imaginary components (Experimental and Fitted) of the Fourier transform of k^2-weighted Co-N-C EXAFS obtained under flowing H_2 or CO.

Table 2.1. Results of the analysis of Co EXAFS on Co-N-C during H_2 or CO flow[a]

Conditions	Shell	CN	r (Å)	$\Delta\sigma^2$ (Å^2)	ΔE_o (eV)
H_2	Co-N	4.9 ± 1.6	1.92 ± 0.03	0.01 ± 0.005	-3.2 ± 3.7
CO	Co-N	4.8 ± 1.8	1.93 ± 0.04	0.01 ± 0.01	-1.9 ± 4.3

[a] Fitting parameters: Fourier transform range, Δk, 1.5-10 Å^{-1}; fitting range ΔR, 1-2 Å; k^2 weighting, S_o^2 (Co-N) = 0.775 (obtained from Xie et al. using Co phthalocyanine as a reference material).[9] The Co-N-C catalyst was initially ramped in H_2 at 10 K min^{-1} to 738 K and held for two hours before cooling to 303 K in H_2.

2.3.2 Oxidation of CO over Co Catalysts

To determine the effect of support composition on catalytic performance, the oxidation of CO was evaluated over a variety of supported Co catalysts over a range of temperatures (273 – 453 K) at a total pressure of 3 atm. The total pressure of 3 atm was achieved by adding He gas to substantially lower partial pressures of CO and O_2 so that pressure transients often observed during isotopic transient experiments could be eliminated. All reaction kinetics reported here were evaluated in the steady-state regime. Oxidation of CO was not observed over an N-C sample that was prepared in the absence of the Co precursor, which illustrates the importance of the Co component in the reaction. In addition to Co-N-C, various other Co-containing catalysts were investigated, including highly dispersed 4.78 wt % Co/SiO_2, nitrogen-free 2.29 wt % Co supported on carbon black (Co/CB), and Co oxide (Co_3O_4). Figure 2.3 illustrates the excellent catalytic performance of Co-N-C relative to the other Co catalysts at temperatures < 340 K, with the conversion of CO actually increasing with decreasing temperature for Co-N-C.

Multiple groups have reported on low temperature CO oxidation catalyzed by Co oxide structures.[28, 29, 51, 52] For example, Schüth and co-workers previously showed that CO oxidation can occur on uniquely shaped small Co oxide structures at temperatures as low as 196 K, while Haruta and co-workers found that Co spinel structures were also active at temperatures ranging

from 198 to 323 K.[27, 28] The interesting "U" shape of the CO conversion with temperature (Fig. 2.3) observed for our Co-N-C catalyst is reminiscent of results for some Co oxide samples reported earlier.[27, 51] In previous work on Co oxide, a similar "U" shaped conversion plot was seen at temperatures between 273 and 373 K where activity dropped from 100 % conversion at 273 K to 70 % at 363 K before returning to 100 % at temperatures higher than 373 K.[27] One possible explanation for the "U" shape conversion plot is the presence of trace water impurities that deactivate the catalyst at ambient temperatures while operation at low temperatures serves as a cold trap for water removal and operation at high temperatures minimizes the influence of water as an inhibitor.[27, 51] Indeed, upon purification of the gases by passing through cold traps, the "U" shape was avoided and 100 % conversion was observed at all temperatures investigated.[27] This inhibition contrasts with reports for some Au catalysts[53-55] and FeO-Pt interfaces,[56] where surface hydroxyl groups are known to promote the low temperature oxidation of CO. To explore the potential influence of water, we evaluated CO oxidation over Co-N-C in the presence and absence of co-fed water at 273 and 303 K. Appendix Figure A8 shows cofed water (0.05 vol %) inhibited the conversion of CO, but conversion recovered when the water addition was stopped. The inhibition of the rate by addition of 0.05 vol % H_2O suggests that water is not required for low temperature CO oxidation on Co-N-C.

All the gases in our study were purified (see Methods Section 2.2) to minimize any impacts of water on the steady-state rate. Contrary to the report by Schüth and co-workers,[27] the "U" shape of conversion as a function of temperature remained in our study (Figs. 2.3 and 2.4). Moreover, Schüth and co-workers reported that high temperature pretreatment of a Co oxide catalyst in H_2 eliminated low temperature activity (<273 K) for CO oxidation.[27] They hypothesized that reduction of Co^{3+} surface species to Co^{2+} accompanied by a loss of labile O^{2-} species was

responsible for the loss of low temperature activity.[27] To explore the potential influence of reducible Co species on the rate of CO oxidation, we evaluated the effect of H_2 pretreatment on the steady-state reaction. As summarized in Fig. 2.4, an in situ pretreatment of the Co-N-C catalyst at 673 K in H_2 did not significantly influence the rate or unusual "U" shape of the conversion. Evidently, easily reducible Co species, if present, are not responsible for the CO oxidation reaction at sub-ambient temperatures, which is consistent with our XPS results that indicate a majority of the Co in Co-N-C is Co^{2+}. A comparison of the X-ray absorption near edge structure (XANES) of Co-N-C after high temperature treatment in H_2 and subsequent cooling to 303 K with the XANES after CO exposure (Fig. 2.5) shows no change in the edge position, confirming that exposure of the catalyst to H_2 or CO does not alter the oxidation state of the Co. Analysis of the extended X-ray absorption fine structure (Fig. 2.2 and Table 2.1) indicates exposure of Co-N-C to CO followed by a purge in inert gas did not result in a measurable change in the average coordination environment around Co in the sample. Evidently, the number of exposed Co ions in Co-N-C that strongly bind CO at 303 K was very low.

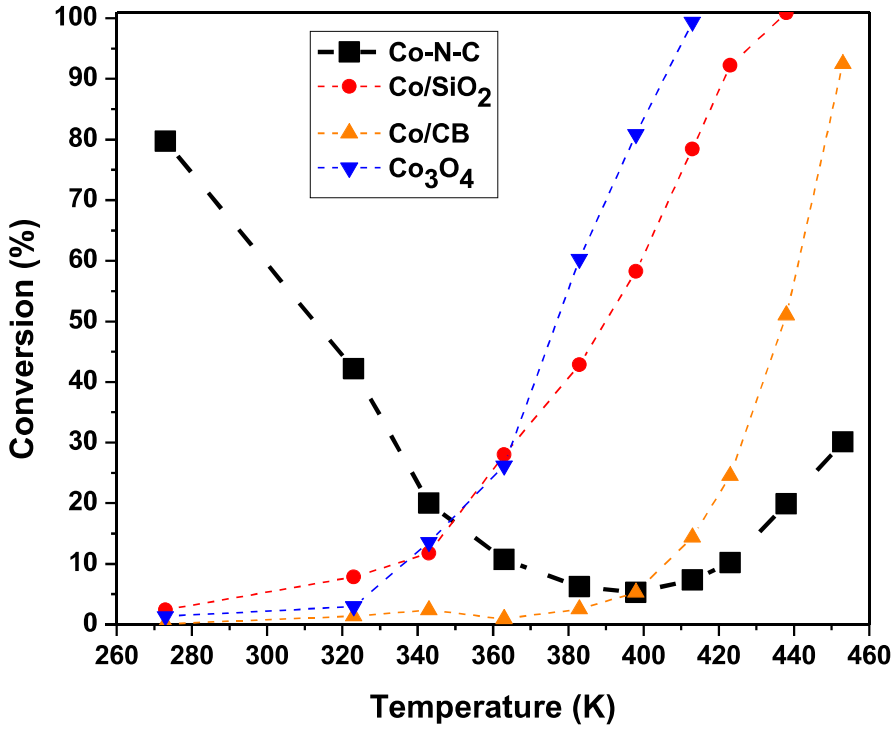

Figure 2.3. Temperature dependence of steady-state CO conversion over Co catalysts. All reactions were run with 100 mg of catalyst diluted in SiC with 160 cm^3 total flow, 1 % CO, 13 % O_2, 1 % Ar, and balance He at 3 atm. The O_2 and CO lines were purified with silica traps in a dry-ice acetone bath while the He and Ar lines were purified with an OMI Filter.

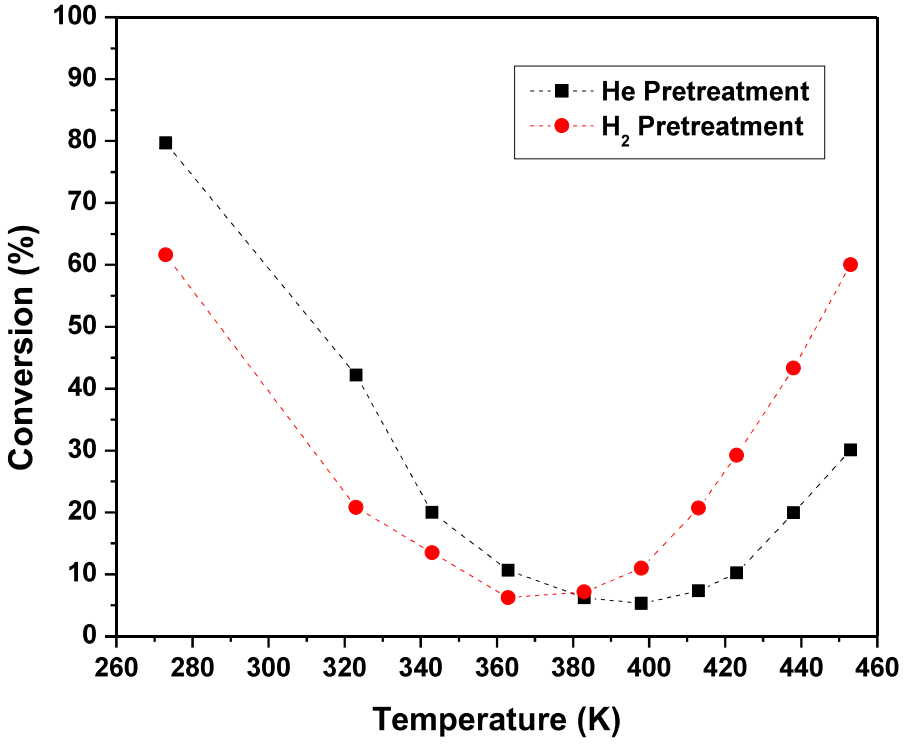

Figure 2.4. Temperature dependence of steady-state CO conversion over Co-N-C following inert or reductive pretreatment.

The reactions were performed sequentially, (He followed by H_2 pretreatment at 673 K) without removing the catalyst. The reaction was run with 100 mg of Co-N-C diluted in SiC and with 160 cm^3 total flow, 1 % CO, 13 % O_2, 1 % Ar, and balance He at 3 atm. The O_2 and CO lines were purified with silica traps in a dry-ice acetone bath while the He and Ar lines were purified with an OMI Filter.

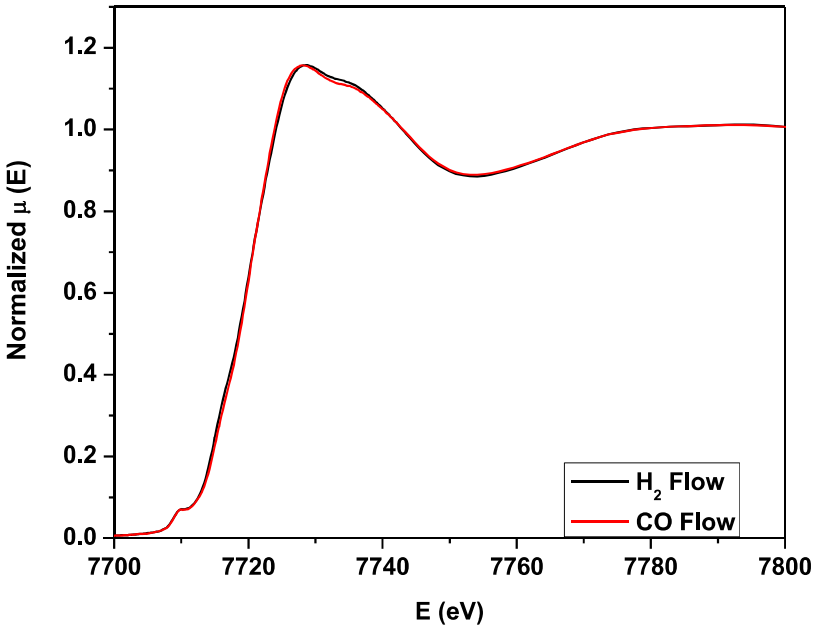

Figure 2.5. Normalized X-ray absorption near edge structure for Co-N-C.
Comparison of the normalized XANES for Co-N-C under H_2 and CO in situ flows (10 cm^3 min^{-1}). The catalyst was initially ramped in H_2 to 738 K and held for 2 hours before cooling to 303 K. The multiple scans were averaged for each XANES.

The observed orders of reaction during CO oxidation catalyzed by Co-N-C shown in Table 2.2 were strikingly different compared to those measured over other Co containing catalysts. The nearly first order dependence of the rate on CO observed over Co-N-C contrasts the inhibition by CO typically observed for platinum group metal catalysts that bind CO strongly.[57] Indeed, the positive reaction order in CO indicates binding to the active site is weak, which is consistent with the EXAFS results discussed above. The reaction orders for CO oxidation on the Co-N-C catalyst were not significantly affected by operation in the low (303 K) or high temperature regime (443 K) (Appendix Fig. A9). An attempt at investigating the kinetics at 196 K proved difficult as the activity was outside of the differential regime even when lowering the partial pressures of reactants and amount of catalyst (Appendix Fig. A10). Apart from Co-N-C, the CO reaction order measured over all the Co-containing catalysts in Table 2.2 was close to zero. Since Co oxide catalysts are

believed to catalyze CO oxidation via an MvK type mechanism, the rate of CO reduction of the surface is rapid relative to re-oxidation.[27, 28, 58] Interestingly, the orders of reaction in Table 2.2 for CO oxidation on Co-N-C are similar to those reported for isolated Ir atoms on $MgAl_2O_4$, for which an ER mechanism of CO oxidation has been postulated.[21]

The observed increase in the rate with lowering the temperature of CO oxidation over Co-N-C results in a negative apparent activation energy of -30 kJ mol^{-1} in the low temperature region of Figs. 2.3 and 2.4. While high temperature CO oxidation on Co containing catalysts has been previously investigated,[45] the unique low temperature activity regime is relatively unexplored. To further explore the origins of the low temperature activity of CO oxidation over Co-N-C, we performed isotopic transient analysis of the steady-state reaction.

Table 2.2. Summary of kinetic orders for CO and O2 on various Co containing catalysts along with the apparent activation energy for CO oxidation

Catalyst	$E_{apparent}$[a] (kJ mol^{-1})	Orders of Reaction[b]	
		CO	O_2
Co-N-C			
Low T regime	-30	0.8	0.7
High T regime	50	0.4	0.7
Co/SiO_2	36	0.0	0.2
Co/CB	50	0.0	0.6
Co_3O_4	38	0.1	0.4
Co_3O_4[c]	46.6	0	0.41

a) Apparent activation energy determined from Arrhenius-type plots shown in Figs. A11 and A12.
b) Kinetic orders were evaluated under steady-state differential conversion (<20 %) and were determined by varying the partial pressure (from 1.5 to 4.5 kPa) of CO or O_2 while maintaining the other.
c) Reference values from Perti and Kabel[57]

2.3.3 Steady-state Isotopic Transient Kinetic Analysis

As the number of active sites on the Co-N-C catalyst is unknown, a reaction rate normalized by the total Co loading may underestimate the turnover frequency (TOF) of the reaction. To better evaluate the TOF, we performed SSITKA of the CO oxidation reaction, which is a kinetic method that does not require a priori knowledge of the active site density to normalize the observed rate. After achieving steady state during CO oxidation at 273 K, the reactant stream was abruptly switched to one that contains ^{13}CO instead of ^{12}CO using the scheme shown in Appendix Fig. A1. More experimental details can be found in the Methods Section 2.2 and an example switch between ^{12}CO/Ar and ^{13}CO/He during steady-state CO oxidation is shown in Fig. 2.6 a. In brief, the integration of the areas under the product $^{12}CO_2$ or $^{13}CO_2$ subtracted from the tracer Ar signal gives the average residence time of surface intermediates leading to product (τ). The strong influence of flow rate on τ given in Fig. 2.6 b for the case without a co-feed of CO_2 indicates the rate is affected by conversion or there is a strong influence of product re-adsorption on the measured τ. As illustrated in Appendix Fig. A2, varying the reactant flow rate changes the conversion of CO between 6 and 13 % (with no co-fed CO_2), resulting in a reaction rate that is independent of conversion. Moreover, the conversion extrapolates to zero at infinite flow rate when no CO_2 was co-fed. These observations are consistent with differential conversion of CO in the reactor and lack of any inhibition by product CO_2 under the conditions explored. The influence of flowrate on τ in Fig. 2.6 b is therefore attributed to product re-adsorption in the catalyst bed. Although increasing the flowrate through the reactor bed minimizes the influence of interparticle re-adsorption on τ, the flowrate does not impact re-adsorption of CO_2 within the catalyst pores. Thus, co-feeding an excess of $^{12}CO_2$ can be used to outcompete the re-adsorption of product $^{13}CO_2$ formed during a transient experiment.[35, 36] Interestingly, co-feeding a high level of CO_2 actually

inhibited the global steady-state rate (see Appendix Figs. A2 and A13), suggesting competitive adsorption on active sites, which will be discussed later. Extrapolating the τ values to infinite flowrate in the presence of co-fed CO_2 gives a value that is statistically close to zero (Fig. 2.6b), suggesting a high intrinsic turnover rate at 273 K that cannot be accurately quantified by this method. Nevertheless, using the result obtained at the highest measured flow rate and 4 % co-fed $^{12}CO_2$ (circled point in Fig. 6b) an estimated lower bound on the turnover frequency was calculated:

$$TOF = \frac{1}{\tau} = 0.3\ s^{-1} \tag{2}$$

A material balance on the reactor was used to estimate the upper bound on the number of adsorbed species that convert to product at the time of the switch, using the following equation involving τ and the steady-state rate of CO oxidation:

$$N_{CO_x} = \tau\ R_{CO_2} \tag{3}$$

The upper bound of coverage N_{COx} was calculated to be 10 % of the total Co in the sample as evaluated by elemental analysis. Clearly, the high global rate of low temperature CO oxidation on Co-N-C is attributed to the high intrinsic *TOF* with only a small portion of the Co being covered with intermediates leading to product.

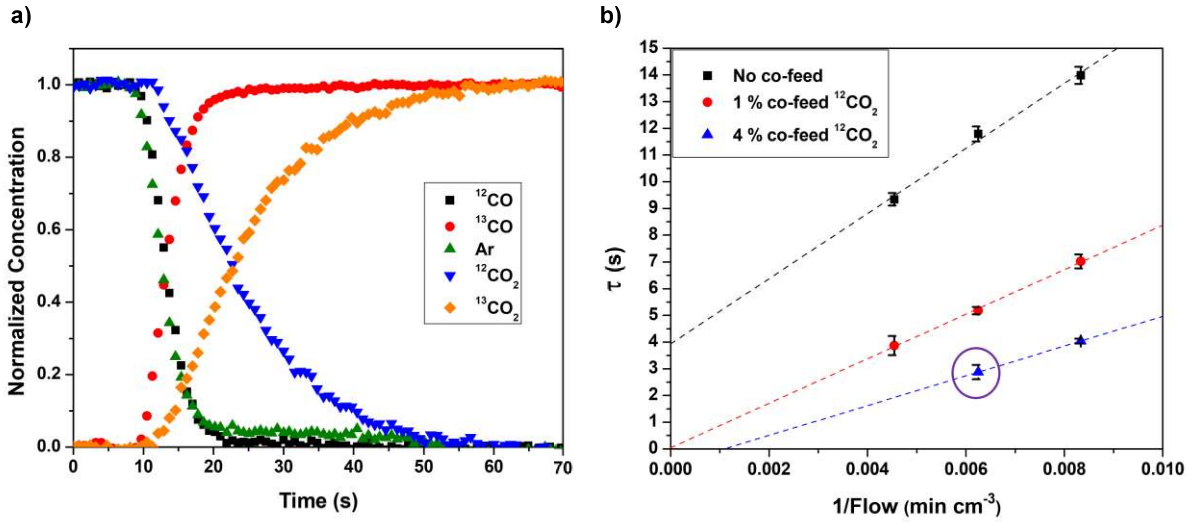

Figure 2.6. Example isotopic transient response following a switch from ^{12}CO and ^{13}CO during CO oxidation on Co-N-C.
a) Example isotopic transient response following a switch from ^{12}CO and ^{13}CO during CO oxidation on Co-N-C. The reaction was run with 30 mg of Co-N-C diluted in SiC and with 160 cm^3 total flow, 1 % CO, 1 % O_2, 1 % Ar, and balance He at 3 atm. The O_2 and CO lines were purified with silica traps submersed in a dry-ice acetone bath while the He and Ar lines were purified with an OMI Filter. The CO_2 line was purified by 3 Å molecular sieves. b) Effect of flow rate on the τ with various co-feed partial pressures of $^{12}CO_2$. The purple circled point was used to calculate lower bound of *TOF* and upper bound of N_{COX}. In b), the data points and error bars represent the average and standard deviation based on analysis of 3 to 6 transient response curves over a single catalyst.

2.3.4 Density Functional Theory Screening of Potential Active Sites and Mechanism

The kinetic data in Table 2.2 and the SSITKA results suggest that both CO and O_2 bind weakly to the active site. Figure 2.7 shows the vdW-DF functional computed CO and O_2 binding energies for Co-N-C sites in the graphene plane with zero to four N coordinated to the Co ion, implicated as active sites on these materials for both ORR and oxidative dehydrogenation reactions.[4, 9, 59, 60] Full computational details are provided in Methods Section 2.2. Increasing the number of N coordinated to Co generally leads to a reduction in binding energy of both CO and O_2. This result is consistent with previous reports that N substitutions for the C atoms that create

pyridinic binding modes to a transition metal center stabilizes the d-orbitals relative to the Fermi level and thus weakens binding energies of adsorbates.[45] Our results also indicate that the binding energy for CO and O_2 on CoN_4 are significantly weaker than CO on Pt (-155 kJ mol^{-1}), which has a negative CO order, in contrast to the positive CO order we observe on our Co-N-C catalyst.[61] The CoN_4 site is consistent with the Co^{2+} oxidation state from XPS (Fig. A6) and coordination number from EXAFS (Table 2.1), is very stable relative to other Co-N-C sites,[45, 49, 62] and fits the criterion for weak binding of both reactants. Thus, even if other Co sites coordinated to less than 4 N atoms are present as minority species in our catalyst, the strong binding energy of CO on these sites is inconsistent with the observed positive CO order and low coverage of CO as a reactive intermediate inferred from SSITKA, precluding their participation in the low temperature (< 400 K) catalytic cycle. Therefore, we next investigated the mechanism for low temperature CO oxidation over the CoN_4 site.

Previously calculated barriers for CO oxidation on various transition metals in N-C involve direct dissociation of O_2 over the metal center, which incurs large activation energies (i.e., 66 kJ mol^{-1} on CoN_4), and should alter the oxidation state of Co upon exposure to O_2.[38, 45] While the proposed mechanisms in those studies may explain the CO oxidation activity we observe at > 400 K (Fig. 2.3), they are incompatible with the activity and negative apparent activation energy observed in the low temperature kinetic regime, and also our prior in situ XAS results demonstrating no change in the Co oxidation state upon exposure to 10 % O_2 at 373 K.[9]

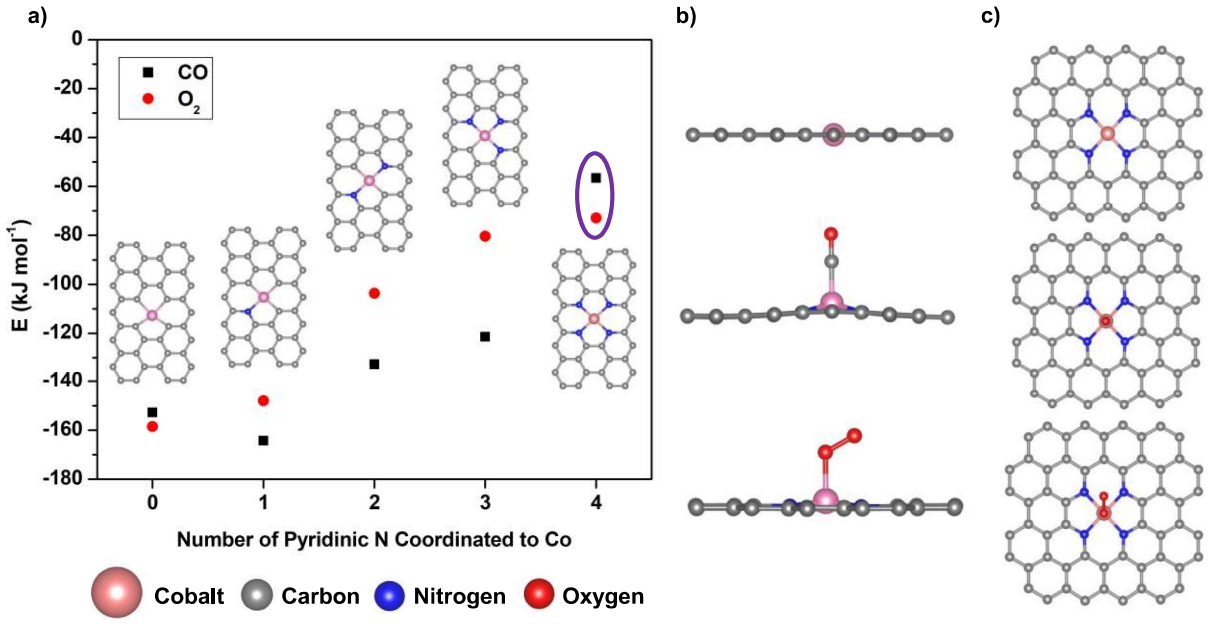

Figure 2.7. Adsorption energies were calculated using the vdW-DF functional because it shows good agreement with the experimental enthalpy of reaction for gas phase CO oxidation (Appendix Table A2).
The purple circle highlights the binding energies for the CoN_4 structure that is displayed in b) side view and c) top down.

To explore potential configurations for simultaneous adsorption of CO and O_2 we used NVT ab initio molecular dynamics (AIMD) starting from a supercell containing the CoN_4 site, one CO, and one O_2; AIMD details are in the Methods Section 2.2, and trajectories and movies are provided in a supplemental attachment and in Appendix Fig. A5. Early in the AIMD simulation CO binds to the CoN_4 site and one of the oxygen atoms in O_2 becomes weakly coordinated to CO. Surprisingly, the O-O bond distance then increased upon interaction with an adjacent C in the graphene sheet, until finally breaking, leaving behind a bent O-C-O complex bound through C to the Co, and one oxygen atom bound to carbon on the N-C support (O*). The O-C-O complex then rapidly desorbs from Co, forming a linear CO_2 molecule with no bonds to Co or the support. To complete the catalytic cycle, we ran a subsequent AIMD simulation starting from the previous

structure, removing the desorbed CO_2, and adding a CO molecule to the cell. The CO binds to the Co ion and subsequently reacts with O* to form CO_2 and desorb, completing the catalytic cycle. The formation of CO_2 during both AIMD simulations, without the use of enhanced sampling techniques to bias structures along a prescribed reaction coordinate, suggests that these reactions occur with very low activation barriers.

Due to the similar binding energies of CO and O_2, we also repeated these two AIMD simulations starting from O_2 adsorbed to the CoN_4 site and did not observe any reactions during these simulations. We did not observe co-adsorption of CO and O_2 to Co in any of our simulations, and geometry optimization of structures with both bound to Co resulted in desorption of either CO or O_2 depending on the initial structure. To determine if O_2 can bind to other surface sites in the absence of CO, we optimized structures with O_2 initially located on either graphitic C with only C nearest neighbors, a C atom with a N nearest neighbor, or a N atom. Regardless of the initial guess structure, the subsequent geometry optimization for all three potential binding sites led to either movement of the O_2 molecule to the Co site (yielding an analogous structure to that of O_2CoN_4, shown in Figure 2.7 b, c), or desorption of the O_2 molecule from the surface. Taken together, our results indicate that for CoN_4 the only two viable sites for O_2 adsorption are the Co atom or a CO molecule that is bound to Co, suggesting a possible CO oxidation mechanism over CoN_4 sites whereby O_2 dissociation is assisted by CO bound to Co and the N-C support itself.

Structures derived from the AIMD simulations were subsequently used for detailed calculations of the reaction coordinate. Figure 2.8 shows the resulting potential energy diagram, schematic representations, and vdW-DF computed structures. We report only energies and not free energies because the reaction intermediates are weakly adsorbed and not amenable to standard free energy approximations. Our AIMD simulation results and the similar binding energies of CO and

O_2 on CoN_4 (Fig. 2.7) suggest the mechanism initiates with CO adsorbed on CoN_4 (2). This is followed by weak interaction of O_2 with CO (3) and subsequent dissociation of O_2 upon interaction with the N-C support to form an O-O-C=O transition state (TS1) and subsequently O* and CO_2 (4). This reaction sequence is followed by adsorption of CO to Co (5). The reaction of Co-bound CO with O* has a barrier of only 0.2 kJ mol^{-1} (TS2), and CO_2 desorbs from Co (1) to close the catalytic cycle. Throughout this reaction cascade the 16 kJ mol^{-1} activation energy (TS1) is the only significant barrier.

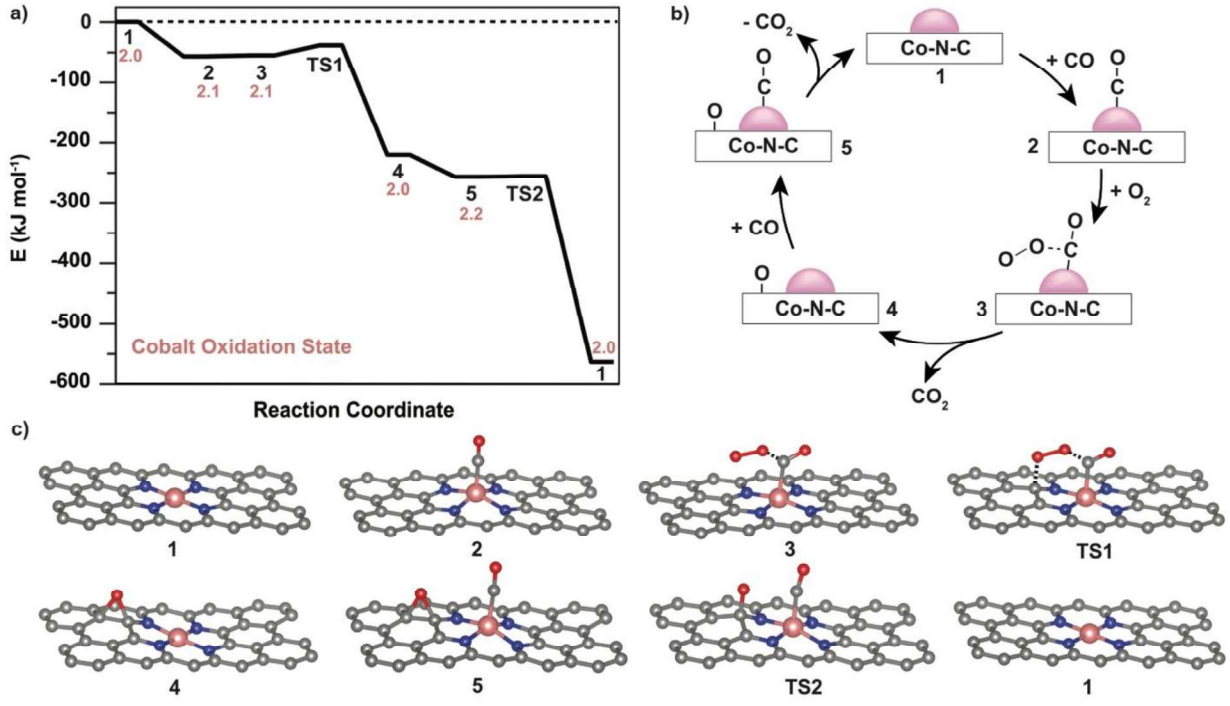

Figure 2.8. Schematic depicting reaction coordinates for the complete CO oxidation mechanism. a) vdW-DF computed reaction coordinate for the complete CO oxidation mechanism over CoN_4. b) Schematic of the complete catalytic cycle. c) Molecular structures corresponding to the reaction coordinate. Changes in the Co oxidation state were calculated using a normalized Bader charge analysis (Appendix Fig. A14).

Bader charge analysis (Fig. 2.8 a and Appendix Fig. A14) confirmed that the Co remained in a ~ 2+ oxidation state throughout the entire reaction mechanism. The lack of change in oxidation state indicates that Co does not undergo redox during the mechanism and is consistent with the lack of influence of gaseous environment on the Co K-edge XANES (CO or H_2 exposure in Fig. 2.5 and O_2 or H_2 exposure in reference 9).[9] The weak binding of CO and O_2 on the CoN_4 site is consistent with the positive experimental reaction orders and SSITKA results, and the low activation barrier for the rate determining step suggests that this reaction mechanism is plausible for CO oxidation in the low temperature (< 400 K) kinetic regime.

2.4 Discussion

The proposed reaction path is energetically downhill at every step and the elementary step involving O_2 activation (through transition state TS1) has a low barrier of 16 kJ mol^{-1} (Appendix Fig. A4 a). To explain the observed reaction kinetics (observed reaction orders and apparent negative activation energy), we need to account for the weak binding of reactants. The rate of the reaction step involving dioxygen activation (through TS-1) should be proportional to the overall reaction rate as the sequential oxidation of CO with the second oxygen atom is nearly barrierless (see results for TS-2 in Appendix Fig. A4b). Thus, we can write an expression for the observed rate as:

$$Rate = k[CO - O_2]_{ads} \quad (4)$$

where $[CO\text{-}O_2]_{ads}$ represents the surface concentration of the surface complex that is formed by adsorption of CO on Co followed by very weak adsorption of O_2 next to CO to give the structure depicted as 3 in Fig. 2.8. Although the results in Fig. 2.7 suggest that CO and O_2 will compete for binding on the Co site and subsequent MD simulations indicate only the adsorbed CO will lead to

reaction, the low coverages suggest that a first order model could be assumed. Thus, a standard Langmuir isotherm for competitive adsorption can be utilized to calculate the fractional coverage of CO on the hypothetical lattice of non-interacting Co sites (θ_{CO}) in the limit of low coverage of both CO and O_2:

$$\theta_{CO} = \frac{K_{CO}[CO]}{(1+K_{CO}[CO]+K_{O_2}[O_2])} = K_{CO}[CO] \quad (5)$$

where the K values represent the adsorption equilibrium constants of CO and O_2 on bare Co ions.

Likewise, the very weak adsorption of O_2 adjacent to the adsorbed CO is approximated by the linear portion of an adsorption isotherm, i.e. the adsorbed amount is proportional to the adsorption equilibrium constant of O_2 next to CO (K_{O2}') and the partial pressure of O_2. The observed rate is therefore approximated as:

$$r \propto k\, K_{CO} K'_{O_2} [CO][O_2] \quad (6)$$

which compares well the experimentally measured orders of reaction near unity for both CO and O_2. Using the expression in (6), the apparent activation energy (E_{apparent}) of the CO oxidation reaction can be evaluated from the barrier to form TS1 (E_a) and the heats of adsorption of CO adsorbed on Co and O_2 adsorbed adjacent to CO according to:

$$E_{\text{apparent}} = E_a + \Delta H_{CO} + \Delta H_{CO-O_2} = -41\ kJ\ mol^{-1} \quad (7)$$

Substituting the calculated barrier of O_2 activation through TS1 (16 kJ mol^{-1}) and the binding energies from the DFT calculations (-57 for CO on Co, and ~ 0 kJ mol^{-1} for O_2 adjacent to adsorbed CO) into (7), we estimate E_{apparent} = -41 kJ mol^{-1}, which is within reasonable agreement with the experimental value of -30 kJ mol^{-1} and is consistent with our proposed mechanism for low temperature CO oxidation.

Whereas we focused primarily on the low temperature mechanism of CO oxidation, the reaction at elevated temperature may proceed through a high barrier path that was previously reported by Mavrikakis and co-workers.[45] Their mechanism involves dissociation of O_2 on the subsequently oxidized Co site prior to reacting with CO to form two CO_2 molecules. In addition, a small number of undetected Co oxide particles may also be present on the surface of Co-N-C, which could catalyze CO oxidation at elevated temperatures via the MvK mechanism known to occur with Co oxide. [27, 28, 63-66]

We realize that a simplified kinetic analysis has been applied to the low temperature regime, but the model accounts for the key features of the reaction, namely the nearly first order behavior in both CO and O_2 and a negative apparent activation energy. In this model, lower temperatures increase the number of adsorbed species on the surface without compromising the fast rate of O_2 activation. In other words, the implication of a very low barrier for O_2 activation is that the observed rate is dictated primarily by the number of adsorbed intermediates that lead to product. Furthermore, the proposed mechanism for low temperature CO oxidation over Co-N-C catalysts involves the CO-assisted activation of O_2 through a O-O-C=O transition state that is similar to that proposed previously for the reaction occurring on CO-saturated Pt clusters at much higher temperatures. Under reaction conditions that saturate a Pt surface with CO, the unavailability of adjacent surface vacancies on the Pt prevents dissociative chemisorption of O_2 on the catalyst.[67] The reaction under those conditions is therefore proposed to proceed through a CO-assisted O_2 dissociation step involving the decomposition of an O-O-C=O surface intermediate to give CO_2 and a surface oxygen atom, which rapidly reacts with adsorbed CO to form another CO_2.[67] The barriers to form and react the proposed intermediate are quite low, consistent with the results reported here. The mechanism presented in our study is also comparable

to that proposed for CO oxidation on Au stepped surfaces whereby O_2 weakly binds to Au in the presence of adsorbed CO to form an O_2-CO surface intermediate that can subsequently decomposes to form CO_2.[68] To the best of our knowledge, these types of reactive intermediates have not been proposed previously for the low temperature oxidation of CO over Co-N-C type materials.

We attribute the low coverage of reactive intermediates leading to product, as revealed by SSITKA, to the weak binding energy of reactants to the isolated Co ions and relatively low partial pressures used in the study. Although there may be multiple motifs for Co to reside on Co-N-C, the CoN_4 motif that is often proposed to be the majority species in M-N-C catalysts is entirely consistent with all of the observations reported in this work. Thus, we do not need to invoke the presence of a trace species of Co to account for the observations.

We realize the above model does not include any potential inhibition by CO_2. As shown in Fig. A2, inhibition by CO_2 is not observed when the conversion of CO is differential and CO_2 is not co-fed. When the concentration of CO_2 was co-fed at orders of magnitude higher levels, there was an inhibitory effect on the rate as summarized in Fig. A13. This observation is entirely consistent with the model discussed above as high pressures of CO_2 are expected to eventually compete for Co sites. In other words, the expression for θ_{CO} in Equation 5 can be easily modified to include competitive adsorption of CO_2 on the Co sites. In addition, the presence of high levels of CO_2 could inhibit the weak interaction of O_2 with CO during the formation of the O-O-C=O surface complex.

2.5 Conclusions

Our results suggest that isolated Co ions doped into nitrogen-carbon can utilize reductant molecules to activate O_2 via the surrounding carbon support at low temperatures. Further, both our calculations and experiments suggest Co maintains a 2+ oxidation state upon exposure to the reaction gas mixture or individual components of it, completing the catalytic reaction without undergoing a redox cycle between Co^{2+} and Co^{3+}. Since the metal ion is not required to undergo a redox cycle to facilitate the reaction, we anticipate that further studies on other metal ions in N-C could yield similar results.

Acknowledgements

This research was sponsored by the U.S. National Science Foundation under grant # CBET-1802482. C.P. acknowledges the donors of the American Chemical Society Petroleum Research Fund for partial support of this research. This research used beamline 8-ID of the National Synchrotron Light Source II, a U.S. Department of Energy (DOE) Office of Science User Facility operated for the DOE Office of Science by Brookhaven National Laboratory under Contract No. DE-SC0012704. Dr. Eli Stavitski provided technical assistance with operating beamline 8-ID. Scanning Transmission Electron Microscopy research was conducted as part of a user project at the Center for Nanophase Materials Sciences (CNMS), which is a US Department of Energy, Office of Science User Facility at Oak Ridge National Laboratory. Helpful technical discussions with Sugandha Verma and Dr. Gordon Brezicki are also acknowledged.

2.6 References

1. Liang, H. W.; Wei, W.; Wu, Z. S.; Feng, X.; Müllen, K. Mesoporous Metal-Nitrogen-Doped Carbon Electrocatalysts for Highly Efficient Oxygen Reduction Reaction. *J. Am. Chem. Soc.* **2013,** *135* (43), 16002-16005.

2. Liu, Q.; Zhang, J. Graphene Supported Co-g-C_3N_4 as a Novel Metal-Macrocyclic Electrocatalyst for the Oxygen Reduction Reaction in Fuel Cells. *Langmuir* **2013,** *29* (11), 3821-3828.

3. Malko, D.; Kucernak, A.; Lopes, T. In Situ Electrochemical Quantification of Active Sites in Fe-N/C Non-Precious Metal Catalysts. *Nat. Commun.* **2016,** *7*, 1-7.

4. Zitolo, A.; Ranjbar-Sahraie, N.; Mineva, T.; Li, J.; Jia, Q.; Stamatin, S.; Harrington, G. F.; Lyth, S. M.; Krtil, P.; Mukerjee, S.; Fonda, E.; Jaouen, F. Identification of Catalytic Sites in Cobalt-Nitrogen-Carbon Materials for the Oxygen Reduction Reaction. *Nat. Commun.* **2017,** *8*, 957.

5. Zhang, Q.; Mamtani, K.; Jain, D.; Ozkan, U.; Asthagiri, A. CO Poisoning Effects on FeNC and CN_x ORR Catalysts: A Combined Experimental–Computational Study. *J. Phys. Chem. C* **2016,** *120* (28), 15173-15184.

6. Jain, D.; Zhang, Q.; Hightower, J.; Gustin, V.; Asthagiri, A.; Ozkan, U. S. Changes in Active Sites on Nitrogen-Doped Carbon Catalysts Under Oxygen Reduction Reaction: A Combined Post-Reaction Characterization and DFT Study. *ChemCatChem* **2019,** *11* (24), 5945-5950.

7. Vijay, S.; Ju, W.; Brückner, S.; Tsang, S. C.; Strasser, P.; Chan, K. Unified Mechanistic Understanding of CO_2 Reduction to CO on Transition Metal and Single Atom Catalysts. *Nat. Catal.* **2021,** *4*, 1024-1031.

8. Xie, J.; Yin, K.; Serov, A.; Artyushkova, K.; Pham, H. N.; Sang, X.; Unocic, R. R.; Atanassov, P.; Datye, A. K.; Davis, R. J. Selective Aerobic Oxidation of Alcohols over Atomically-Dispersed Non-Precious Metal Catalysts. *ChemSusChem* **2017,** *10* (2), 359-362.

9. Xie, J.; Kammert, J. D.; Kaylor, N.; Zheng, J. W.; Choi, E.; Pham, H. N.; Sang, X.; Stavitski, E.; Attenkofer, K.; Unocic, R. R.; Datye, A. K.; Davis, R. J. Atomically Dispersed Co and Cu on N-Doped Carbon for Reactions Involving C–H Activation. *ACS Catal.* **2018,** *8* (5), 3875-3884.

10. Huang, K.; Fu, H.; Shi, W.; Wang, H.; Cao, Y.; Yang, G.; Peng, F.; Wang, Q.; Liu, Z.; Zhang, B.; Yu, H. Competitive Adsorption on Single-Atom Catalysts: Mechanistic Insights into the Aerobic Oxidation of Alcohols over Co–N–C. *J. Catal.* **2019,** *377*, 283-292.

11. Liao, C.; Li, X.; Yao, K.; Yuan, Z.; Chi, Q.; Zhang, Z. Efficient Oxidative Dehydrogenation of N-Heterocycles over Nitrogen-Doped Carbon-Supported Cobalt Nanoparticles. *ACS Sustain. Chem. Eng.* **2019,** *7* (16), 13646-13654.

12. Li, J.; Liu, J.; Zhang, J.; Wan, T.; Huang, L.; Wang, X.; Pan, R.; An, Z.; Vlachos, D. G. An Unconventional DCO_x Favored Co/N-C Catalyst for Efficient Conversion of Fatty Acids and Esters to Liquid Alkanes. *Appl. Catal., A* **2020,** *591*, 117385-117394.

13. Shao, M.; Chang, Q.; Dodelet, J.-P.; Chenitz, R. Recent Advances in Electrocatalysts for Oxygen Reduction Reaction. *Chem. Rev.* **2016,** *116* (6), 3594-3657.

14. Wang, J.; You, R.; Zhao, C.; Zhang, W.; Liu, W.; Fu, X. P.; Li, Y.; Zhou, F.; Zheng, X.; Xu, Q.; Yao, T.; Jia, C. J.; Wang, Y. G.; Huang, W.; Wu, Y. N-Coordinated Dual-Metal Single-Site Catalyst for Low-Temperature CO Oxidation. *ACS Catal.* **2020,** *10* (4), 2754-2761.

15. Luo, F.; Choi, C. H.; Primbs, M. J. M.; Ju, W.; Li, S.; Leonard, N. D.; Thomas, A.; Jaouen, F.; Strasser, P. Accurate Evaluation of Active-Site Density (SD) and Turnover Frequency

(TOF) of PGM-Free Metal-Nitrogen-Doped Carbon (MNC) Electrocatalysts using CO Cryo Adsorption. *ACS Catal.* **2019,** *9* (6), 4841-4852.

16. Luo, F.; Wagner, S.; Onishi, I.; Selve, S.; Li, S.; Ju, W.; Wang, H.; Steinberg, J.; Thomas, A.; Kramm, U. I.; Strasser, P. Surface Site Density and Utilization of Platinum Group Metal (PGM)-Free Fe-NC and FeNi-NC Electrocatalysts for the Oxygen Reduction Reaction. *Chem. Sci.* **2021,** *12*, 384-396.

17. Bamwenda, G. R.; Tsubota, S.; Nakamura, T.; Haruta, M. The Influence of the Preparation Methods on the Catalytic Activity of Platinum and Gold Supported on TiO_2 for CO Oxidation. *Catal. Lett.* **1997,** *44*, 83-87.

18. Berlowitz, P. J.; Peden, C. H. F.; Goodman, D. W. Kinetics of CO Oxidation on Single-Crystal Pd, Pt, and Ir. *J. Phys. Chem.* **1988,** *92* (18), 5213-5221.

19. Mars, P.; van Krevelen, D. W. Oxidations Carried out by Means of Vanadium Oxide Catalysts. *Chem. Eng. Sci.* **1954,** *3*, 41-59.

20. Close, J. S.; White, J. M. On the Oxidation of Carbon Monoxide Catalyzed by Palladium. *J. Catal.* **1975,** *36* (2) 185-198.

21. Lu, Y.; Wang, J.; Yu, L.; Kovarik, L.; Zhang, X.; Hoffman, A. S.; Gallo, A.; Bare, S. R.; Sokaras, D.; Kroll, T.; Dagle, V.; Xin, H.; Karim, A. M. Identification of the Active Complex for CO Oxidation over Single-Atom Ir-on-$MgAl_2O_4$ Catalysts. *Nat. Catal.* **2019,** *2*, 149-156.

22. Haruta, M. Size- and Support-Dependency in the Catalysis of Gold. *Catal. Today* **1997,** *36* (1), 153-166.

23. Haruta, M.; Kobayashi, T.; Sano, H.; Yamada, N. Novel Gold Catalysts for the Oxidation of Carbon Monoxide at a Temperature far Below 0 °C. *Chem. Lett.* **1987,** *16* (2). 405-408.

24. Haruta, M.; Tsubota, S.; Kobayashi, T.; Kageyama, H.; Genet, M. J.; Delmon, B. Low-Temperature Oxidation of CO over Gold Supported on TiO_2, α-Fe_2O_3, and Co_3O_4. *J. Catal.* **1993,** *144* (1), 175-192.

25. Jansson, J.; Palmqvist, A. E. C.; Fridell, E.; Skoglundh, M.; Österlund, L.; Thormählen, P.; Langer, V. On the Catalytic Activity of Co_3O_4 in Low-Temperature CO Oxidation. *J. Catal.* **2002,** *211* (2), 387-397.

26. Zheng, J.; Chu, W.; Zhang, H.; Jiang, C.; Dai, X. CO Oxidation over Co_3O_4/SiO_2 Catalysts : Effects of Porous Structure of Silica and Catalyst Calcination Temperature. *J. Nat. Gas Chem.* **2010,** *19* (6), 583-588.

27. Gu, D.; Jia, C. J.; Weidenthaler, C.; Bongard, H. J.; Spliethoff, B.; Schmidt, W.; Schüth, F. Highly Ordered Mesoporous Cobalt-Containing Oxides: Structure, Catalytic Properties, and Active Sites in Oxidation of Carbon Monoxide. *J. Am. Chem. Soc.* **2015,** *137* (35), 11407-11418.

28. Baidya, T.; Murayama, T.; Nellaiappan, S.; Katiyar, N. K.; Bera, P.; Safonova, O.; Lin, M.; Priolkar, K. R.; Kundu, S.; Srinivasa Rao, B.; Steiger, P.; Sharma, S.; Biswas, K.; Pradhan, S. K.; Lingaiah, N.; Malviya, K. D.; Haruta, M. Ultra-Low-Temperature CO Oxidation Activity of Octahedral Site Cobalt Species in Co_3O_4 Based Catalysts: Unravelling the Origin of the Unique Catalytic Property. *J. Phys. Chem. C* **2019,** *123* (32), 19557-19571.

29. Cai, Y.; Xu, J.; Guo, Y.; Liu, J. Ultrathin, Polycrystalline, Two-Dimensional Co_3O_4 for Low-Temperature CO Oxidation. *ACS Catal.* **2019,** *9* (3), 2558-2567.

30. Jagadeesh, R. V.; Junge, H.; Pohl, M.-m.; Radnik, J.; Bru, A.; Beller, M. Selective Oxidation of Alcohols to Esters Using Heterogeneous Co_3O_4−N@C Catalysts under Mild Conditions. *J. Am. Chem. Soc.* **2013,** *135* (29), 10776-10782.

31. Lam, Y. L.; Boudart, M. Preparation of Small Au-Pd Particles on Silica. *J. Catal.* **1977,** *50* (3), 530-540.

32. Kaylor, N.; Xie, J.; Kim, Y.-S.; Pham, H. N.; Datye, A. K.; Lee, Y.-K.; Davis, R. J. Vapor Phase Deoxygenation of Heptanoic Acid over Silica-Supported Palladium and Palladium-Tin Catalysts. *J. Catal.* **2016,** *344*, 202-212.

33. Kammert, J. D.; Brezicki, G.; Acevedo-Esteves, R.; Stavitski, E.; Davis, R. J. High-Throughput Operando-Ready X-ray Absorption Spectroscopy Flow Reactor Cell for Powder Samples. *Rev. Sci. Instrum.* **2020,** *91,* 013107.

34. Ravel, B.; Newville, M. ATHENA, ARTEMIS, HEPHAESTUS: Data Analysis for X-ray Absorption Spectroscopy using IFEFFIT. *J. Synchrotron Radiat.* **2005,** *12*, 537-541.

35. Shannon, S. L.; Goodwin, J. G. Characterization of Catalytic Surfaces by Isotopic-Transient Kinetics during Steady-State Reaction. *Chem. Rev.* **1995,** *95* (3) 677-695.

36. Calla, J.; Bore, M.; Datye, A.; Davis, R. Effect of Alumina and Titania on the Oxidation of CO over Au Nanoparticles Evaluated by ^{13}C Isotopic Transient Analysis. *J. Catal.* **2006,** *238* (2), 458-467.

37. Kresse, G.; Furthmuller, J. Efficient Iterative Schemes for Ab Initio Total-Energy Calculations using a Plane-Wave Basis Set. *J. Phys. Rev. B* **1996,** *54* (16), 11169-11186.

38. Deng, Q.; Zhao, L.; Gao, X.; Zhang, M.; Luo, Y.; Zhao, Y. Single Layer of Polymeric Cobalt Phthalocyanine: Promising Low-Cost and High-Activity Nanocatalysts for CO Oxidation. *Small* **2013,** *9* (20), 3506-3513.

39. Patel, A. M.; Ringe, S.; Siahrostami, S.; Bajdich, M.; Nørskov, J. K.; Kulkarni, A. R. Theoretical Approaches to Describing the Oxygen Reduction Reaction Activity of Single-Atom Catalysts. *J. Phys. Chem. C* **2018,** *122* (51), 29307-29318.

40. Dion, M.; Rydberg, H.; Schroder, E.; Langreth, D. C.; Lundqvist, B. I. van der Waals Density Functional for General Geometries. *Phys. Rev. Lett.* **2004,** *92,* 246401.

41. Perdew, J. P.; Wang, Y. Accurate and Simple Analytic Representation of the Electron-Gas Correlation Energy. *Phys. Rev. B* **1992,** *45* (23), 13244-13249.

42. Lee, K.; Murray, É. D.; Kong, L.; Lundqvist, B. I.; Langreth, D. C. Higher-Accuracy van der Waals Density Functional. *Phys. Rev. B* **2010,** *82*, 3-6.

43. Henkelman, G.; Uberuaga, B. P.; Josson, H. A Climbing Image Nudged Elastic Band Method for Finding Saddle Points and Minimum Energy Paths and Minimum Energy Paths. *J. Chem. Phys.* **2000,** *113*, 9901-9904.

44. Henkelman, G.; Josson, H. Improved Tangent Estimate in the Nudged Elastic Band Method for Finding Minimum Energy Paths and Saddle Points. *J. Chem. Phys.* **2000,** *133*, 9978-9985.

45. Kropp, T.; Mavrikakis, M. Transition Metal Atoms Embedded in Graphene: How Nitrogen Doping Increases CO Oxidation Activity. *ACS Catal.* **2019,** *9* (8), 6864-6868.

46. Liu, W.; Zhang, L.; Yan, W.; Liu, X.; Yang, X.; Miao, S.; Wang, W.; Wang, A.; Zhang, T. Single-Atom Dispersed Co-N-C Catalyst: Structure Identification and Performance for Hydrogenative Coupling of Nitroarenes. *Chem. Sci.* **2016,** *7* (9), 5758-5764.

47. Biesinger, M. C.; Payne, B. P.; Grosvenor, A. P.; Lau, L. W. M.; Gerson, A. R.; Smart, R. S. C. Resolving Surface Chemical States in XPS Analysis of First Row Transition Metals, Oxides and Hydroxides: Cr, Mn, Fe, Co and Ni. *Appl. Surf. Sci.* **2011,** *257* (7), 2717-2730.

48. Haque, E.; Zavabeti, A.; Uddin, N.; Wang, Y.; Rahim, M. A.; Syed, N.; Xu, K.; Jannat, A.; Haque, F.; Zhang, B. Y.; Shoaib, M. A.; Shamsuddin, S.; Nurunnabi, M.; Minett, A. I.;

Ou, J. Z.; Harris, A. T. Deciphering the Role of Quaternary N in O_2 Reduction over Controlled N-Doped Carbon Catalysts. *Chem. Mater.* **2020,** *32* (4), 1384-1392.

49. Ebikade, E. O.; Wang, Y.; Samulewicz, N.; Hasa, B.; Vlachos, D. Active Learning-Driven Quantitative Synthesis–Structure–Property Relations for Improving Performance and Revealing Active Sites of Nitrogen-Doped Carbon for the Hydrogen Evolution Reaction. *React. Chem. Eng.* **2020,** *5* (12), 2134-2147.

50. Sun, Y.; Li, S.; Jovanov, Z. P.; Bernsmeier, D.; Wang, H.; Paul, B.; Wang, X.; Kühl, S.; Strasser, P. Structure, Activity, and Faradaic Efficiency of Nitrogen-Doped Porous Carbon Catalysts for Direct Electrochemical Hydrogen Peroxide Production. *ChemSusChem* **2018,** *11* (19), 3388-3395.

51. Wang, Y.; Chen, Z.; Fang, R.; Li, Y. Hollow-Co_3O_4@Co_3O_4@SiO_2 Multi-Yolk-Double-Shell Nanoreactors for Highly Efficient CO Oxidation. *ChemCatChem* **2019,** *11* (2), 772-779.

52. Iablokov, V.; Barbosa, R.; Pollefeyt, G.; Van Driessche, I.; Chenakin, S.; Kruse, N. Catalytic CO Oxidation over Well-Defined Cobalt Oxide Nanoparticles: Size-Reactivity Correlation. *ACS Catal.* **2015,** *5* (10), 5714-5718.

53. Calla, J. T.; Davis, R. J., Influence of Dihydrogen and Water Vapor on the Kinetics of CO Oxidation over Au/Al_2O_3. *Ind. Eng.Chem. Res.* **2005,** *44*, 5403-5410.

54. Daté, M.; Okumura, M.; Tsubota, S.; Haruta, M. Vital Role of Moisture in the Catalytic Activity of Supported Gold Nanoparticles. *Angew. Chem. Int. Ed.* **2004,** *43* (16), 2129-2132.

55. Saavedra, J.; Doan, H. A.; Pursell, C. J.; Grabow, L. C.; Chandler, B. D. The Critical Role of Water at the Gold-Titania Interface in Catalytic CO Oxidation. *Science* **2014,** *345* (6204), 1599-1602.

56. Jin, Y.; Sun, G.; Xiong, F.; Wang, Z.; Huang, W. Proton-Transfer-Connected Elementary Surface Reaction Network for Low-Temperature CO Oxidation Catalyzed by Metal-Oxide Nanocatalysts. *J. Phys. Chem. C* **2016,** *120* (47) 26968-26973.

57. Perti, D; Kabel, R. L. Kinetics of CO Oxidation Over Co_3O_4/Al_2O_3. *AIChE J.* **1985,** *31* (9), 1420-1426.

58. Lukashuk, L.; Yigit, N.; Rameshan, R.; Kolar, E.; Teschner, D.; Hävecker, M.; Knop-Gericke, A.; Schlögl, R.; Föttinger, K.; Rupprechter, G. Operando Insights into CO Oxidation on Cobalt Oxide Catalysts by NAP-XPS, FTIR, and XRD. *ACS Catal.* **2018,** *8* (9), 8630-8641.

59. Gadipelli, S.; Zhao, T.; Shevlin, S. A.; Guo, Z. Switching Effective Oxygen Reduction and Evolution Performance by Controlled Graphitization of a Cobalt–Nitrogen–Carbon Framework System. *Energy Environ. Sci.* **2016,** *9*, 1661-1667.

60. Xie, X.; He, C.; Li, B.; He, Y.; Cullen, D. A.; Wegener, E. C.; Kropf, A. J.; Martinez, U.; Cheng, Y.; Engelhard, M. H.; Bowden, M. E.; Song, M.; Lemmon, T.; Li, X. S.; Nie, Z.; Liu, J.; Myers, D. J.; Zelenay, P.; Wang, G.; Wu, G.; Ramani, V.; Shao, Y. Performance Enhancement and Degradation Mechanism Identification of a Single-Atom Co–N–C Catalyst for Proton Exchange Membrane Fuel Cells. *Nat. Catal.* **2020,** *3* (12), 1044-1054.

61. Koper, M. T. M.; Shubina, T. E.; Santen, R. A. V. Periodic Density Functional Study of CO and OH Adsorption on Pt-Ru Alloy Surfaces: Implications for CO Tolerant Fuel Cell Catalysts. **2002**, *106,* 686-692.

62. Kattel, S.; Wang, G. Reaction Pathway for Oxygen Reduction on FeN_4 Embedded Graphene. *J. Phys. Chem. B* **2014,** *106* (3), 452-6.

63. Molavi, R.; Safaiee, R.; Sheikhi, M. H.; Hassani, N. Theoretical Perspective on CO Oxidation over Small Cobalt Oxide Clusters. *Chem. Phys. Lett.* **2021,** *767* (16), 138361.

64. Broqvist, P.; Panas, I.; Persson, H. A DFT Study on CO Oxidation over Co_3O_4. *J. Catal*. **2002,** *210* (1), 198-206.

65. Xie, Y.; Dong, F.; Heinbuch, S.; Rocca, J. J.; Bernstein, E. R. Oxidation Reactions on Neutral Cobalt Oxide Clusters: Experimental and Theoretical Studies. *Phys. Chem. Chem. Phys.* **2010,** *12* (4), 947-959.

66. Xu, X. L.; Li, J. Q. DFT Studies on H_2O Adsorption and its Effect on CO Oxidation over Spinel Co_3O_4 (110) Surface. *Surf. Sci.* **2011,** *605* (23), 1962-1967.

67. Allian, A. D.; Takanabe, K.; Fujdala, K. L.; Hao, X.; Truex, T. J.; Cai, J.; Buda, C.; Neurock, M.; Iglesia, E. Chemisorption of CO and Mechanism of CO Oxidation on Supported Platinum Nanoclusters. *J. Am. Chem. Soc.* **2011,** *133* (12), 4498-4517.

68. Liu, Z. P.; Hu, P.; Alavi, A. Catalytic Role of Gold in Gold-Based Catalysts: A Density Functional Theory Study on the CO Oxidation on Gold. *J. Am. Chem. Soc.* **2002,** *124* (49), 14770-14779.

Chapter 3 Low Temperature CO Oxidation over Rh Supported on N-Doped Carbon

Abstract

As discussed in Chapter 2, a mechanism for CO oxidation at temperatures as low as 196 K was proposed for isolated Co ions in nitrogen-doped carbon (Co-N-C) but it was unclear if this mechanism was applicable to other transition metals (M-N-Cs). The low barrier mechanism for CO oxidation progressed by a weakly adsorbed CO molecule assisting activation of O_2 with the carbon support without redox on the transition metal. The weak adsorption and lack of redox on the metal center indicates that the mechanism may be applicable to other M-N-Cs. In this work, the screening of various M-N-Cs using quantum chemical calculations revealed that transition metals in the same column as Co could bind CO in a range that is competitive with O_2 on the surface and also could form a stable CO-O_2 intermediate. A Rh-N-C catalyst was synthesized to determine if it did indeed have low temperature activity for CO oxidation. Steady-state CO oxidation at low temperature over Rh-N-C had positive reaction orders in both CO and O_2 with nearly zero apparent activation energy. Results from kinetic experiments and quantum chemical calculations are consistent with a reaction path involving weak adsorption of CO onto Rh ions with turnover coming from CO-assisted activation of weakly adsorbed O_2. The mechanism was similar to the previously reported mechanism for CO oxidation on Co-N-C and thus appears to be general in nature and may be useful for the design of other catalysts for reactions involving O_2 activation.

3.1 Introduction

Transition metal ions (M) isolated in a nitrogen-doped carbon matrix (M-N-C) have demonstrated activity for reactions involving molecular oxygen in both electrocatalytic[1-6] and thermocatalytic[7-11] processes but the coordination environment around the isolated metal center and the mechanism for O_2 activation remain controversial.[7-9, 11] Oxidation of CO through O_2 activation has been studied over M-N-C catalysts since the reaction lacks complicating effects such as solvents and applied potentials.[11, 12] Specifically, catalytic CO oxidation was investigated on Fe-N-C, Co-N-C, and materials containing with both Co and Fe (Co,Fe-N-C), with the Co-containing catalysts exhibiting activity even at dry-ice acetone temperature.[12] In that work, the low-temperature activity was attributed to weak but preferential binding of CO to Co with O_2 binding on the adjacent Fe.[12] In a related study, results from CO pulse cryo-chemisorption showed that CO chemisorbed on Fe-N-C and Fe,Ni-N-C catalysts whereas CO did not chemisorb on Ni-N-C.[13, 14] Clearly, CO adsorption and O_2 activation are highly dependent on the nature of the transition metal element in M-N-C materials.

We recently used kinetic measurements, ab initio quantum chemical calculations, and molecular dynamics simulations to study a Co-N-C catalyst for low temperature CO oxidation.[11] Results from that work are consistent with a mechanism for O_2 activation that avoids direct dissociation of O_2 on the transition metal ion.[11] Instead, weak adsorption of CO onto Co ions followed by CO-assisted activation of weakly adsorbed O_2 with the carbon support produced CO_2 in a reaction path with an apparent activation energy that is negative.[11] Interestingly, the proposed mechanism did not involve a redox cycle on the isolated Co metal ion.[11] The absence of a redox

cycle on the metal and the weak interactions of the reactants with the isolated transition metal ion suggests that other M-N-C catalysts may also be active for CO oxidation at low temperatures.

A variety of M-N-C catalysts have been synthesized (i.e. Ag, Au, Cd, Cr, Cu, Fe, Ir, Mn, Ni, Pd, Pt, Rh, Ru, and Zn) and their activity and stability in O_2 activation reactions varies accordingly.[15] For example, Cr, Co, and Cu N-C materials exhibited high initial catalytic activity for the oxidative dehydrogenation of benzyl alcohol, but the activity for the Cu samples was not recovered upon recycle or regeneration.[7] Evidently, although M-N-Cs with various transition metals can be synthesized, not all of them may be stable under catalytic conditions. The stability of M-N-C structures was investigated by quantum chemical calculations using the formation energy of transition metals in graphite and N-doped structures.[16] The study showed that many M-N-Cs in the same N-doped double vacancy motif that we previously studied are stable.[16] The stability of other metals indicate that other M-N-Cs could be synthesized, explored for low temperature CO oxidation, and compared to DFT calculations mechanisms.

In this study, we computationally screened various reportedly stable M-N-C catalysts to determine CO and O_2 adsorption energy trends that might enable the low-temperature activation of O_2 on various M-N-C catalysts. Rhodium ions in N-doped carbon (Rh-N-C) as well as Ir ions in N-doped carbon (Ir-N-C) are predicted to activate O_2 through a mechanism similar to that described in our previous publication on Co-N-C (Chapter 2).[11] To confirm the mechanism descriptors are correct in predicting a mechanism for CO oxidation on metals, we chose to synthesize Rh-N-C and tested it in low temperature CO oxidation. The low temperature CO oxidation kinetics are consistent with our computationally derived mechanism with CO-assisting the activation of O_2 with the participation of the carbon matrix.

3.2 Methods

3.2.1 Quantum Chemical Density Functional Theory Calculations

We performed spin-polarized periodic supercell density functional theory (DFT) calculations with a plane wave basis set and an energy cutoff of 500 eV using the Vienna ab initio simulation package (VASP)[17] version 5.4.4. For all structures, convergence criteria of 10^{-6} eV and 0.01 eV $Å^{-1}$ for self-consistent-field (SCF) energies and atomic forces, respectively, were used. Structures in various graphene supercell sizes may have different adsorbate binding energies so two different cell sizes were generated to compare to the literature. An 8.5 Å by 9.8 Å graphene supercell with 14 Å vacuum in the z-direction with two adjacent carbon vacancies to add in the metal ion (corresponding to a density of 1 M per 0.8 nm^2) was generated by using a total of 30 C atoms (when the number of nitrogen atoms is zero). The carbon atoms surrounding the metal added to the defect site were then substituted with 4 pyridinic N atoms. A previous study used a supercell with less M density (1 M per 1.3 nm^2)[16], thus for comparison we generated a graphene supercell with 58 C (without N substitutions) and 15 Å vacuum in the z-direction. All of the structure files for optimized geometries are included as Supplemental Files submitted with this dissertation. Monkhorst-Pack *k*-points were used with a 4 X 4 X 1 mesh since they were the optimized k-points for the small cell (Appendix Fig. B1). A variety of metals were used so the spin states for each were checked by doing an optimization starting from a low spin state on the entire structure by setting NUPDOWN to 0 and then doing a second optimization starting from a high spin state on the metal by setting MAGMOM to 5 for just the metal atom. Geometry optimizations for O_2 adsorption were started from both bidentate and monodentate initial configurations, and the more exothermic binding mode after geometry optimization is reported here. Only energies are reported

and not free energies since the reaction intermediates have been shown previously to weakly adsorb in the case of Co ions doped in nitrogen-carbon (Co-N-C)[11] and thus are not amenable to standard free energy approximations. Vibrational zero-point energy corrections were neglected to reduce computational costs as they are expected to have a negligible contribution to reaction energies for our system. Mavrikakis and co-workers[16] reported binding energies of CO and O_2 on a variety of metals calculated with the Perdew, Burke, and Ernzerhof (PBE)[18] functional and the previously described larger supercell. Our PBE computed adsorption energies were analogous to theirs (Appendix Table B1), with the exception of CO binding to Fe-N-C. Our computed binding energy for CO on Fe-N-C is more exothermic but has a value that is consistent with other PBE-computed binding energies for CO on Fe-N-C.[19-21] Finally, we chose to report van der Waals density functional (vdW-DF)[22] computed values in the main text (PBE values are reported in Appendix Table B1 for comparison) because this functional reproduces the experimental enthalpy of reaction for gas-phase CO oxidation,[11] was previously benchmarked for the binding energy of CO on Co-N-C,[11] and accounts for nonlocal electron correlation dispersion interactions that are important for weak adsorption.

Transition states for the CO oxidation reaction on Rh-N-C structures were determined using climbing image nudged elastic band (CI-NEB) calculations derived from the method of Henkelman et al. and are reported in Appendix Fig. B2.[23, 24] The transition state calculations were completed using the higher metal density structures (small supercell) since for Rh-N-C the binding energies were within 15 kJ mol^{-1} of each other (-68 and -68 kJ mol^{-1} for CO and O_2 respectively in the higher metal density cell and -54 and -60 kJ mol^{-1} respectively for the lower metal density cell). For transition state one (TS1), we investigated multiple spin states and found that although the barrier is sensitive to spin and typically decreases with lower spin, the reactant binding energies

only weakly vary with the spin state (Appendix Fig. B3). Therefore, we report the low spin reaction coordinate (magnetic moment = 0 for the whole structure) for the CI-NEB for TS1.

3.2.2 Synthesis of Rh Catalysts

The Rh-N-C catalyst was synthesized by a modified high-temperature pyrolysis method similar to previously used methods.[8, 11, 25] A solution of Rh nitrate (0.293 g) (Aldrich, rhodium(III) nitrate solution ~10 % (wt/wt) Rh in > 5 wt. % nitric acid) was added to 10 cm^3 of distilled, deionized (DDI) H_2O and added to a solution of 1,10 phenanthroline (0.358 g) (Sigma-Aldrich Corporation) in 15 cm^3 ethanol (Sigma-Aldrich Corporation) to make a 1:2 molar ratio of Rh/phenanthroline (stirring for 20 min at 353 K). This mixture was subsequently added dropwise to a 0.1 M NaOH slurry with Carbon Black Pearls 2000 (Cabot Corporation) at 353 K (stirring for 2 h). A washing of the slurry with 3000 cm^3 of DDI H_2O via vacuum filtration was then done before drying overnight at 343 K. A small portion of the carbon black with Rh/phenanthroline complex (0.1 g) was then impregnated with 80 wt % dicyandiamide (Aldrich) relative to the complex. This slurry was stirred vigorously at 343 K until all the solution evaporated and the solid was dried overnight at the same temperature. This batch was then combined with another batch to reach (0.2 g) before ramping in ultrahigh purity (UHP) N_2 (100 cm^3 min^{-1}) (99.999 %, Praxair) at 10 K min^{-1} and holding at 973 K for a high temperature thermal treatment. The thermally treated Rh sample was then treated in a solution of 11 M HCl and 1 wt % H_2O_2 for 3 h at 333 K in an attempt to remove any Rh metal nanoparticles formed during pyrolysis. Approximately 0.2 g (two combined batches of acid-washed samples) were heated at 10 K min^{-1} to 673 and held for 2 h in flowing UHP H_2 (100 cm^3 min^{-1}) (5 % H_2/Ar) to produce the as synthesized Rh-N-C catalyst. The 0.29 wt % Rh/SiO_2 catalyst was synthesized using incipient wetness impregnation. An aqueous

solution of Rh nitrate (Aldrich, rhodium(III) nitrate solution ~10 % (wt/wt) Rh in > 5 wt. % nitric acid)) (0.053g) was added to 2.5 cm^3 of DDI H_2O and added dropwise to silica gel (2 g) (Davisil 636 Silica Gel).[26, 27] The catalyst was then dried overnight at room temperature before heating in air for 2 h at 393 K. The catalyst was then heated at 10 K min^{-1} to 673 K and thermally treated for 2 h in flowing air (Medical Grade, Praxair). A commercial 5 wt % Rh/C catalyst (Aldrich) was used from the bottle with no further treatment prior to going into the reactor.

3.2.3 Characterization of the Catalysts

High-angle annular dark-field scanning transmission electron microscopy (STEM) imaging was performed using an aberration-corrected STEM Themis, operating at 200 kV and using a convergence semi-angle of 25 mrad.

All inductively coupled plasma optical emission spectroscopy (ICP-OES) analyses were conducted at Galbraith Laboratories Inc. (2323 Sycamore Drive, Knoxville, TN 37921) using a PerkinElmer Optima 5300V, 8300DV, or Avio 500 ICP-OES.

A Micromeritics ASAP 2020 adsorption system was used for H_2 chemisorption. The Rh/SiO_2 catalyst was evacuated for 2 h at 673 K following reduction at that temperature for 2 h in flowing H_2 (99.999 %, Praxair UHP). After reduction, the system was cooled under vacuum to 308 K for analysis. Available metal sites were determined by extrapolating the high pressure, linear portion of the isotherm to zero pressure. A prior study of the highly dispersed Rh metal particles has shown that the stoichiometric ratio of H to surface Rh atoms can be as high as 2:1.[28]

3.2.4 Oxidation of CO

The oxidation of CO was carried out in a stainless steel, down-flow, continuous packed bed reactor. Silicon carbide (2 g) (Universal Photonics, Inc., 150 mesh) was used to dilute the catalyst in each reaction. The reaction conditions involved 160 cm^3 min^{-1} total gas flow with 1 % CO (Praxair, 99.99 %), 2 % O_2 (Praxair 99.99 % O_2) and balance He (Praxair UHP, 99.999%) at 3 atm total pressure. The He was passed through an OMI-2 indicating purifier while CO and O_2 were passed through silica traps immersed in a dry-ice acetone bath to remove trace water and trace carbonyls (from CO). Before initiating the reaction, the catalyst was thermally treated in situ in flowing He by ramping at 10 K min^{-1} to 673 K and holding for 2 h before cooling to the reaction temperature. A Balzers Quadrupole Mass Spectrometer was used to analyze the reactor effluent with signals associated with masses (m/e) 28, 29, 44, and 45 amu recorded at a voltage of 1200 V and dwell times of 50 ms for all masses except 44 and 45 which were measured at 100 ms. A cooling bath for reactions at 199 K was made by adding dry-ice to acetone.

3.3 Results

3.3.1 Density Functional Theory Screening of Metal Ions for Low Temperature CO Oxidation Activity

We used DFT calculations with vdW-DF (full calculation details are provided in the Methods Section 3.2) to investigate the viability of O_2 activation through a CO-assisted mechanism on a variety of isolated transition metal ions in N-doped carbon. Briefly, a previous mechanism for Co-N-C involved CO binding to the metal and interacting with O_2 to form a CO-O_2 complex, which evolves into 2 CO_2 molecules with subsequent reactions.[11] Limited charge transfer to Co

occurred throughout the cycle, indicating other metal ions may also be viable active centers. This low-temperature mechanism requires: 1) an exothermic enough CO binding energy to the metal to result in non-negligible CO coverage 2) a CO binding energy that is at least competitive with the O_2 binding energy (to the metal) to prevent O_2 poisoning, and 3) the ability to form a stable CO-O_2 complex. Consequently, for screening purposes we used a CO binding energy < -30 kJ mol^{-1}, CO and O_2 binding energies that are within 30 kJ mol^{-1} of each other, and a convergence to a local minimum CO-O_2 complex (additional details for how we arrived at these numbers can be found in Appendix Figs. B4 and B5). We screened 15 candidate metal ions in four-fold coordinated pyridinic N sites with a double vacancy since this motif is reported for many synthesized catalysts[11, 15, 16, 29-32] and has been shown computationally to stabilize the metal.[16, 33, 34] The transition metals for screening were chosen based on their proximity to Co in the periodic table or similar electronegativity in the case of Ga[35] and experimental evidence that they can be synthesized in the double vacancy motif (Ag and Mo were neglected since both were found to be unstable in the double vacancy motif).[15, 16]

Figures 3.1 and 3.2 show the vdW-DF computed CO and O_2 binding energies for various metal ions coordinated to four N atoms (M-N-C) catalysts. Candidate metals in groups 10-13 bind CO weakly, apart from Cd, and are unlikely to have non-negligible CO coverage. Weak binding to Ni-N-C is consistent with the observed lack of CO uptake on Ni-N-C, even at cryo-temperatures.[13, 14] Conversely, transition metal ions in groups 6-9 have reasonably exothermic CO binding energy values in a wide range (-226 to -50 kJ mol^{-1}) and therefore require application of the other criterion to differentiate. The Cr, Mn, and Cd N-C cases bound O_2 stronger than CO by at least 56 kJ mol^{-1}, which indicates that O_2 would poison these sites for a low temperature path initiated with CO bound to the transition metal. The preference for binding O_2 over CO does not

preclude low temperature CO oxidation, but only higher energy mechanisms for O_2 starting on the transition metal atom have been reported.[16] Previous reports from Mavrikakis and co-workers have found a higher barrier mechanism using quantum chemical calculations where O_2 dissociates on the transition metal and undergoes an Eley-Rideal type mechanism that has barriers in the range of 66 kJ mol^{-1}, which is not consistent with low temperature activity.[16] Thus, in the search for metals that follow a low-temperature mechanism similar to Co, application of the first two criteria narrow the search to metals in groups 8 and 9.

Optimization of structures, starting from our previously reported CO-O_2 complex that forms on Co, were used to differentiate groups 8 and 9 further. For the transition metals in group 8, the optimization of a structure starting with CO bound to the metal atom in a bent configuration and O_2 coordinated to the CO (e.g. Fig. 3.3 structure 3) resulted in the CO relaxing to a linear orientation with a large distance (3.5 Å) between the carbon atom in CO and either of the oxygen atoms in the O_2 molecule (see Supplemental Files submitted with this dissertation). The inability of Fe-N-C to form this complex, and our assumption that this precludes participation in low-temperature CO-oxidation, is consistent with prior experimental results where an Fe-N-C catalyst was reported to be catalytically inactive for low temperature (200 K) CO oxidation.[12] The application of these criteria therefore leaves only the transition metal atoms in group 9 which can form stable CO-O_2 complexes with reasonable bond distances between the carbon atom in CO and an oxygen atom in the O_2 (1.5 Å). Group 9 includes Co, which we used to establish the selection criteria, but also Ir-N-C and Rh-N-C.[11] Rhodium-N-C catalysts have previously been experimentally synthesized[25, 36] so the Rh-N-C catalyst was chosen instead of Ir-N-C for subsequent calculations of the reaction coordinate and comparison with experimental data.

Group 6		Group 7		Group 8		Group 9		Group 10		Group 11		Group 12		Group 13	
Cr		**Mn**		**Fe**		**Co**		**Ni**		**Cu**		**Zn**		**Ga**	
CO	-87	CO	-92	CO	-128	CO	-65	CO	-15	CO	-15	CO	-19	CO	-30
O_2	-212	O_2	-148	O_2	-104	O_2	-85	O_2	-27	O_2	-31	O_2	-66	O_2	-161
				Ru		**Rh**		**Pd**				**Cd**			
				CO	-226	CO	-54	CO	-14			CO	-157		
Adsorption Energy				O_2	-175	O_2	-60	O_2	-26			O_2	-222		
is in kJ mol^{-1}						**Ir**		**Pt**		**Au**					
						CO	-79	CO	-14	CO	-13				
						O_2	-48	O_2	-26	O_2	-43				

Figure 3.1. Adsorption energies of CO and O_2 computed with vdW-DF. All metal ions were bound to four pyridinic N atoms.
For O_2 binding, the more exothermic optimized binding motif (bidentate or monodentate O_2) was reported. All structure files can be viewed as a Supplemental Attachment and magnetic moments are reported in Appendix Fig. B6.

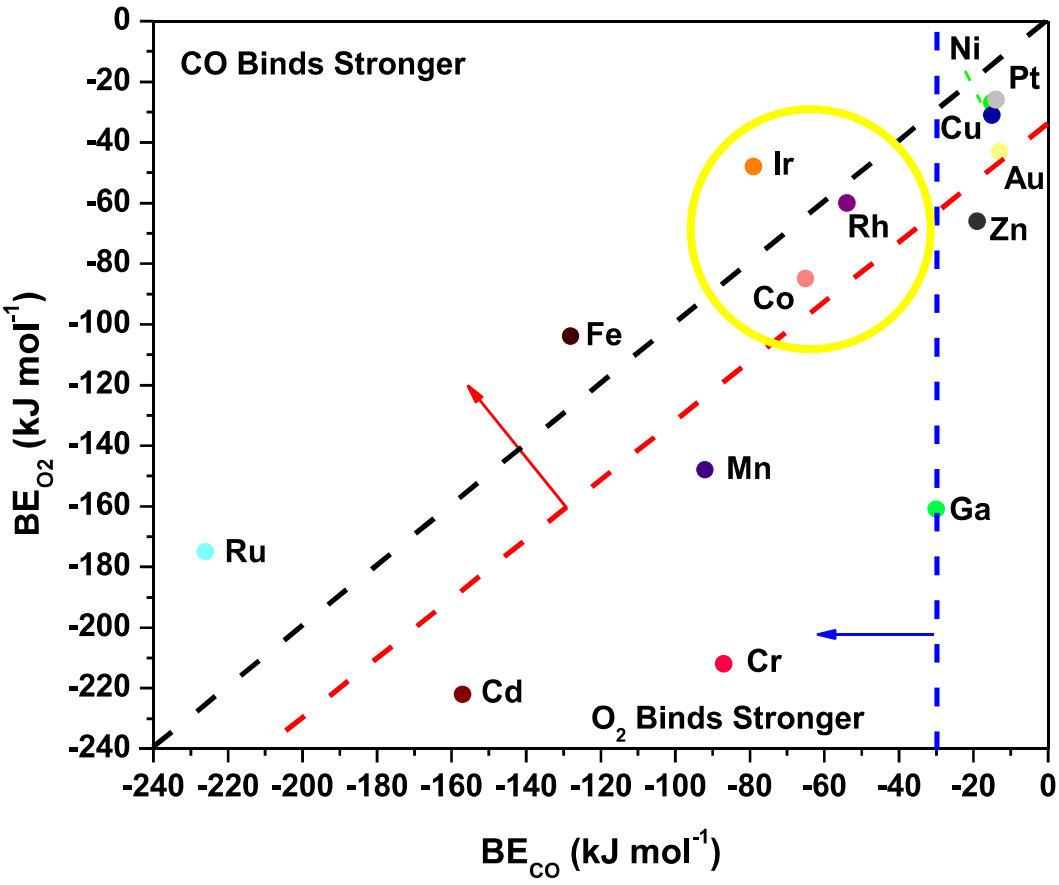

Figure 3.2. Adsorption energies of CO and O_2 computed with vdW-DF.
The black line bisecting the figure is a representation of equal binding energies for CO and O_2 on the metal. The vertical blue line indicates the -30 kJ mol^{-1} binding energy needed for CO to adsorb on the metal atom (criteria 1). The diagonal red line indicates the -30 kJ mol^{-1} excess O_2 binding energy relative to CO (criteria 2). The yellow circle indicates the metals that fit all of criteria 1-3.

The Rh-N-C catalyst provides an opportunity for both experimental validation and an exploration of potential intermediates in a catalytic cycle using structures from the previously described Co-N-C mechanism.[11] The first step in the catalytic cycle involves adsorption and as discussed earlier, calculations for CO and O_2 revealed they had similar binding energies on the Rh so either structure could be the starting structure for the catalytic cycle. Although Rh is known to form Rh gem-dicarbonyl structures,[37] optimization of Rh gem-dicarbonyl structures resulted in the desorption of one molecule of CO, leaving only one CO bound to the metal. The next step involves

interaction of both CO and O_2 and the mechanism could start with either CO or O_2 initially adsorbed but calculations with O_2 bound to the metal ion and CO in the gas phase did not result in a CO-O_2 complex forming. The inability to form the CO-O_2 complex suggests that CO binding to the Rh metal is the first step in the catalytic cycle and is denoted in the potential energy diagram in Fig. 3.3 as (step 2). The CO molecule then interacts with a gas phase O_2 molecule to form a CO-O_2 complex on the Rh (step 3). The complex then goes through a transition state where the bound O_2 molecule interacts with the carbon support (step TS1) before dissociating and forming O* on the carbon support and producing a gas phase CO_2 molecule (step 4). The reaction sequence is then closed by the binding of a new CO molecule to Rh (5) before interacting with the O* on the carbon surface through a negligible barrier of ~ 0 kJ mol^{-1} (TS2) to form a gas phase CO_2 molecule. Thus, the only significant barrier during the overall reaction sequence is the 20 kJ mol^{-1} activation energy (TS1). The barriers associated with this mechanism are similar to those of our previously calculated barriers for CO oxidation on a Co-N-C catalyst, with its most significant barrier being 16 kJ mol^{-1}.[11] The mechanism for Co-N-C did not involve a redox cycle on the Co and thus redox on the Rh atom was further explored.[11]

The oxidation state of Rh was investigated with Bader charge analysis (Fig. 3.3 and Appendix Fig. B7) by first calibrating the charge with references (1+ and 3+).[38, 39] The oxidation state for Rh in the bare structure was 1.4+. An oxidation state of 1.4+ is less than the 2+ reported for Rh in similar N-doped Rh complexes but is within the metallic to 3+ range typically reported for Rh.[40, 41] The binding of CO and the formation of the CO-O_2 transition state (TS1) resulted in the largest change in oxidation state (2.4+). This change in oxidation state is consistent with electron sharing with the adsorbate or the movement of Rh from the plane. It is possible that a nonclassical carbonyl formed on the Rh atom. The electrostatic Rh-CO interaction is potentially

stronger and has a smaller π back-bonding than the Co case and thus the C-O bond is contracted as negative charge gets placed onto the C atom in the CO molecule.[42, 43] These results contrast with the Co-N-C mechanism which did not involve significant electron sharing. Evidently, although only very limited charge transfer occurred for Co, the Rh mechanism seems to follow a similar path with increased charge transfer.[11]

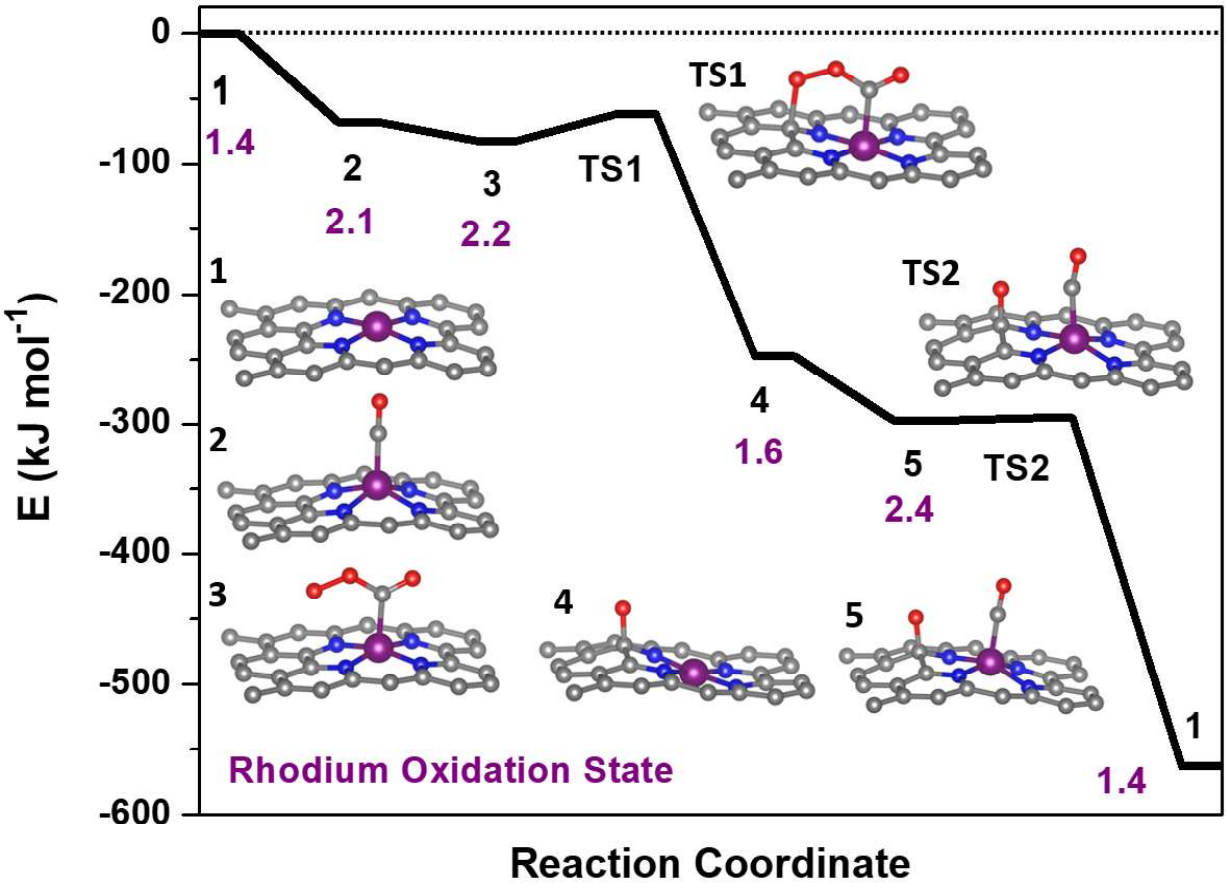

Figure 3.3. Reaction coordinate for the low-temperature CO oxidation mechanism over Rh-N-C computed with vdW-DF.
Molecular structures corresponding to the reaction coordinates are included. Rhodium oxidation state changes were calculated using a normalized Bader charge analysis as reported in Appendix Fig. B7.

3.3.2 Catalyst Synthesis and Characterization

The quantum chemical calculations suggest that Rh-N-C sites may utilize a mechanism that involves weak binding of reactants and a low transition state barrier for low temperature CO oxidation. To investigate isolated Rh in N-doped carbon for low temperature CO oxidation, a 1.26 wt % Rh-N-C catalyst was synthesized via a modified high-temperature pyrolysis method similar to previous Co[8, 11] and Rh-N-C[25] catalysts. To confirm the presence of isolated Rh ions on Rh-N-C, we examined the Rh-N-C by atomic-resolution HAADF-STEM, as shown in Fig. 3.4. Although atomically dispersed Rh ions are apparent and are likely stable since they are present after treatments in acid-peroxide solution and high-temperature H_2, some nanoparticles were still observed. The similar content of Rh before and after treatment (1.23 versus 1.26 wt %) indicates that a significant amount of Rh single atoms are not removed and thus can be investigated for low temperature CO oxidation.

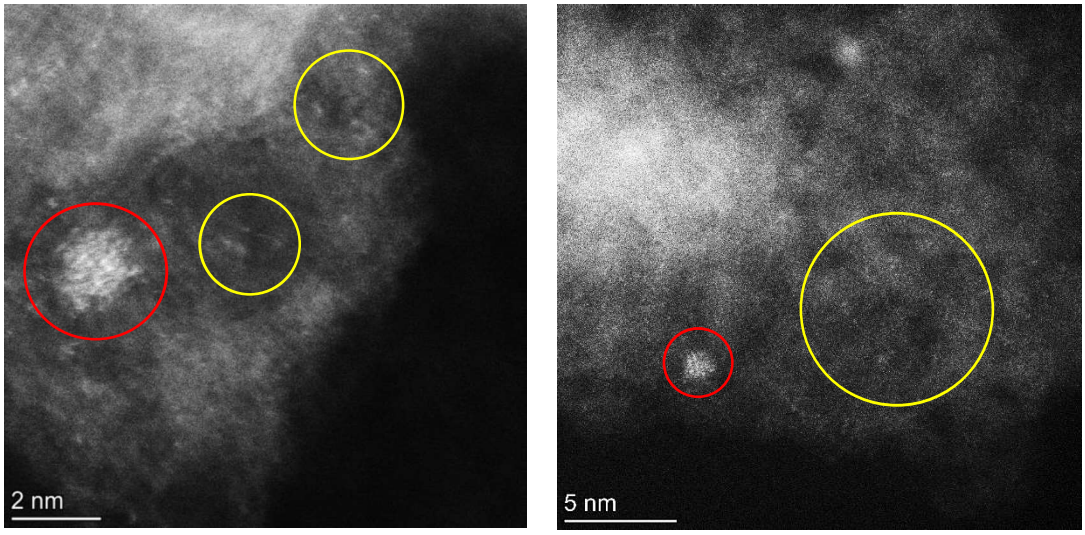

Figure 3.4. Atomic-resolution HAADF-STEM images of Rh-N-C show isolated Rh atoms and small Rh nanoparticles.
The left panel shows a small area where the isolated atoms of Rh are visible and the right panel shows an expanded view with few nanoparticles of Rh present. Some isolated Rh atoms in the image are circled in yellow. Rhodium nanoparticles are circled in red.

3.3.3 Oxidation of CO over Rh Catalysts

The steady-state activity of 1.26 wt % Rh-N-C for CO oxidation was compared to those measured over a nitrogen-free commercially available 4.63 wt % Rh/C and a highly dispersed 0.29 wt % Rh/SiO_2 catalyst. All of these catalysts were evaluated over a range of temperatures (199 to 460 K) at a total pressure of 3 atm. Temperatures were alternated between high and low to ensure that any potential hysteresis could be explored. Figure 3.5 shows the catalytic activity of Rh-N-C at temperatures < 418 K, with activity being observed as low as 199 K. The high activity for the Rh-N-C contrasts with the other Rh catalysts which contain metal particles that are known to be covered in CO, blocking the O_2 adsorption needed for turnover, at the lower temperatures used here. Indeed, the other Rh containing catalysts exhibited no detectable activity at low temperatures (273 K and lower). As the N-C support exhibited negligible conversion at the temperatures studied, it is likely the activity is coming from the isolated Rh.[11] Interestingly, a Rh/TiO_2 catalyst was previously reported to have low temperature CO oxidation activity and its performance was attributed to the formation of a $CO\text{-}O_2$ complex similar to the one proposed in this study.[44] In that work, a CO bound on Rh was used to activate O_2 with the reducible TiO_2 support. Although our Rh-N-C catalyst does not have a reducible support, its low temperature CO oxidation activity is consistent with the CO-assisted activation of O_2 as described earlier. In the higher temperature regime (> 418 K), the activity begins to increase with temperature. The presence of nanoparticles, as confirmed by STEM, could account for the observed high temperature activity of Rh-N-C. Fortunately, reaction kinetics can be used to discriminate between the participation of metal nanoparticles versus isolated Rh cations in the CO oxidation reaction.

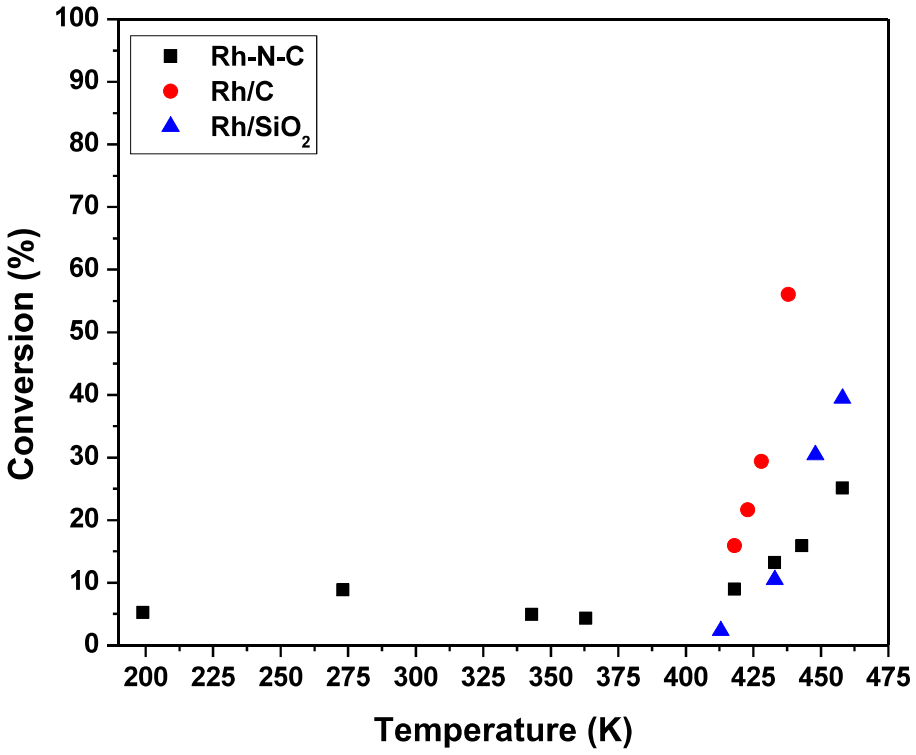

Figure 3.5. Influence of temperature on the steady-state CO conversion over Rh catalysts. The reactions were run with 0.1 g of catalyst diluted in SiC with 160 cm^3 min^{-1} total flow, 1 % CO, 2 % O_2 and balance He at 3 atm.

The observed steady-state orders of reaction during CO oxidation catalyzed by Rh-N-C as shown in Table 3.1 were strikingly different at low temperature (273 K) compared to high temperature (498 K). The positive order dependence of the rate on CO for the low temperature CO oxidation over Rh-N-C contrasts with the inhibition by CO observed over Rh/C and Rh/SiO_2 in this study (Table 3.1) and other reported platinum-group metal catalysts.[45, 46] The positive CO reaction order is consistent with the weak adsorption of CO on the active site, as suggested by DFT. The calculated binding energy of CO on Rh-N-C is significantly weaker than on Rh metal (-120 kJ mol^{-1}), which has a negative CO order under similar concentrations of CO and O_2.[47] As CO oxidation does not occur to any measurable extent on Rh nanoparticles at low temperature, the reactivity results are attributed solely to the isolated Rh ions in Rh-N-C and the neighboring Rh

nanoparticles are merely spectators on the Rh-N-C. While the reaction order for CO in the high temperature regime (> 418 K) is different than that at low temperature, the nearly zero order dependence in CO is consistent with high temperature catalytic activity being a convolution of the reaction occurring on the nanoparticles (observed using STEM) and on the isolated Rh ions. Evidently, inhibition by CO on isolated Rh nanoparticles and positive order in CO on isolated Rh combine to a nearly zero-order dependence at the temperature used here. A previous study on catalysts with various ratios of both nanoparticles and isolated atoms (Ir-$MgAl_2O_4$) reported changes in the reaction order with reaction conditions being used to probe isolated atoms versus nanoparticles.[48] By raising the partial pressure of CO, which inhibited reaction on nanoparticles, the kinetics of the isolated atoms could be studied.[48] In our case, the higher partial pressures of CO did not result in a low enough contribution of the inhibited nanoparticles. The reaction order in O_2 is positive on both nanoparticles and isolated Rh at both low and high temperatures, so it cannot be used to discriminate between the different types of sites.

Table 3.1 shows the apparent activation energies for CO oxidation over the Rh containing catalysts. The rate being invariant with temperature in the low temperature regime for Rh-N-C (< 413 K) is consistent with a negligible apparent activation energy (~0 kJ mol^{-1}). The low temperature regime contrasted with the high temperature regime (413 – 460 K) wherein the rate increased significantly with temperature. Similar to the reported orders of reaction in this high temperature regime, the apparent activation energy is likely a convolution of rate occurring on both the isolated Rh atoms and the Rh nanoparticles. The apparent activation energies measured in the high temperature regime (413 – 460 K) for the other Rh containing catalysts, Rh/C and Rh/SiO_2, are consistent with CO oxidation on Rh nanoparticles.[45] Thus, the reaction orders and apparent activation energy for the Rh-N-C at high temperatures are not consistent with the CO-

assisted O_2 activation mechanism depicted in Fig. 3.3, whereas the low temperature CO oxidation kinetics over Rh-N-C are completely consistent with that mechanism.

Table 3.1. Summary of Kinetic Parameters for CO and O_2 on Various Rh-Containing Catalysts for CO Oxidation

catalyst	$E_{apparent}$[a] (kJ mol^{-1})	orders of reaction[b]	
		CO	O_2
Rh-N-C			
low-T regime < 403 K	0	0.6	0.6
high-T regime > 403 K	40	0	1.1
Rh/C	98	-1.0	1.5[c]
Rh/SiO_2	110	-1.0	1.5[c]

[a]Apparent activation energies were determined from Arrhenius-type plots (Appendix Fig. B8). [b]Kinetic orders were evaluated under steady-state differential conversion (< 40 %) and were determined by varying the partial pressure of one while holding the other constant (Appendix Fig. B9 a, b). [c]Kinetic orders for O_2 on Rh/C and Rh/SiO_2 were calculated at a constant 3 % CO instead of the 1 % CO reaction condition to stay in the differential conversion regime.

3.4 Discussion

To understand if the mechanism and elementary steps reasonably approximate the experimental kinetics, a rate expression for the reaction path was derived. The reaction path involves the weak adsorption of reactants on the surface, which is consistent with the observed reaction kinetics (observed reaction orders and the approximately zero apparent activation energy). The deviations from first-order dependence suggests that there is some non-saturated coverage of CO or competition between the CO and O_2, which is apparent with the similar computationally calculated binding energies for the small cell (-68 and -68 kJ mol^{-1} for CO and O_2 respectively).

The overall rate of reaction should be proportional to the reaction step involving dioxygen activation (TS1 in Fig. 3.3), (CI-NEB presented in Appendix Fig. B2 a) as the sequential oxidation

of CO with the second oxygen atom from Fig. 3.3 is nearly barrierless (CI-NEB (TS2) in Appendix Fig. B2 b). Thus, we can write the expression for the observed rate as

$$rate = k[CO - O_2]_{ads} \quad (1)$$

where $[CO\text{-}O_2]_{ads}$ represents the surface concentration of the complex that is formed by the first adsorption of CO on Rh followed by the adsorption of O_2 next to CO to give structure 3 in Fig. 3.3. The rate is therefore proportional to the fractional coverage of O_2 on the adsorbed CO, exemplified by the following equation

$$rate = k\theta_{CO}\gamma_{O_2} \quad (2)$$

A standard Langmuir isotherm for competitive adsorption can be used to represent the fractional coverage of CO on Rh sites (θ_{CO})

$$\theta_{CO} = \frac{K_{CO}[CO]}{(1+K_{CO}[CO]+K_{O_2}[O_2])} \quad (3)$$

where the K_{CO} and K_{O_2} represent adsorption equilibrium constants of CO and O_2, respectively, on the bare Rh ions. It should be noted that the γ_{O2} term in equation 2 is not related to the adsorption equilibrium constant of O_2 on Rh. This term is associated with the weak adsorption of O_2 adjacent to the adsorbed CO. Thus, γ_{O2} is approximated by the linear, low coverage, portion of an adsorption isotherm (structure 3 in Fig. 3.3) denoted by $K'_{O_2}[O_2]$. To compare with the proposed rate expression with experiment, the Langmuir isotherm can be approximated as a power law expression to give an observed rate expression as:

$$rate \propto \frac{kK_{CO}[CO]K'_{O_2}[O_2]}{(K_{CO}[CO])^{\alpha}(K_{O_2}[O_2])^{\beta}} \quad (4)$$

Values of α and β can be adjusted to account for the experimentally determined orders of reaction to give the following expression in (5), which can be used to explore the temperature dependence of the rate.

$$rate \propto kK_{CO}^{0.6}[CO]^{0.6}K'_{O_2}K_{O_2}^{-0.4}[O_2]^{0.6} \quad (5)$$

The DFT derived values for heats of adsorption of CO or O_2 adsorbed on Rh (-68 kJ mol^{-1}), the O_2 adsorbed adjacent to the CO (-14 kJ mol^{-1}), and the E_a associated with TS1 (20 kJ mol^{-1}) are substituted into (5) to give an apparent activation energy ($E_{apparent}$) as calculated in (6)

$$E_{apparent} = E_a + 0.6\Delta H_{CO} + 0.6\Delta H_{CO-O_2} - 0.4\Delta H_{O_2} = -1\ kJ\ mol^{-1} \quad (6)$$

The estimated $E_{apparent}$ = -1 kJ mol^{-1} is in reasonable agreement with the experimental value of approximately zero and is consistent with the mechanism for low-temperature CO oxidation proposed by our DFT calculations.

The proposed low-temperature mechanism of CO oxidation on Rh-N-C does not preclude other potential mechanisms for low or high temperature CO oxidation occurring on the isolated Rh sites. For example, other screened metals had various binding energies of CO and O_2 to the metal ion. Metal ions that bound CO stronger than the binding energy of CO to Co or Rh were unable to form the O-O-C-O transition state. Transition metals such as Fe have been previously investigated with O_2 binding first to give a higher barrier transition state but apparently would not be suitable for low temperature CO oxidation.[16] This indicated that while there could be other barriers for O_2 activation, the one studied here seems amenable to this particular column of the periodic table as it is completely consistent with at least two metals.

A simplified kinetic analysis was applied to the low-temperature regime but the model accounts for the change in binding energy and potential competition of CO and O_2 on the surface

of the Rh ion. The model does still account for the positive order behavior of both CO and O_2 along with the nearly zero apparent activation energy. This similarity implies that there is a small barrier for O_2 activation, and the rate is instead dominated by the number of adsorbed intermediates leading to product and the competition of CO and O_2 for the same surface sites. This contrasts with the literature on platinum group metals and supported Rh nanoparticles where CO inhibits adsorption of O_2 to adjacent surface vacancies and thus prevents dissociative O_2 chemisorption, leading to a negative order for CO.[46, 49] Conversely, in the previously described Co-N-C case, there was a negative apparent activation energy, which contrasts with the nearly zero activation energy in this study. The difference appears to be due to the more exothermic binding energy of the CO and O_2 (-68 and -68 kJ mol^{-1}, respectively) for Rh, versus the CO and O_2 binding energies on Co (-57 and -73 kJ mol^{-1}, respectively). The more exothermic binding energies indicate that the Rh case will have a lower reaction order.[11]

Interestingly, similar transition states have previously been attributed to low temperature CO oxidation on Rh and Ir. For example, Rh/TiO_2 was found to have a low barrier with the reducible support enabling the formation of O-O-C=O and activation through vacancies in the TiO_2.[44] The similarity to other Rh systems indicates that other isolated Rh ions may be able to active O_2 in a similar mechanism. Indeed, another transition metal in the Co column, Ir, was previously investigated as an isolated Ir-on-$MgAl_2O_4$ catalyst.[50] The proposed mechanism for CO oxidation involved a spectator CO molecule which enables an Eley-Rideal-type mechanism with surface oxygen.[50] Isolated atoms appear to enable interesting interactions with surface groups surrounding the transition metal site.

After screening metals for reaction paths similar to the previously derived CO-assisted mechanism, it appears that the column containing the Co, Rh, and Ir on the periodic table has

characteristics that enable low temperature CO oxidation through a CO-assisted mechanism. Other metals may be active for low temperature O_2 activation but for those transition metals it appears that O_2 is activated through different mechanisms as they either lacked CO uptake or were unable to form stable CO-O_2 complexes.

3.5 Conclusions

Our results suggest that the other transition metal ions in N-C in the Co column have characteristics of preferential binding of CO, non-negligible coverages CO on the transition metal ion, and the ability to form a CO-O_2 complex similar to our previous report on Co-N-C (Chapter 2). Detailed quantum chemical calculations on the Rh-N-C catalyst suggest that Rh-N-C catalyst could proceed through a low temperature mechanism involving CO-assisted O_2 activation with the carbon support. Gas-phase CO oxidation over a synthesized isolated Rh-N-C catalyst showed low temperature activity and reaction orders that are consistent with the quantum chemical calculations. Application of the kinetic parameters with the DFT derived adsorption and barrier values resulted in a predictive rate expression. The results suggest that O_2 could be activated through a CO assisted method on the transition metal atoms in group 9.

3.6 References

1. Liang, H. W.; Wei, W.; Wu, Z. S.; Feng, X.; Müllen, K., Mesoporous Metal-Nitrogen-Doped Carbon Electrocatalysts for Highly Efficient Oxygen Reduction Reaction. *J. Am. Chem. Soc.* **2013,** *135*, 16002-16005.

2. Liu, Q.; Zhang, J., Graphene Supported Co-g-C_3N_4 as a Novel Metal-Macrocyclic Electrocatalyst for the Oxygen Reduction Reaction in Fuel Cells. *Langmuir* **2013,** *29*, 3821-3828.

3. Malko, D.; Kucernak, A.; Lopes, T., In Situ Electrochemical Quantification of Active Sites in Fe-N/C Non-Precious Metal Catalysts. *Nat. Commun.* **2016,** *7*, 1-7.

4. Zitolo, A.; Ranjbar-Sahraie, N.; Mineva, T.; Li, J.; Jia, Q.; Stamatin, S.; Harrington, G. F.; Lyth, S. M.; Krtil, P.; Mukerjee, S.; Fonda, E.; Jaouen, F., Identification of Catalytic Sites in Cobalt-Nitrogen-Carbon Materials for the Oxygen Reduction Reaction. *Nat. Commun.* **2017,** *8*, 957.

5. Zhang, Q.; Mamtani, K.; Jain, D.; Ozkan, U.; Asthagiri, A., CO Poisoning Effects on FeNC and CN_x ORR Catalysts: A Combined Experimental–Computational Study. *J. Phys. Chem. C* **2016,** *120*, 15173-15184.

6. Vijay, S.; Ju, W.; Brückner, S.; Tsang, S. C.; Strasser, P.; Chan, K., Unified Mechanistic Understanding of CO_2 Reduction to CO on Transition Metal and Single Atom Catalysts. *Nat. Catal.* **2021,** *4*, 1024-1031.

7. Xie, J.; Yin, K.; Serov, A.; Artyushkova, K.; Pham, H. N.; Sang, X.; Unocic, R. R.; Atanassov, P.; Datye, A. K.; Davis, R. J., Selective Aerobic Oxidation of Alcohols over Atomically-Dispersed Non-Precious Metal Catalysts. *ChemSusChem*, **2017**, (10), 359-362.

8. Xie, J.; Kammert, J. D.; Kaylor, N.; Zheng, J. W.; Choi, E.; Pham, H. N.; Sang, X.; Stavitski, E.; Attenkofer, K.; Unocic, R. R.; Datye, A. K.; Davis, R. J., Atomically Dispersed Co

and Cu on N-Doped Carbon for Reactions Involving C–H Activation. *ACS Catal.* **2018**, (8), 3875-3884.

9. Huang, K.; Fu, H.; Shi, W.; Wang, H.; Cao, Y.; Yang, G.; Peng, F.; Wang, Q.; Liu, Z.; Zhang, B.; Yu, H., Competitive Adsorption on Single-Atom Catalysts: Mechanistic Insights into the Aerobic Oxidation of Alcohols over Co–N–C. *J. Catal.* **2019,** *377*, 283-292.

10. Li, J.; Liu, J.; Zhang, J.; Wan, T.; Huang, L.; Wang, X.; Pan, R.; An, Z.; Vlachos, D. G., An Unconventional DCO_x Favored Co/N-C Catalyst for Efficient Conversion of Fatty Acids and Esters to Liquid Alkanes. *Appl. Catal. A: General* **2020,** *591*.

11. Whitcomb, C. A.; Sviripa, A.; Schapowal, M. I.; Mamedov, K.; Unocic, R. R.; Paolucci, C.; Davis, R. J., Mechanistic Insights on the Low-Temperature Oxidation of CO Catalyzed by Isolated Co Ions in N-Doped Carbon. *ACS Catal.* **2022,** *12* (24), 15529-15540.

12. Wang, J.; You, R.; Zhao, C.; Zhang, W.; Liu, W.; Fu, X. P.; Li, Y.; Zhou, F.; Zheng, X.; Xu, Q.; Yao, T.; Jia, C. J.; Wang, Y. G.; Huang, W.; Wu, Y., N-Coordinated Dual-Metal Single-Site Catalyst for Low-Temperature CO Oxidation. *ACS Catal.* **2020,** *10*, 2754-2761.

13. Luo, F.; Choi, C. H.; Primbs, M. J. M.; Ju, W.; Li, S.; Leonard, N. D.; Thomas, A.; Jaouen, F.; Strasser, P., Accurate Evaluation of Active-Site Density (SD) and Turnover Frequency (TOF) of PGM-Free Metal–Nitrogen-Doped Carbon (MNC) Electrocatalysts using CO Cryo Adsorption. *ACS Catal.* **2019,** *9*, 4841-4852.

14. Luo, F.; Wagner, S.; Onishi, I.; Selve, S.; Li, S.; Ju, W.; Wang, H.; Steinberg, J.; Thomas, A.; Kramm, U. I.; Strasser, P., Surface Site Density and Utilization of Platinum Group Metal (PGM)-Free Fe-NC and FeNi-NC Electrocatalysts for the Oxygen Reduction Reaction. *Chem. Sci.* **2021,** *12*, 384-396.

15. Kaiser, S. K.; Chen, Z.; Faust Akl, D.; Mitchell, S.; Pérez-Ramírez, J., Single-Atom Catalysts across the Periodic Table. *Chem. Rev.* **2020,** *120*, 11703-11809.

16. Kropp, T.; Mavrikakis, M., Transition Metal Atoms Embedded in Graphene: How Nitrogen Doping Increases CO Oxidation Activity. *ACS Catal.* **2019,** *9*, 6864-6868.

17. Kresse, G.; Furthmuller, J., Efficient Iterative Schemes for Ab Initio Total-Energy Calculations using a Plane-Wave Basis Set. *Phys. Rev. B* **1996,** *54* (16), 11169-11186.

18. Perdew, J. P.; Burke, K.; Ernzerhof, M., Generalized Gradient Approximation Made Simple. *Phys. Rev. Lett.* **1996,** *77*, 3865-3868.

19. Zhang, P.; Chen, X. F.; Lian, J. S.; Jiang, Q., Structural Selectivity of CO Oxidation on Fe/N/C Catalysts. *J. Phys. Chem. C* **2012**, *116* (33), 17572-17579.

20. Wang, Q.; Jin, B.; Hu, M.; Jia, C.; Li, X.; Sharman, E.; Jiang, J., N-Doped Graphene-Supported Diatomic Ni−Fe Catalyst for Synergistic Oxidation of CO. *J. Phys. Chem. C* **2021**, *125* (10), 5616-5622.

21. He, B. L.; Shen, J. S.; Tian, Z. X., Iron-Embedded C_2N Monolayer: A Promising Low-Cost and High-Activity Single-Atom Catalyst for CO Oxidation *Phys. Chem. Chem. Phys*. **2016**, 24261-24269.

22. Dion, M.; Rydberg, H.; Schroder, E.; Langreth, D. C.; Lundqvist, B. I., van der Waals Density Functional for General Geometries. *Phys. Rev. Lett.* **2004,** *92* (24), 246401.

23. Henkelman, G.; Uberuaga, B. P.; Josson, H., A Climbing Image Nudged Elastic Band Method for Finding Saddle Points and Minimum Energy Paths and Minimum Energy Paths. *J. Chem. Phys.* **2000,** *113*.

24. Henkelman, G.; Josson, H., Improved Tangent Estimate in the Nudged Elastic Band Method for Finding Minimum Energy Paths and Saddle Points. *J. Chem. Phys.* **2000,** *133*.

25. Luo, Z.; Whitcomb, C. A.; Kaylor, N.; Zhang, Y.; Zhang, S.; Davis, R. J.; Gunnoe, T. B., Oxidative Alkenylation of Arenes Using Supported Rh Materials: Evidence that Active Catalysts are Formed by Rh Leaching. *ChemCatChem* **2021,** *13*, 260-270.

26. Kaylor, N.; Xie, J.; Kim, Y. S.; Pham, H. N.; Datye, A. K.; Lee, Y. K.; Davis, R. J., Vapor Phase Deoxygenation of Heptanoic Acid over Silica-Supported Palladium and Palladium-Tin Catalysts. *J. Catal.* **2016,** *344*, 202-212.

27. Lam, Y. L.; Boudart, M., Preparation of Small Au-Pd Particles on Silica. *J. Catal.* **1977,** *50*, 530-540.

28. Duivenvoorden, F. B. M.; Koningsberger, D. C., Determination of Metal Particle Size of Highly Dispersed Rh , Ir , and Pt Catalysts by Hydrogen Chemisorption and EXAFS. *J. Catal.* **1987,** *38*, 26-38.

29. Zhang, N.; Zhou, T.; Chen, M.; Feng, H.; Yuan, R.; Zhong, C. A.; Yan, W.; Tian, Y.; Wu, X.; Chu, W.; Wu, C.; Xie, Y., High-Purity Pyrrole-Type FeN_4 Sites as a Superior Oxygen Reduction Electrocatalyst. *Energy and Environ. Sci.* **2020,** *13*, 111-118.

30. Haque, E.; Zavabeti, A.; Uddin, N.; Wang, Y.; Rahim, M. A.; Syed, N.; Xu, K.; Jannat, A.; Haque, F.; Zhang, B. Y.; Shoaib, M. A.; Shamsuddin, S.; Nurunnabi, M.; Minett, A. I.; Ou, J. Z.; Harris, A. T., Deciphering the Role of Quaternary N in O_2 Reduction over Controlled N-Doped Carbon Catalysts. *Chem. Mater.* **2020,** *32*, 1384-1392.

31. Ma, R.; Lin, G.; Ju, Q.; Tang, W.; Chen, G.; Chen, Z.; Liu, Q.; Yang, M.; Lu, Y.; Wang, J., Edge-Sited Fe-N_4 Atomic Species Improve Oxygen Reduction Activity via Boosting O_2 Dissociation. *Appl. Catal. B: Environ.* **2020,** *265*, 118593.

32. Liu, J.; Kong, X.; Zheng, L.; Guo, X.; Liu, X.; Shui, J., Rare Earth Single-Atom Catalysts for Nitrogen and Carbon Dioxide Reduction. *ACS Nano* **2020,** *14*, 1093-1101.

33. Fei, H.; Dong, J.; Feng, Y.; Allen, C. S.; Wan, C.; Volosskiy, B.; Li, M.; Zhao, Z.; Wang, Y.; Sun, H.; An, P.; Chen, W.; Guo, Z.; Lee, C.; Chen, D.; Shakir, I.; Liu, M.; Hu, T.; Li, Y.; Kirkland, A. I.; Duan, X.; Huang, Y., General Synthesis and Definitive Structural Identification of MN_4C_4 Single-Atom Catalysts with Tunable Electrocatalytic Activities. *Nat. Catal.* **2018,** *1*, 63-72.

34. Jain, D.; Zhang, Q.; Gustin, V.; Hightower, J.; Gunduz, S.; Co, A. C.; Miller, J. T.; Asthagiri, A.; Ozkan, U. S., Experimental and DFT Investigation into Chloride Poisoning Effects on Nitrogen-Coordinated Iron-Carbon (FeNC) Catalysts for Oxygen Reduction Reaction. *J. Phys. Chem. C* **2020,** *124*, 10324-10335.

35. Boeyens, J. C. A., The Periodic Electronegativity Table. *Zeitschrift für Naturforschung B* **2008,** *63* (2), 199-209.

36. Xiong, Y.; Dong, J.; Huang, Z. Q.; Xin, P.; Chen, W.; Wang, Y.; Li, Z.; Jin, Z.; Xing, W.; Zhuang, Z.; Ye, J.; Wei, X.; Cao, R.; Gu, L.; Sun, S.; Zhuang, L.; Chen, X.; Yang, H.; Chen, C.; Peng, Q.; Chang, C. R.; Wang, D.; Li, Y., Single-Atom Rh/N-Doped Carbon Electrocatalyst for Formic Acid Oxidation. *Nat. Nanotech.* **2020**, (15), 390-397.

37. Yates, J. T.; Kolasinski, K., Infrared Spectroscopic Investigation of the Rhodium Gem-Dicarbonyl Surface Species. *J. Chem. Phys.* **1983,** *79* (2), 1026-1030.

38. Shimizu, Y.; Mitsuhashi, H.; Caspi, E., A New Practical Synthesis of 1-dehydro-3-keto Steroids of the A/B Cis Series. *Tetrahedron Lett.* **1966,** *7* (34), 4113-4116.

39. Jain, A.; Ong, S. P.; Hautier, G.; Chen, W.; Richards, W. D.; Dacek, S.; Cholia, S.; Gunter, D.; Skinner, D.; Ceder, G.; Persson, K. A., Commentary: The Materials Project: A Materials Genome Approach to Accelerating Materials Innovation. *APL Mater.* **2013**, (1), 011002.

40. Wayland, B. B.; Ba, S.; Sherry, A. E., Activation of Methane and Toluene by Rhodium(II) Porphyrin Complexes. *J. Am. Chem. Soc.* **1991,** *113* (14), 5305-5311.

41. Choi, K. S.; Lai, T. H.; Lee, S. Y.; Chan, K. S., Reduction of Rhodium(III) Porphyrin Hydroxide to Rhodium(II) Porphyrin. *Organometallics* **2011,** *30* (10), 2633-2635.

42. Lubbe, S. C. C. V. D.; Vermeeren, P.; Ø, C.; Guerra, F.; Bickelhaupt, F. M., The Nature of Nonclassical Carbonyl Ligands Explained by Kohn – Sham Molecular Orbital Theory. *Chem. Eur. J.* **2020**, 15690-15699.

43. Meng, Y.; Qu, X.; Li, K.; Yang, Y.; Wang, Y.; Wu, Z., Rhodium and Nitrogen Codoped Graphene as a Bifunctional Electrocatalyst for the Oxygen Reduction Reaction and CO_2 Reduction Reaction: Mechanism Insights. *J. Phys. Chem. C* **2019**, *123* (9), 5176-5187.

44. Guan, H.; Lin, J.; Qiao, B.; Yang, X.; Li, L.; Miao, S.; Liu, J.; Wang, A.; Wang, X.; Zhang, T., Catalytically Active Rh Sub-Nanoclusters on TiO_2 for CO Oxidation at Cryogenic Temperatures. *Angew. Chem. Int. Ed. Engl.* **2016,** *55* (8), 2820-4.

45. McClure, S. M.; Goodman, D. W., New Insights into Catalytic CO Oxidation on Pt-Group Metals at Elevated Pressures. *Chem. Phys. Lett.* **2009,** *469* (1-3), 1-13.

46. Krenn, G.; Bako, I.; Schennach, R., CO Adsorption and CO and O Coadsorption on Rh(111) Studied by Reflection Absorption Infrared Spectroscopy and Density Functional Theory. *J. Chem. Phys.* **2006,** *124* (14), 144703.

47. Guerrero-Ruiz, A.; Maroto-Valiente, A.; Bachiller-Baeza, B.; Rodriguez-Ramos, I., Surface Properties of Supported Metallic Clusters as Determined by Microcalorimetry of CO Chemisorption. *Top. Catal.* **2002,** *19* (3), 303-311.

48. Lu, Y.; Kuo, C. T.; Kovarik, L.; Hoffman, A. S.; Boubnov, A.; Driscoll, D. M.; Morris, J. R.; Bare, S. R.; Karim, A. M., A Versatile Approach for Quantification of Surface Site Fractions

using Reaction Kinetics: The Case of CO Oxidation on Supported Ir Single Atoms and Nanoparticles. *J. Catal.* **2019,** *378*, 121-130.

49. Allian, A. D.; Takanabe, K.; Fujdala, K. L.; Hao, X.; Truex, T. J.; Cai, J.; Buda, C.; Neurock, M.; Iglesia, E., Chemisorption of CO and Mechanism of CO Oxidation on Supported Platinum Nanoclusters. *J. Am. Chem. Soc.* **2011,** *133*, 4498-4517.

50. Lu, Y.; Wang, J.; Yu, L.; Kovarik, L.; Zhang, X.; Hoffman, A. S.; Gallo, A.; Bare, S. R.; Sokaras, D.; Kroll, T.; Dagle, V.; Xin, H.; Karim, A. M., Identification of the Active Complex for CO Oxidation over Single-Atom Ir-on-$MgAl_2O_4$ Catalysts. *Nat. Catal.* **2019,** *2*, 149-156.

Chapter 4 Aerobic Oxidation of 2-propanol over Co Containing Catalysts

Abstract

As described in earlier chapters, isolated transition metal ions in N-doped carbon (M-N-C) have been proposed to activate O_2 through a CO-assisted mechanism during low temperature (< 273 K) CO oxidation catalysis. The Co-N-C and Rh-N-C catalysts utilize the N-doped carbon support and adsorbed CO to activate the O_2 with a low activation barrier. Whereas a low activation barrier for O_2 activation at low temperature was consistent with quantum chemical calculations, the high temperature kinetics of CO oxidation were not accounted for in the mechanism. In this chapter, the oxidative dehydrogenation of alcohol is explored as another reaction probe for O_2 activation. The high temperature catalysis (>273 K) for oxidative dehydrogenation of primary alcohols has been explored in liquid phase systems, but the studies are complicated by the effect of solvent and the production of acid, which can deactivate the catalyst. Here, we explore the oxidative dehydrogenation of 2-propanol over Co-N-C in both liquid and gas phase systems. The gas phase oxidative dehydrogenation over Co-N-C at 473 K has significant conversion for hours but decreases to a steady-state value similar to that observed with N-C, indicating the Co sites may not be turning over. While no conversion was observed over N-C in the liquid phase (in water solvent) at 393 K, the Co-N-C catalyst was active but stopped production of 2-propanone after 15 min. To probe the deactivation of this reaction in liquid water, 2-butanone was added to the reaction mixture. The addition of 2-butanone inhibited the reaction, which indicates that formation of product ketone deactivates the catalyst. These results suggest that there may be a highly active site for the oxidative dehydrogenation of ketone, but it deactivates quickly. The results may be

useful for understanding the mechanism where it appears that a stable product is forming that may further block the binding of reactants to turn over the catalyst.

4.1. Introduction

Transition-metal ions (M) isolated in a nitrogen-doped carbon matrix (M-N-C) have been shown to be active for reactions involving O_2 activation, with examples in both electrocatalytic[1-5] and thermocatalytic reactions.[6-8] For both of these catalytic systems, various M-N-Cs have even been shown to exhibit activity and selectivity comparable to Pt-based electrodes in case of the electrochemical oxygen reduction reaction (ORR)[5, 9, 10] and Pt nanoparticles for the organic reactions involving C-H activation at mild temperatures.[7, 8, 11, 12] Although these M-N-C catalysts exhibit high activity, mechanistic insights into the activation of O_2 have remained elusive due to the complicated effects of solvents in the case of thermocatalytic reactions or applied potentials in electrocatalytic systems.

Two mechanisms are often invoked for the thermocatalytic aerobic oxidation of organic molecules with M-N-C: (1) direct inner-sphere reactions (ISR) where organic molecules directly interact with activated O_2 or (2) two independent redox half-reactions (IHR) where oxidation of the organic molecule and reduction of O_2 occur separately.[12] Recently, thermocatalytic systems without the complications of these effects were studied. For example, the gas phase oxidation of CO was investigated on Fe-N-C, Co-N-C, and samples containing both Co and Fe (Fe-Co-N-C).[13] The Co-N-C catalyst exhibited activity at temperatures as low as dry-ice acetone.[13] Another study by our group investigated a mechanism for CO oxidation on Co-N-C using quantum chemical density functional theory (DFT) and experimental work at these low temperatures (See Chapter

2).[14] The mechanism utilized a CO molecule adsorbed on the Co ion in the N-C structure before activating the O_2 with the carbon structure and producing CO_2.[14] The binding energies of the CO and O_2 during the reaction were quite weak so the surface coverage, and therefore CO oxidation rate, decreased with increasing temperature.[14] The proposed mechanism explained the experimental results at low temperatures whereas the high temperature kinetics of CO oxidation could not be explained by that model. As the high temperature regime (> 400 K) is where liquid phase alcohol oxidative dehydrogenation reactions are often studied, we chose to explore the alcohol oxidation reaction as a complement to our prior studies on CO oxidation.

Prior work on the liquid phase oxidative dehydrogenation of benzyl alcohol showed various M-N-C catalysts were catalytically active, with Co-N-C exhibiting both high activity and decent stability.[7] Kinetic isotope effect (KIE) experiments revealed that the kinetically relevant elementary step in alcohol oxidation involved C-H activation.[8] An attempt at titrating the active sites involved adsorption of low amounts of benzoic acid as the rate decreased upon its addition.[8] After titrating for active sites, the Co-N-C catalyst was shown to have turnover frequencies for benzyl alcohol oxidative dehydrogenation on the order of Pt nanoparticles under identical conditions.[8] Interestingly, higher additions of acid did not continue to proportionally decrease the rate and thus it is possible not all sites were quantified.[8] Since not all sites were quantified and solvation effects may play a role in the mechanism, further study in the absence of some of these complicating effects is necessary to understand the mechanism and active sites for oxidative dehydrogenation on these catalysts.

In the current work, Co-N-C is investigated for both the liquid and gas phase oxidative dehydrogenation of 2-propanol. Since benzoic acid was previously used to titrate the Co sites, alcohols that can form acid products should be avoided. Therefore, we chose the short chain 2-

propanol molecule to explore as the product ketone will be unable to form an acid product. Our experiments show that while the Co-N-C catalyst initially converts the 2-propanol in both the liquid and gas phase, the gas phase reaction may not actually turn over and conversion observed at longer times might be the result of N-C. This suggests that the initial burst of activity observed with Co-N-C might be related to Co sites that are poisoned by product while the steady-state activity may be due to the N-C. Although these M-N-C catalysts are often proposed to be active for oxidative dehydrogenation reactions, they significantly deactivate over time and thus the highly active sites may not be catalytic.

4.2. Methods

4.2.1. Synthesis of Co Catalysts

The Co-N-C catalyst was synthesized using a modified high-temperature pyrolysis method that was previously developed.[7, 8, 14] To briefly summarize, Co nitrate hexahydrate (0.49 g) (Sigma-Aldrich Corporation) was dissolved in 10 cm^3 of distilled, deionized (DDI) H_2O before combining with a solution of 1, 10 phenanthroline (0.61 g) (Sigma-Aldrich Corporation) in 15 cm^3 ethanol (Sigma-Aldrich Corporation). This 1:2 molar ratio of Co/phenanthroline was then stirred for 20 min at 353 K. The mixture was then added dropwise to a 0.1 M NaOH (Sigma-Aldrich) slurry that contained 2 g of Carbon Black Pearls 2000 (Cabot Corporation) at 353 K and stirred for 2 h. The slurry was then washed and vacuum filtered with 3000 cm^3 of DDI H_2O before drying overnight in an oven at 343 K. This slurry with deposited Co-phenanthroline was then impregnated with 80 wt % dicyandiamide (Aldrich) relative to the slurry complex in 10 cm^3 acetone (Fischer Chemical, Historical Grade). The solution was vigorously stirred at 343 K and dried overnight. Multiple

batches were combined until 0.2 g could be heated in ultrahigh purity (UHP) N_2 (100 cm^3 min^{-1}) (99.999 %, Praxair) at 10 K min^{-1} and held at 973 K. Any nanoparticles that formed during the thermal treatment were removed via a vigorously stirred 1 M HCl (VWR Chemicals, ACS Grade) solution (100 cm^3) with 0.1 g of catalyst at room temperature for 12 h. The acid-washed catalyst was then washed with 3000 cm^3 of DDI H_2O before drying overnight at 353 K. A thermal treatment in flowing UHP H_2 (100 cm^3 min^{-1}) (5 % H_2/Ar, Praxair) with a 10 K min^{-1} ramp to 673 K and a hold at 2 h was used to produce the as synthesized Co-N-C. A metal-free nitrogen-carbon catalyst (N-C) was also synthesized via the impregnation of an aqueous solution of 0.4 g dicyandiamide into 0.5 g Carbon Black Pearls 2000 with the same thermal treatment method described for the Co-N-C catalyst. A 4.78 wt % Co/SiO_2 catalyst was synthesized via incipient wetness impregnation of Co nitrate hexahydrate (0.5 g) dissolved in 2.5 cm^3 of DDI H_2O into silica gel (2 g) (Davisil 636).[15, 16] The catalyst was subsequently dried overnight at room temperature before another 2 h drying in an oven at 393 K. A thermal treatment with a ramp of 10 K min^{-1} to 673 K (2 h hold) in flowing air (Medical Grade, Praxair) was used to decompose the nitrate and leave behind the Co on silica (Co/SiO_2). A 2.29 wt % Co/CB catalyst was synthesized by incipient wetness impregnation of Co acetate tetrahydrate (0.04 g, Aldrich) dissolved in 1 cm^3 DDI H_2O onto Carbon Black Pearls 2000 (0.2 g). The mixture was dried at 393 K overnight before thermally treating at 973 K for 2 h (ramp at 10 K min^{-1}) in flowing UHP He (99.999 %, Praxair). A Co_3O_4 sample (Co (II, III) oxide from Alfa Aesar) was thermally treated for 5 h at 673 K in 100 cm^3 min^{-1} flowing air (ramp at 10 K min^{-1}) and used as treated.

4.2.2. Calculation of the Exposed Co on the Co_3O_4 Sample

Dinitrogen physisorption was performed on a Micromeritics ASAP 2020 automated adsorption system to determine the surface area of the Co oxide. Prior to N_2 physisorption at 77 K, a degas of the sample was done at 723 K under vacuum. The Brunauer-Emmett-Teller (BET) method was used to calculate the total surface area of the oxide catalyst, yielding 239 $m^2\ g^{-1}$. Since this surface area is inclusive of all surface sites including the exposed O and Co species, further calculation was needed to determine the grams of Co on the surface to normalize rates by Co. By using the density of Co_3O_4 (6.11 g cm^{-3}) and the relationship between surface area and volume of the particles, a radius based on the average particle size was calculated (2.05 nm). The volume based on the surface area was then calculated with this radius and the density of Co oxide with allow for Co per volume to be calculated. Now that the moles of Co per particle is known, the surface moles of Co can be calculated by understanding the Co per surface area in a unit cell. Thus, a (111) plane of Co_3O_4 was used since it has been reported to be the most common plane for Co_3O_4.[17] Taking the unit cell diameter and the number of exposed Co atoms per unit cell (2) we can determine the moles of Co m^{-2}. Using the radius of the particles we can calculate the amount of Co on the surface as we can calculate the surface area of an average particle. By dividing this number with the previously calculated Co per bulk particle, we can get the dispersion. The dispersion then is multiplied by the mass of Co added to the reaction to yield the grams of Co on the surface of the particles. This value was used to determine the reaction rate $g^{-1}_{Co}\ s^{-1}$.

4.2.3. Oxidative Dehydrogenation of Gas Phase 2-propanol in a Continuous-Flow Reactor

The oxidative dehydrogenation of 2-propanol was carried out in a stainless steel, down flow, continuous packed bed reactor. The catalyst (0.2 g) was diluted in 3 g of SiC (Universal

Photonics, Inc, 150 mesh) for each reaction. The reaction was run with 43 cm^3 min^{-1} total gas flow with 6.7 % 2-propanol (Fischer Chemical, ACS Plus grade), 14 % O_2 (Medical Air, Praxair), and balance He (Praxair, 99.999 %) at atmospheric pressure. Prior to the reaction run, each catalyst was thermally pretreated in situ by ramping at 10 K min^{-1} to 673 K and holding for 2 h in He before cooling down in He to the reaction temperature. The 2-propanol was introduced to the reactor by a saturator that was fed by a liquid pump with a mixture of air and diluent He comprising the rest of the reaction gas feed. The reactor effluent was analyzed by an SRI 8610 C gas chromatograph (GC) equipped with a flame ionization detector. The products were separated by a Restek MXT-WAX column operating isothermally at 373 K for 6 min. The retention times and calibration curves were determined by injection of known concentrations of 2-propanol (Fischer Chemical, ACS Plus) and 2-propanone (Fischer Chemical, Histological Grade). The relative responses were used to quantify the production of propene, which was another product formed in low concentrations. The conversion was based on product formed, determined by the production of 2-propanone and propene. Selectivity was defined as the molar amount of that product formed divided by the molar amount of both products formed during reaction. For co-feed experiments, the amount of inert He was proportionally decreased to keep the total flow rate through the reactor the same. The co-feed experiments were run with silica gel (Davisil 636) instead of the SiC as the diluent.

4.2.4. Oxidative Dehydrogenation of Liquid Phase 2-propanol in a Batch Reactor

High-pressure, liquid phase, semi-batch alcohol oxidation reactions were performed in a 50 cm^3 Parr Instrument Company 4592 batch reactor with a 30 cm^3 glass liner. In a typical reaction, the glass liner was filled with 10 cm^3 of aqueous 2-propanol (Fischer Chemical, ACS Plus) solution (0.01 M) and 0.025 or 0.05 g of catalyst before being inserted into the reactor, sealed, and purged

with O_2. The reactor was preheated to the reaction temperature and then the reaction was initialized by purging and pressurizing the reactor with pure O_2. Liquid samples were taken periodically and filtered with 0.2 μm PTFE filters before injection with a known carbon standard (ethanol or 1-butanol) (Sigma-Aldrich 99.5 % and Sigma-Aldrich 99.8 %, respectively) into an Agilent 7890 A GC equipped with a flame ionization detector. The products were separated by a Varian CP-Poraplot capillary column operating at 393 K for 15 min before ramping at 10 K min^{-1} to 473 K and holding for 10 min with a flow rate of 2.44 cm^3 min^{-1}. The retention times and calibration curves were determined by injecting known concentrations of 2-propanol and 2-propanone (Fischer Chemical, Histological Grade) and a known standard of 0.1 M ethanol or 1-butanol. The carbon balance will be further discussed in the Results Section 4.3. For co-feed experiments, the reaction was run as previously described but included a solution of the co-feed (NaOH or 2-butanone (Sigma-Aldrich, 99 + %). These samples were filtered and injected without further purification into the GC.

4.2.5. Density Functional Theory Calculations

We performed spin-polarized periodic supercell density functional theory (DFT) calculations with a plane wave basis set and 500 eV as an energy cutoff using the Vienna ab initio simulation package (VASP)[18] version 5.4.4. The structures were converged to a criterion of 10^{-6} eV and 0.01 eV $Å^{-1}$ for self-consistent-field (SCF) energies and atomic forces, respectively. Structures were generated by removing two carbon atoms from a 8.5 Å by 9.8 Å graphene supercell with 14 Å vacuum in the z-direction for a total of total of 30 C atoms (when the number of N atoms is zero). The carbon atoms surrounding the defect site were modified with 4 pyridinic N to create the site often claimed to be active for oxidative dehydrogenation reactions.[14, 19] Monkhorst-Pack

k-points were optimized to 4 X 4 X 1 mesh. The energies are reported rather than free energies since the binding of adsorbates was directly compared to previously calculated binding energies of CO and O_2 to the isolated Co ion which were weakly adsorbed and thus they are not amenable to standard free energy approximations.[14] Further, vibrational zero-point energy corrections were neglected as they should have a negligible contribution to our reaction energies for this system. We are reporting the energies with van der Waals density functional (vdW-DF)[20] computed values as the functional was previously used to calculate CO and O_2 binding energies on the same Co-N-C structure, which we want to compare our binding energies to.

4.3. Results and Discussion

4.3.1. Oxidative Dehydrogenation of 2-propanol over Co Catalysts in the Gas Phase

To determine the effect of support composition on catalytic performance, the oxidative dehydrogenation of 2-propanol was evaluated over a suite of Co catalysts and the metal-free N-C. A 1.89 wt % Co-N-C catalyst was synthesized using a modified high temperature pyrolysis method (See Methods Section 4.2).[14] This catalyst has been previously investigated by our group, with no Co nanoparticles being detected upon inspection with aberration corrected high-angle annular dark-field scanning transmission electron microscopy (STEM) (Chapter 2 Fig. 2.1).[14] In addition to the Co-N-C, various other Co-containing catalysts were investigated, including a commercial Co_3O_4, a highly dispersed 4.78 wt % Co/SiO_2, and nitrogen-free 2.29 wt % Co/CB. These catalysts were tested for the oxidative dehydrogenation of 2-propanol using a flow reactor over a range of temperatures (393 - 473 K) at atmospheric pressure. To understand if background activity was present in the system, the Co-N-C catalyst was tested without the presence of O_2 over the whole

temperature range. In the reaction run without O_2 there was a constant 0.3 % conversion which resulted in a rate of dehydrogenation (0.7×10^{-7} mol 2-propanone formed g_{cat}^{-1} s^{-1} formed) over the whole range of temperatures. This rate was significantly lower than the observed rates of oxidative dehydrogenation and confirmed that O_2 was necessary for the measured activity of all catalysts. To further probe the background activity, a tube with just the SiC diluent was added to the reactor and resulted in a conversion of 0.1 % (an order of magnitude less than the studied catalysts at the same temperature).

Figure 4.1 illustrates the catalytic performance of the Co-containing catalysts (at conversions less than 10 %) and a metal free N-C at 473 K. The Co-N-C catalyst exhibits a high initial reaction rate that declines over time to the same rate per gram of catalyst as the metal-free N-C material. The rates were based on 2-propanone formation since the selectivity for the products from all catalyst was > 95 % 2-propanone with the balance being propene. Comparing Co-N-C with the other catalysts, the Co/SiO_2 and N-C materials have similar rates of 2-propanone formation on a per mass basis at these conditions while the Co/CB had a significantly lower rate. However, the mass basis of rate normalization improperly estimates the amount of active material in each sample. When instead normalizing the rate of reaction in the steady-state regime by the mass of Co, the Co/SiO_2 and Co/CB catalysts had approximately the same rate of 2-propanone formation (220×10^{-7} and 211×10^{-7} mol 2-propanone formed g_{Co}^{-1} s^{-1} respectively). The Co_3O_4 had the highest activity on a per mass of catalyst basis and had a higher rate per exposed Co than the supported Co catalysts (576×10^{-7} mol 2-propanone formed g_{Co}^{-1} s^{-1}). The derivation of this Co amount was discussed in Methods Section 4.2.2. but is considered to be an underrepresentation of the amount of exposed Co and thus it is possible that the Co/CB, Co/SiO_2, and Co_3O_4 had similar rates of reaction on an exposed Co basis. Further, the observed activity for the bulk Co oxide

catalyst is consistent with the previously reported conversion of 2-propanol above 430 K for unsupported Co_3O_4 spinel nanoparticles.[21] The Co oxide spinel catalyst was proposed to proceed through a mechanism involving nucleophilic atomic oxygen species formed from the redox of Co^{3+}/Co^{2+} in the selective production of 2-propanone.[21] This mechanism might be applicable to the observed activity on small clusters of Co oxide on Co/SiO_2, Co/CB, and the high initial activity regime for Co-N-C. Although no metal particles have been detected on this catalyst through STEM imaging and X-ray absorption spectroscopy (see Chapter 2), small quantities of Co oxide may be present on the Co-N-C. Ultimately a comparison for Co-N-C by amount of Co cannot be made since the N-C appears to be active and thus this similarity is further explored.

The comparable rates of reaction on N-C (on a mass basis) and Co-N-C after a long time on stream suggests that the high conversion observed over Co-N-C at short times on stream is mostly associated with Co. To investigate this concept, the excess moles of 2-propanone formed above the background steady-state rate during the initial period of rapid deactivation was calculated by first removing the background conversion associated with N-C, assuming there is a comparable amount of N-C in the Co-N-C compared to the just N-C reaction run. In other words, the amount of 2-propanone produced above steady state in the initial deactivating period was determined by integrating the area under the rate curve in Fig. 4.1 and subtracting the integrated amount of 2-propanone formed at the steady state rate. The excess moles of 2-propanone formed above steady state was then compared to the amount of Co in the Co-N-C catalyst. The weight percent of Co was previously determined by inductively coupled plasma optical emission spectroscopy (ICP-OES) to be 1.89 wt %.[14] Dividing the moles of 2-propanone by the moles of Co gives a ratio of 2:1, which is the stoichiometric ratio predicted from the overall reaction of two molecules of 2-propanol reacting with one O_2 molecule to produce 2 molecules of 2-propanone

and 2 molecules of water. Thus, the initial deactivation appears to be stoichiometric with O_2 to Co. A deactivated Co-N-C catalyst was thermally treated in He at 673 K for 2 h and cooled to the reaction temperature, after which the high initial activity of 2-propanol conversion was again observed. The deactivation occurs on various loadings of catalyst as well. Appendix Fig. C1 shows the reaction rate in the initial period of deactivation for three different loadings of catalyst (0.05, 0.1 and 0.2 g). The overlap of the reaction profiles for the 0.05 and 0.1 g catalyst loadings are expected since the rate was normalized by catalyst mass. The highest loading of 0.2 g apparently had artifacts in the measured rate. Nevertheless, significant deactivation was seen in all cases.

The steady-state observed orders of reaction for 2-propanol and O_2 during the oxidative dehydrogenation of 2-propanol for all catalysts are similar (Table 4.1). The similar positive order dependence for all catalysts on 2-propanol is indicative of weak adsorption on the reactant on the surface. This positive order for 2-propanol for Co-N-C contrasts with the reported zero order dependence for both the alcohol and O_2 during the benzyl alcohol oxidative dehydrogenation reaction in the liquid phase on Co-N-C.[7] The zero order dependence could indicate a saturation of both reactant species on two separate sites on the catalyst surface. In a two-site mechanism, there could be activation of the O_2 on one site while C-H activation on the 2-propanol occurs on another. This mechanism is reminiscent of the previously reported IHR reaction where two different sites complete the reduction of the O_2 and the oxidation of the alcohol.[12] A significant difference in the saturated benzyl alcohol case versus the 2-propanol system could be attributed to the inability of the 2-propanol to pi-pi stack on the carbon structure like aromatic molecules can.[22] The reaction order for 2-propanol was also lower for the N-C catalyst compared to the one over Co-N-C. Since all reaction orders were collected in the steady-state regime where Co is assumed to be deactivated, it is unclear why the alcohol order is different. Contrasting with the alcohol, the slightly negative

reaction order for O_2 during the 2-propanol oxidative dehydrogenation reaction over both N-C and Co-N-C indicates that there may be competitive adsorption of O_2 on the same site as the alcohol. More work needs to be done to understand how the O_2 and alcohol are activated. Further spectroscopic analysis is needed to understand how the O_2 is activated on these catalysts.

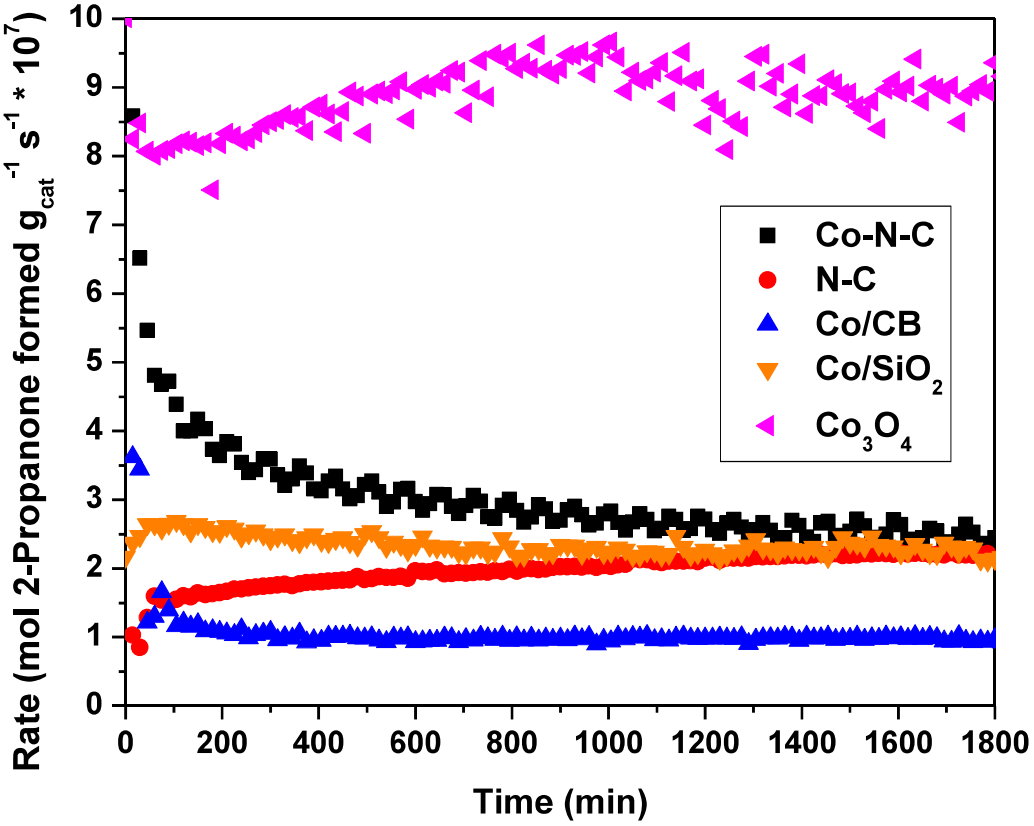

Figure 4.1. Formation rate of 2-propanone versus time over a variety of Co-containing catalysts. Each catalyst was thermally treated in He at 673 K before starting the reactor upon cooling to 473 K and switching the gas flow to the reactants. The reaction was run with 0.2 g of catalyst diluted in SiC with 43 cm^3 min^{-1} total gas flow, 6.7 % 2-propanol, 14 % O_2, and balance He at atmospheric pressure. The selectivity to 2-propanone was > 95 % throughout the reaction run time.

Table 4.1. Summary of Kinetic Parameters for the Oxidative Dehydrogenation of 2-propanol over Various Co-Containing Catalysts

catalyst	E_a[a]	orders of reaction[b]	
	(kJ mol^{-1})	2-propanol	O_2
Co-N-C	63	0.9	-0.3
N-C	58	0.5	-0.4
Co/CB[c]	-	1.4	0
Co/SiO_2	67	0.8	0.2
Co_3O_4	80	0.6	0

[a]Apparent activation energy was determined from an Arrhenius-type plot shown in Appendix Fig. C2.
[b]Kinetic orders were evaluated under steady-state differential conversion (< 20 %) and were determined by varying the partial pressure of 2-propanol (6.8 to 12.5 kPa) or O_2 (2.0 to 16.4 kPa) while maintaining the other. Kinetic order plots are presented in Appendix Figs. C3 a and b.
[c]Conversion was too low at 473 K to go to lower temperatures for apparent activation energy calculations.

The Co-N-C, N-C, and Co/SiO_2 catalysts all had approximately the same apparent activation energy (Table 4.1) in the long time steady-state regime. Although the Co in the Co-N-C is assumed to be mainly in isolated Co sites, some Co oxide nanoclusters may have formed during the high temperature thermal treatment. Furthermore, even though Co/SiO_2 and Co/CB are highly dispersed there could be small Co clusters which are known to be difficult to reduce.[23] These Co clusters however, do not explain the similar activity that the N-C has. The similarity could be a coincidence since the N-C does not have Co present. The N-C has basic sites on the exposed N species that could play a role in the oxidative dehydrogenation as has been previously reported to occur for propane oxidative dehydrogenation.[24] During that reaction, positive order kinetics were reported in both alkane and O_2.[24] Interestingly, the increase in activity with time was

also apparent for the propane oxidative dehydrogenation reaction with the authors attributing the initial increase in activity to the in situ rearrangements of "functionalities and carbon debris" on the carbon surface.[24] The functionalities are carbonyls formed after activating O_2 and are known to react with C-H bonds in propane.[24-27]

4.3.2. Effect of Co-feeds on High Initial Activity for Co-N-C during the Gas-Phase Oxidative Dehydrogenation of 2-Propanol

To further investigate the initial deactivation of the Co-N-C catalyst, a series of molecules were co-fed to the reactor. Figure 4.2 shows the effect of various co-feeds on the rate of 2-propanone formed over time. The rates were unaffected when co-feeding H_2O, a product of the oxidative dehydrogenation of 2-propanol. Likewise, CO did not have any effect on the reaction rate, which is consistent with our earlier work showing weak binding of CO to the Co.[14] Moreover, the product of CO oxidation, CO_2, also did not have an effect on the reaction rate. Interestingly, co-feeding NH_3 greatly inhibited the 2-propanol reaction, and, after stopping the NH_3 feed, the conversion of 2-propanol returned to the prior steady-state level before NH_3 exposure. Since it was unclear how NH_3 could inhibit the reaction while CO did not, computational quantum chemical calculations with DFT were used. Full computational details are provided in the Methods Section 4.2. In brief, the bare Co-N-C structures from Chapter 2 were used with the addition of an NH_3 molecule. Figure 4.3 shows the binding of NH_3 to Co (a) and the adjacent C (b). Whereas the binding energy of CO on the Co ion was 57 kJ mol^{-1}, the NH_3 binding energy using the same functional and settings was 30 kJ mol^{-1}.[14] The weaker binding of NH_3 on Co relative to CO and the lack of CO inhibition on the 2-propanol reaction suggest the oxidative alcohol dehydrogenation reaction may not proceed over the Co ion. The carbon atom adjacent to the pyridinic N was also

investigated as another possible site for NH_3 binding since it is often reported as the active site for metal free (N-C) ORR. This site also had a weak NH_3 binding energy of 15 kJ mol^{-1}. Evidently, further work is needed to explain the observed deactivation of the oxidative dehydrogenation of 2-propanol caused by co-feeding NH_3.

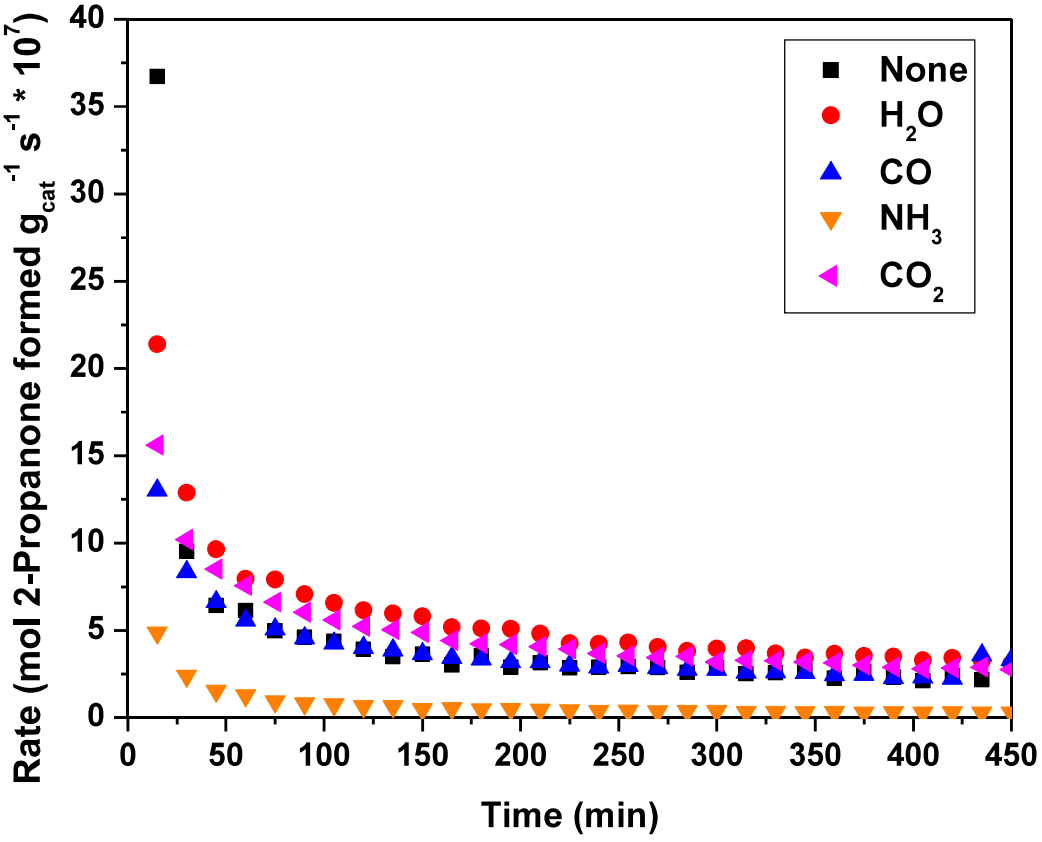

Figure 4.2. Rate of 2-propanone formation on Co-N-C over time with various co-feeds. The catalyst was treated in He at 673 K and cooled to 403 K prior to starting reactant flow. The reaction was run with 43 cm^3 min^{-1} total gas flow, 6.7 % 2-propanol, 14 % O_2, and 21 % co-feed with balance N_2 at atmospheric pressure. The selectivity to 2-propanone was > 95 % throughout the reaction run time. These experiments were run before switching the diluent to SiC. The silica gel does appear to have higher background activity compared to the SiC (0.5 % conversion) and thus the reaction rates when adding in the catalyst are higher than those reported in Fig. 4.1 even though those reaction were run at higher temperatures.

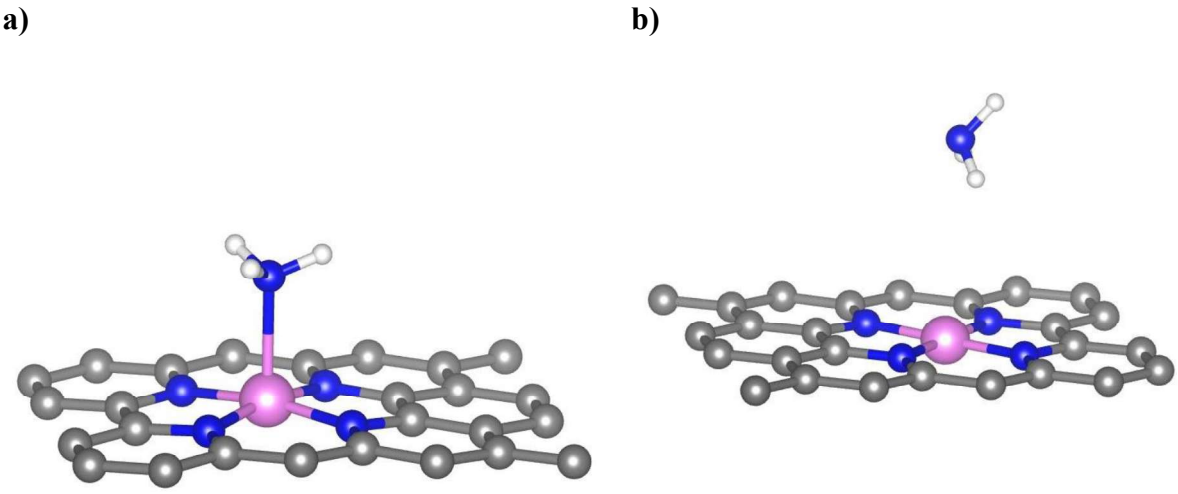

Figure 4.3. a) Geometry optimized structures for NH_3 on Co (a) and C (b) using vdW-DF.

4.3.3. Oxidative Dehydrogenation of 2-Propanol over Co Catalysts in the Liquid Phase

To probe the effect of solvent on the catalytic performance of the Co-N-C catalyst, the oxidative dehydrogenation of 2-propanol was evaluated in liquid water using a pressurized batch reactor at various temperatures. The reactor was heated before the addition of the alcohol-water solution with catalyst and the reaction was initialized after purging with pure O_2 and pressurizing with pure O_2. Conversion of 2-propanol was observed when Co-N-C was used as a catalyst in the temperature range studied (353 – 403 K) after 60 min of reaction time (Table 4.2), with the other Co catalysts being completely inactive or exhibiting only trace conversion of 2-propanol. Figure 4.4 shows the conversion of 2-propanol with Co-N-C at various time points, up to 90 min. Each time point was acquired from a separate reaction run under identical reaction conditions, i.e., Fig. 4.4 shows results from 4 separate reaction runs. If the catalyst continued to turn over throughout the 90 min, conversion should increase with reaction time. In this case, the conversion of 2-propanol reached about 4% in the first 15 min and remained at that level at longer times. A plateau

in conversion was previously reported for the oxidative dehydrogenation of benzyl alcohol and was attributed to the formation of benzoic acid, which can poison the catalyst.[8] Since 2-propanol is a secondary alcohol that forms a ketone upon oxidative dehydrogenation, the deactivation observed here is likely attributed to something other than acid formation.

As the catalyst deactivated quickly in the liquid phase, determining kinetic parameters for the reaction is problematic. In an attempt to gain some rudimentary insight into the kinetics of the reaction, the average rate of reaction was determined from the conversion after 30 min of reaction. In that fashion, the kinetic orders were evaluated at 388 K after 30 min by varying the concentration of 2-propanol (0.1 to 0.4 M) or O_2 pressure (600 to 1600 kPa) while maintaining the other. The kinetics for the liquid phase reaction over Co-N-C are similar to those in the gas phase where positive order dependence on the alcohol (0.6) and nearly zero-order dependence on O_2 were observed. Plots used to determine the reaction orders are presented in Appendix Fig. C4 a and b. As discussed earlier, the gas phase reaction deactivated significantly over many hours and the liquid phase reaction appeared to follow a similar trend. The conversion evaluated at the earliest time point (15 min) of the liquid phase reaction (Fig. 4.4) has likely already been affected by deactivation, which complicates comparisons to steady state results measured in the gas phase. The reaction of 2-propanol in the liquid phase does need O_2 to proceed as reactions run at atmospheric pressure without O_2 but with N_2 (Praxair, 99.999 % and with OMI Indicator) showed no activity. We attempted to use the presence or absence of H_2O_2 during reaction as a signal for whether or not a two or four electron reaction path occurs for the oxygen reduction reactions over M-N-C catalysts.[12, 28] The formation of H_2O_2 during the reaction was investigated using UV-Vis spectroscopy of the product solution in dilute sulfuric acid and $TiO_2(SO_4)$ as an indicator.[29] When

titrating the product solution, no H_2O_2 was detected. Thus, water is produced as the main reduced species from O_2 activation, the product of a 4-electron reduction.

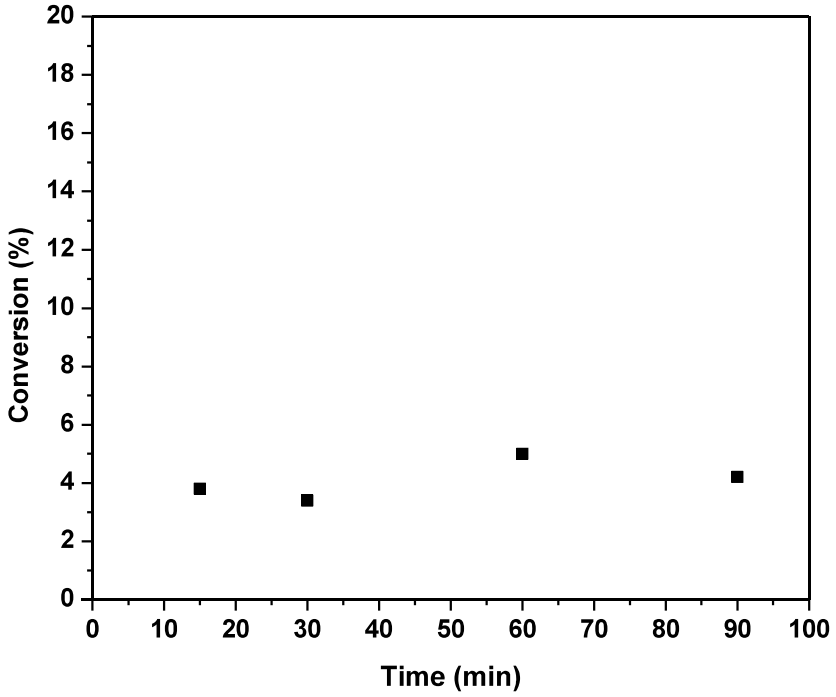

Figure 4.4. Time evolution of the oxidative dehydrogenation of 2-propanol in liquid water with 0.025 g Co-N-C catalyst.
Each point is a separate reaction run at 393 K. To analyze the conversion, the reactor was first cooled down to 273 K before filtering out the catalyst and injecting the solution into the GC. Note that the y-axis is from 0 to 20 % instead of 100 % conversion to show relative differences in conversion.

To understand why the Co-N-C deactivated, various molecules were added to the solution and run with the reaction mixture (Table 4.3). Previous literature has shown that the presence of base accelerates oxidative dehydrogenation reactions involving Co-N-C catalysts.[8] The presence of base during the oxidative dehydrogenation of 2-propanol does seem to accelerate the rate (Table 4.3). It should be noted that the carbon balance for the reaction run with base is close to 100 %. This complete recovery contrasts with the reaction run without base where only 81 % of the carbon is accounted for after the same reaction time. This difference might suggest that the base does not

actually accelerate the reaction rate but rather promotes desorption of the product ketone. Thus, the effect of ketone was also investigated. Table 4.3 shows the effect of the addition of a slightly larger ketone (2-butanone) to the 2-propanol reaction. Addition of 0.001 M 2-butanone had no detectable impact on the reaction rate after 15 min but higher molarity solutions of 0.01 and 0.1 M 2-butanone significantly inhibited the rate of oxidative dehydrogenation of 2-propanol. Evidently the presence of ketone in the reaction is detrimental to catalytic performance, which could account for some of the deactivation of the 2-propanol reaction. For the Co-N-C and N-C catalysts, the carbon balance was 20 % lower than complete carbon recovery (Table 4.2). This contrasts with the nitrogen-free materials (Co/SiO_2, Co/CB, and Co_3O_4) which did not produce 2-propanone but still had ~100 % of the carbon accounted for in the reactor. Evidently, adsorption of product 2-propanone (and perhaps even 2-propanol) onto the catalyst can account for the decrease in carbon recovery on N-C materials. The hypothesis that nitrogen sites of N-C adsorb 2-propanone and 2-propanol is consistent with studies on the use of N-C as a trap for volatile organic compounds.[30, 31] Quantum chemical DFT calculations on the binding energy of 2-propanone to various N-type sites found that 2-propanone would bind to the sites with energies around 45 kJ mol^{-1} (35 to 55 kJ mol^{-1}).[32, 33] These binding energies suggest that the adsorption would be weak but the reactor needs to be cooled down before removing the aliquot to inject into the GC to condense any evaporated alcohol or ketones and thus could be remaining on the catalyst. Moreover, we cannot rule out the possibility that aldol condensation of the product 2-propanone on the basic N-C sites to form heavier products that do not desorb from the catalyst surface might also lower the carbon recovery.[34] With these considerations, we cannot confidently claim that the 2-propanol reaction over N-C did not take place over the 60 min reaction time.

Table 4.2. Liquid Phase Oxidative Dehydrogenation of 2-propanol over Various Catalysts[a]

Entry	Catalyst	Conversion (%)	Recovery (%)
1	Co-N-C	5.0	81
2	N-C	0	75
3	Co/SiO_2	0	98
4	Co/CB	0.2	96
5	Co_3O_4	0	99

[a]Reaction conditions: 10 cm^3 of 0.1 M 2-propanol aqueous solution, 1 MPa O_2, 393 K with 0.025 g of catalyst. The reported conversion is after 60 min of reaction.

Table 4.3. Liquid Phase Oxidative Dehydrogenation of 2-propanol over Co-N-C with Additives[a]

Entry	Additive	Conversion (%)	Recovery (%)
1	-	3.5	72
2	0.1 M NaOH	7.9	97
3	0.001 M 2-butanone	3.5	73
4	0.01 M 2-butanone	1.5	76
5	0.1 M 2-butanone	0.5	95

[a]Reaction conditions: 10 cm^3 of 0.1 M 2-propanol aqueous solution, 1 MPa O_2, 393 K with 0.025 g of Co-N-C catalyst. The reported conversion is after 15 min of reaction.

4.4. Conclusions

Our results suggest that Co-N-C has a very high initial catalytic activity for both the liquid and gas phase oxidative dehydrogenation of 2-propanol but suffers from severe deactivation. The steady-state regime of the 2-propanol study indicates that the support N-C may be contributing most of the reaction rate and that the Co component of the catalyst may only produce 2-propanone in a rapid stoichiometric reaction. In the gas phase, the reaction was severely inhibited by co-fed ammonia, which supports the idea that Co is not the active site at the steady state (after deactivation). In the liquid phase, addition of 2-butanone inhibited the conversion of 2-propanol, indicating product 2-propanone could also impact the reaction. In addition, adsorption of 2-propanone and 2-propanol on the N-C materials affects carbon recovery and complicates reaction kinetics.

4.5. References

1. Zhang, G.; Jia, Y.; Zhang, C.; Xiong, X.; Sun, K.; Chen, R.; Chen, W.; Kuang, Y.; Zheng, L.; Tang, H.; Liu, W.; Liu, J.; Sun, X.; Lin, W.-F.; Dai, H., A General Route via Formamide Condensation to Prepare Atomically Dispersed Metal–Nitrogen–Carbon Electrocatalysts for Energy Technologies. *Energy & Environ. Sci.* **2019,** *12* (4), 1317-1325.

2. Liu, Q.; Zhang, J., Graphene Supported Co-g-C_3N_4 as a Novel Metal-Macrocyclic Electrocatalyst for the Oxygen Reduction Reaction in Fuel Cells. *Langmuir*, **2013**, (29), 3821-3828.

3. Zitolo, A.; Ranjbar-Sahraie, N.; Mineva, T.; Li, J.; Jia, Q.; Stamatin, S.; Harrington, G. F.; Lyth, S. M.; Krtil, P.; Mukerjee, S.; Fonda, E.; Jaouen, F., Identification of Catalytic Sites in Cobalt-Nitrogen-Carbon Materials for the Oxygen Reduction Reaction. *Nat. Commun.* **2017**, (8), 957.

4. Zitolo, A.; Goellner, V.; Armel, V.; Sougrati, M.-T.; Mineva, T.; Stievano, L.; Fonda, E.; Jaouen, F., Identification of Catalytic Sites for Oxygen Reduction in Iron- and Nitrogen-Doped Graphene Materials. *Nat. Mater.* **2015**, (14), 937-942.

5. Liang, H. W.; Wei, W.; Wu, Z. S.; Feng, X.; Müllen, K., Mesoporous Metal-Nitrogen-Doped Carbon Electrocatalysts for Highly Efficient Oxygen Reduction Reaction. *J. Am. Chem. Soc.*, **2013**, (135), 16002-16005.

6. Li, M.; Wu, S.; Yang, X.; Hu, J.; Peng, L.; Bai, L.; Huo, Q.; Guan, J., Highly Efficient Single Atom Cobalt Catalyst for Selective Oxidation of Alcohols. *Appl. Catal. A: General*, **2017**.

7. Xie, J.; Yin, K.; Serov, A.; Artyushkova, K.; Pham, H. N.; Sang, X.; Unocic, R. R.; Atanassov, P.; Datye, A. K.; Davis, R. J., Selective Aerobic Oxidation of Alcohols over Atomically-Dispersed Non-Precious Metal Catalysts. *ChemSusChem*, **2017**, (10), 359-362.

8. Xie, J.; Kammert, J. D.; Kaylor, N.; Zheng, J. W.; Choi, E.; Pham, H. N.; Sang, X.; Stavitski, E.; Attenkofer, K.; Unocic, R. R.; Datye, A. K.; Davis, R. J., Atomically Dispersed Co and Cu on N-Doped Carbon for Reactions Involving C–H Activation. *ACS Catal.* **2018**, (8), 3875-3884.

9. Malko, D.; Kucernak, A.; Lopes, T., In Situ Electrochemical Quantification of Active Sites in Fe-N/C Non-Precious Metal Catalysts. *Nat. Commun.* **2016**, (7), 1-7.

10. Shao, M.; Chang, Q.; Dodelet, J.-P.; Chenitz, R., Recent Advances in Electrocatalysts for Oxygen Reduction Reaction. *Chem. Rev.* **2016**, (116), 3594-3657.

11. Huang, K.; Fu, H.; Shi, W.; Wang, H.; Cao, Y.; Yang, G.; Peng, F.; Wang, Q.; Liu, Z.; Zhang, B.; Yu, H., Competitive Adsorption on Single-Atom Catalysts: Mechanistic Insights Into the Aerobic Oxidation of Alcohols over Co–N–C. *J. Catal.* **2019**, (377), 283-292.

12. Bates, J. S.; Johnson, M. R.; Khamespanah, F.; Root, T. W.; Stahl, S. S., Heterogeneous M-N-C Catalysts for Aerobic Oxidation Reactions: Lessons from Oxygen Reduction Electrocatalysts. *Chem. Rev*, **2022**, *123* (9), 6233-6256.

13. Wang, J.; You, R.; Zhao, C.; Zhang, W.; Liu, W.; Fu, X. P.; Li, Y.; Zhou, F.; Zheng, X.; Xu, Q.; Yao, T.; Jia, C. J.; Wang, Y. G.; Huang, W.; Wu, Y., N-Coordinated Dual-Metal Single-Site Catalyst for Low-Temperature CO Oxidation. *ACS Catal.* **2020**, (10), 2754-2761.

14. Whitcomb, C. A.; Sviripa, A.; Schapowal, M. I.; Mamedov, K.; Unocic, R. R.; Paolucci, C.; Davis, R. J., Mechanistic Insights on the Low-Temperature Oxidation of CO Catalyzed by Isolated Co Ions in N-Doped Carbon. *ACS Catalysis* **2022,** *12* (24), 15529-15540.

15. Lam, Y. L.; Boudart, M., Preparation of Small Au-Pd Particles on Silica. *J. Catal*, **1977**, (50), 530-540.

16. Kaylor, N.; Xie, J.; Kim, Y. S.; Pham, H. N.; Datye, A. K.; Lee, Y. K.; Davis, R. J., Vapor Phase Deoxygenation of Heptanoic Acid over Silica-Supported Palladium and Palladium-Tin Catalysts. *J. Catal.* **2016**, (344), 202-212.

17. Singh, J.; Singh, G. P.; Jain, R. K.; Singh, B.; Singh, K. J.; Singh, R. C., Effect of Calcination Temperature on Structural, Optical and Antibacterial Properties of Ball Mill Synthesized Co_3O_4 Nanomaterials. *J. Mater. Sci.: Mater. Electronics* **2022,** *33* (6), 3250-3266.

18. Kresse, G.; Furthmuller, J., Efficient Iterative Schemes for Ab Initio Total-Energy Calculations using a Plane-Wave Basis Set. *Phys. Rev. B* **1996,** *54* (16), 11169-11186.

19. Kropp, T.; Mavrikakis, M., Transition Metal Atoms Embedded in Graphene: How Nitrogen Doping Increases CO Oxidation Activity. *ACS Catal.*, **2019**, (9), 6864-6868.

20. Dion, M.; Rydberg, H.; Schroder, E.; Langreth, D. C.; Lundqvist, B. I., van der Waals Density Functional for General Geometries. *Phys. Rev. Lett.* **2004,** *92* (24), 246401.

21. Anke, S.; Bendt, G.; Sinev, I.; Hajiyani, H.; Antoni, H.; Zegkinoglou, I.; Jeon, H.; Pentcheva, R.; Roldan Cuenya, B.; Schulz, S.; Muhler, M., Selective 2-Propanol Oxidation over Unsupported Co_3O_4 Spinel Nanoparticles: Mechanistic Insights into Aerobic Oxidation of Alcohols. *ACS Catal.*, **2019**, (9), 5974-5985.

22. Björk, J.; Hanke, F.; Palma, C.-A.; Samori, P.; Cecchini, M.; Persson, M., Adsorption of Aromatic and Anti-Aromatic Systems on Graphene through π−π Stacking. *J. Phys. Chem. Lett.* **2010,** *1* (23), 3407-3412.

23. Khodakov, A. Y.; Lynch, J.; Bazin, D.; Rebours, B.; Zanier, N.; Moisson, B.; Chaumette, P., Reducibility of Cobalt Species in Silica-Supported Fischer–Tropsch Catalysts. *J. Catal.* **1997,** *168* (1), 16-25.

24. Chen, C.; Zhang, J.; Zhang, B.; Yu, C.; Peng, F.; Su, D., Revealing the Enhanced Catalytic Activity of Nitrogen-Doped Carbon Nanotubes for Oxidative Dehydrogenation of Propane. *Chem Commun* **2013,** *49* (74), 8151-3.

25. Li, X.; Yuan, Z.; Liu, Y.; Yang, H.; Nie, J.; Wang, G.; Liu, B., Nitrogen-Doped Carbon as a Highly Active Metal-Free Catalyst for the Selective Oxidative Dehydrogenation of N-Heterocycles. *ChemSusChem* **2022,** *15* (15), 202200753.

26. Zhang, J.; Su, D.; Zhang, A.; Wang, D.; Schlögl, R.; Hébert, C., Nanocarbon as Robust Catalyst: Mechanistic Insight into Carbon-Mediated Catalysis. *Angewandte Chemie* **2007,** *119* (38), 7460-7464.

27. Frank, B.; Zhang, J.; Blume, R.; Schlogl, R.; Su, D. S., Heteroatoms Increase the Selectivity in Oxidative Dehydrogenation Reactions on Nanocarbons. *Angew. Chem. Int. Ed. Engl.* **2009,** *48* (37), 6913-7.

28. Wu, J.; Mehmood, A.; Zhang, G.; Wu, S.; Ali, G.; Kucernak, A., Highly Selective O_2 Reduction to H_2O_2 Catalyzed by Cobalt Nanoparticles Supported on Nitrogen-Doped Carbon in Alkaline Solution. *ACS Catal.*, 2021; (11), 5035-5046.

29. Ketchie, W. C.; Murayama, M.; Davis, R. J., Promotional Effect of Hydroxyl on the Aqueous Phase Oxidation of Carbon Monoxide and Glycerol over Supported Au Catalysts. *Top. Catal.* **2007**, (44), 307-317.

30. Li, L.; Ma, X.; Chen, R.; Wang, C.; Lu, M., Nitrogen-Containing Functional Groups-Facilitated Acetone Adsorption by ZIF-8-Derived Porous Carbon. *Materials* **2018,** *11* (1).

31. Yang, F.; Li, W.; Zhang, L.; Tu, W.; Wang, X.; Li, L.; Yu, C.; Gao, Q.; Yuan, A.; Pan, J., Drastically Boosting Volatile Acetone Capture Enabled by N-Doping Activated Carbon: An Interesting Deep Surface Digging Effect. *Sep. Purif. Tech.* **2021,** *276*.

32. Chen, R.; Han, N.; Li, L.; Wang, S.; Ma, X.; Wang, C.; Li, H.; Li, H.; Zeng, L., Fundamental Understanding of Oxygen Content in Activated Carbon on Acetone Adsorption Desorption. *Appl. Surf. Sci.* **2020,** *508*.

33. Liang, X.; Chi, J.; Yang, Z., The Influence of the Functional Group on Activated Carbon for Acetone Adsorption Property by Molecular Simulation Study. *Microporous and Mesoporous Mater.* **2018,** *262*, 77-88.

34. Lin, F.; Wang, H.; Zhao, Y.; Fu, J.; Mei, D.; Jaegers, N. R.; Gao, F.; Wang, Y., Elucidation of Active Sites in Aldol Condensation of Acetone over Single-Facet Dominant Anatase TiO_2 (101) and (001) Catalysts. *JACS Au* **2021,** *1* (1), 41-52.

Chapter 5 Conclusions and Future Work

5.1 Summary of Findings

In this work, catalytic reactions involving O_2 activation were studied on isolated transition metal atoms in nitrogen-doped carbon. As discussed in Chapter 2, an isolated Co-N-C catalyst was synthesized by a modified thermal treatment method with characterization by STEM revealing the isolated nature of the metal in the catalyst. To investigate the activity of isolated Co for a probe reaction involving O_2 activation, CO oxidation was evaluated over a variety of Co catalysts over a range of temperatures. Although Co-N-C catalyzed CO oxidation at temperatures as low as 196 K, the reaction rate decreased with increasing temperature from 273 K to 400 K. Above 400 K, however, the rate increased with temperature as generally expected. The low temperature activity of Co-N-C contrasted with the other supported and bulk Co-containing catalysts, which lacked low temperature activity and followed Arrhenius-type behavior (increasing rate with temperature) throughout the whole temperature range. Investigation of the orders of reaction at low temperatures revealed a significant difference between the Co-N-C catalyst and other Co-containing catalysts. While the other Co catalysts are known to complete CO oxidation via MvK-type mechanisms, it was unclear how the isolated Co-N-C could catalyze CO oxidation via that path. The reaction on the Co-N-C had positive orders for both CO and O_2 which suggests the reactants have low adsorption energies and therefore low coverages on the catalyst. Low coverage was confirmed by SSITKA as less than 10 % of the total Co in the sample was observed to be covered with intermediates leading to product. The high global-rate of low-temperature CO oxidation on Co-N-C was therefore attributed to the high intrinsic TOF.

As discussed in Chapter 2, quantum chemical DFT calculations were used to propose a mechanism of CO oxidation on the Co-N-C catalyst. The DFT calculations were used to predict binding energies of both CO and O_2 on the Co structures coordinated to between 0-4 pyridinic N atoms. An increase in the number of pyridinic N atoms coordinated to Co decreased the binding energies of the reactants to the metal. The Co bound to 4 pyridinic N had the weakest binding energies and was consistent with the weak binding of reactants predicted through the orders of reaction and SSITKA, the coordination number calculated from XAS, and the most common motif proposed in the literature. Ab initio molecular dynamic calculations on this Co-N-C structure led to a mechanistic path for low temperature CO oxidation where the O_2 molecule is activated through a CO-assisted mechanism. In this mechanism, the reductant molecules and the surrounding N-doped carbon support combine to activate O_2 at low temperatures. Calculation on this mechanism with CI-NEB found a transition barrier for O_2 activation of only 16 kJ mol^{-1}. A derived rate expression utilizing the energetics from DFT is consistent with the negative apparent activation energy for CO oxidation as observed experimentally. Interestingly, during the reaction mechanism, the Co ion appeared to maintain a 2+ oxidation state. Since the Co ion did not undergo a redox cycle to facilitate the reaction, it raised questions about whether other transition metals could yield similar low temperature activity through the same mechanism.

As discussed in Chapter 3, quantum chemical DFT calculations were used to screen transition metals for their ability to facilitate the same reductant-assisted O_2 activation reaction with the supporting N-doped carbon. Transition metals close to Co on the periodic table with some prior experimental evidence of synthesis were used in the screening study. The M-N-Cs were screened for three criteria: 1) an exothermic enough binding energy of CO to result in non-negligible coverage, 2) competitive binding of CO to the metal compared to O_2 to prevent O_2

saturation, and 3) ability to form stable CO-O_2 complexes. Inspection of the binding energies of CO on the metals revealed that Ni, Pd, Pt, Cu, Au, Zn, and Ga would not have appreciable amounts of CO on the surface. Application of the second criteria indicates Cd, Cr, and Mn would be covered in O_2 at low temperatures. This left the group 8 and group 9 transition metals and geometry optimizations of the CO-O_2 complex on these atoms revealed that only the group 9 transition metals can form the CO-O_2 complex. The transition metals in the same column as Co (i.e., Rh and Ir) thus fit all three criteria similar to the Co-N-C. Further investigation of Rh-N-C using CI-NEB studies revealed that a CO-assisted mechanism for O_2 activation was similar to the mechanism proposed in Chapter 2 for Co-N-C and resulted in a small barrier (20 kJ mol^{-1}). Thus, it was hypothesized that the Rh-N-C catalyst could be active at low temperatures.

A Rh-N-C catalyst was synthesized by a modified thermal treatment method and characterized by STEM where both isolated Rh and nanoparticles were observed. To understand if the isolated Rh ions were active during low temperatures CO oxidation, the reaction rate and kinetic parameters were compared for various Rh-containing catalysts. The Rh-N-C catalyst was active at temperatures as low as 196 K, with rates that were fairly independent of temperature until 365 K after which the rates increased with temperature. Conversely, the other Rh-containing catalysts did not catalyze CO oxidation at low temperatures (< 400 K). Evaluation of the orders of reaction for each catalyst showed a difference between the isolated Rh-N-C catalyst and the other Rh-containing catalysts. The Rh-N-C catalyst had positive order behavior in both CO and O_2 at lower temperatures, contrasting with the negative order seen for the Rh nanoparticle catalysts that are known to be inhibited by CO. The reaction order in CO on the Rh-N-C catalyst at higher temperatures was ~ 0 and indicated that the reaction rate may be a convolution of both the isolated Rh sites and Rh nanoparticles that were observed with STEM. Calculation of the apparent

activation energy using the observed reaction orders, the binding energies from DFT, and the calculated transition state barrier for O_2 activation resulted in a negligible apparent activation energy, consistent with experiments in the low temperature regime. While the low temperature regime for CO oxidation on transition metal catalysts is consistent with the proposed mechanism, the high temperature regimes for both this Rh-N-C system and the Co-N-C in Chapter 2 were unexplained by the mechanism, prompting the work in Chapter 4.

In Chapter 4, the same Co-N-C catalyst that was used and characterized in Chapter 2 was probed for its activity in the oxidative dehydrogenation of 2-propanol. The gas-phase oxidative dehydrogenation of 2-propanol was chosen as a probe reaction since prior work on the liquid-phase oxidative dehydrogenation of primary alcohols was complicated by solvents and the production of acid which deactivated the catalyst. The Co-N-C catalyst had high initial activity for the gas phase oxidative dehydrogenation of 2-propanol but severely deactivated over several hours to a steady-state rate that is similar to the rate of the metal-free N-C. This deactivation to a similar rate for both the Co-N-C and the N-C catalyst indicates that the Co sites may not be turning over. The similarity between the steady-state Co-N-C and N-C is further confirmed by the similar positive order in alcohol and negative order in O_2. To understand the deactivation of the Co, various co-feeds were run during the reaction. While CO, H_2O, and CO_2 did not affect the rate, NH_3 eliminated the reaction, and upon it being switched off, the steady-state activity returned. Interestingly, DFT calculations on the binding energy of NH_3 to the metal center found that it would bind weaker to the Co ions than CO discussed in Chapter 2. The inhibition by NH_3 and not CO indicates that the reaction may not proceed over the Co ion or involves a deactivation mechanism more complicated than simple competitive adsorption. Further work is needed to explain why the reaction was severely, but reversibly, inhibited by NH_3.

To further probe the effect of solvent on the catalytic performance of the Co-N-C catalyst, the oxidative dehydrogenation of 2-propanol was also performed in liquid water. The Co-N-C catalyst had high initial activity that deactivated after times shorter than 15 min. After the 15 min timepoint, the conversion did not change appreciably up to 90 min. While deactivation for these catalysts has been previously seen in liquid water with primary alcohols forming acid products, it was unclear why the catalyst would deactivate without acid formation. Further, these reactions resulted in only ~ 80 % carbon recovery. To investigate the loss of carbon and to understand deactivation, ketone was added to the reaction. Upon addition of 0.1 M of a slightly larger ketone (2-butanone), the reaction was inhibited and the carbon balance for 2-propanol and 2-propanone was improved. Evidently, ketone appears to be detrimental to the activity of the Co-N-C catalyst during oxidative dehydrogenation of 2-propanol. Further, the metal-free N-C appeared to be inactive but suffered from carbon balance problems. Thus, it is possible that there is again a highly active site involving the Co that ultimately is deactivated quickly.

The results in this dissertation present a mechanism for the activation of O_2 on Co-N-C and Rh-N-C at low temperatures. The weak binding of adsorbates on the surface with the reductant molecule assisting the activation of O_2 with the carbon support provided a small transition barrier path. While the high temperature activity was inconsistent with the model, results for the oxidative dehydrogenation of 2-propanol on Co-N-C suggest that the N-C may play a more significant role at these higher temperatures. The findings in this dissertation will facilitate further design of M-N-C catalysts and provide a guide for mechanistic studies of O_2 activation in other reactions involving M-N-C catalysts.

5.2 Future Work

5.2.1 Investigation of High Initial Activity for both the Oxidative Dehydrogenation of 2-propanol and CO Oxidation over Co-N-C

The work in this dissertation has focused on the steady-state activity of the M-N-C catalysts for O_2 activation but there is evidently a highly active species that deactivates over several hours for the both the Co-N-C and Rh-N-C catalysts during the CO oxidation reaction and for Co-N-C during the oxidative dehydrogenation of 2-propanol. As discussed in Chapter 4, the Co-N-C catalyst had high initial activity for the oxidative dehydrogenation of 2-propanol in the gas phase that decreased to a steady-state rate that was similar to the metal-free N-C. Similar deactivation was seen for the Co-N-C and Rh-N-C catalyst for low temperature CO oxidation. Interestingly, there is a difference in the deactivation between the 2-propanol and CO reactions. During the CO oxidation reaction, the steady-state rate was not accounted for by the N-C. Various pretreatment flows were used to probe deactivation during CO oxidation and are presented in Fig. 5.1. It appears that each of the pretreatments resulted in deactivation from the untreated Co-N-C case. It is unclear if the deactivation is due to impurities in the gases or if the co-feeds are inhibiting the reaction. A regeneration in He at 673 K for 2 h can, however, recover the deactivated portion of the initial conversion suggesting that it is not a problem with catalyst stability. When investigating the stability of the Co-N-C catalyst during XAS by flowing CO or H_2 at high temperature (673 K) (Chapter 2 Fig. 2.5) there was no change of coordination, indicating that the Co ions appear to be stable during the reaction at least under reductive conditions.[1] Although in Chapter 2 the majority species found through EXAFS fitting was coordinated to 4 N atoms, there could minority sites that are more active but are difficult to probe spectroscopically. It is proposed that future work attempts

to synthesize other metal coordination motifs with N-C and investigate these structures to understand if they are contributing to the high initial activity.

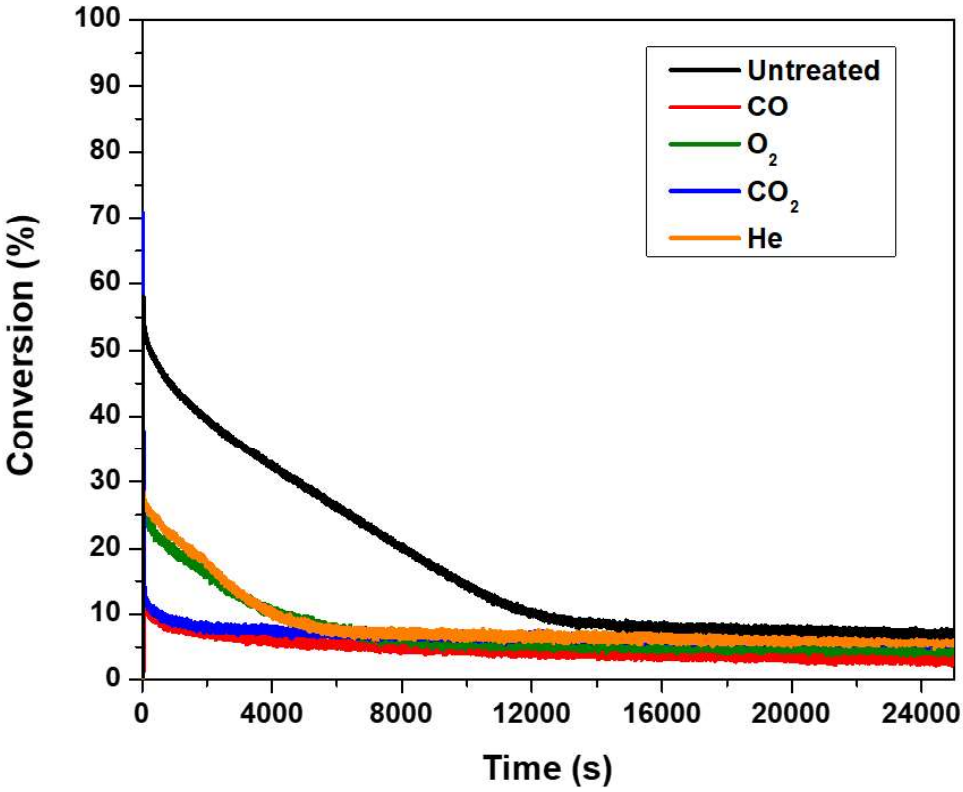

Figure 5.1. Conversion of CO over time. Each reaction was a fresh reaction run with 0.01 g of Co-N-C diluted in 0.25 g SiC.
A thermal treatment of the catalyst at 673 K in He was done before each reaction run. The reactor was subsequently cooled to 273 K and pretreated in flowing gas, pure He or 1 % co-feed in He. All co-feeds were purified with either a silica trap in a dry-ice acetone bath or an OMI indicator filter. The pretreatment was run for 8 h before turning on the reaction gas flows (160 cm^3 min^{-1} total flow with 1 % CO, 1 % O_2, 1 % Ar, and balance He) at 3 atm.

5.2.2 Calculations of Binding Energy for Reactants and a Mechanistic Study on Various Densities of Transition Metal Ions

In Chapter 3, the binding energies for CO and O_2 on various transition metal ions depended on the metal density in the repeated supercell. It is hypothesized that the stability of the transition metal in the N-C structure may change based on the metal density, which could cause a change in the binding energy. For example, Co bound to 4N is known to be stable and thus did not change significantly with metal density.[2] Conversely, when investigating less stable Rh-N-C catalyst, the binding energy did increase for CO on Rh coordinated to 4 N which is less stable than the Co analog (-68 versus -54 kJ mol^{-1} for CO binding to higher and lower density Rh respectively).[2] Evidently, the binding energy may be affected by the presence of other transition metals nearby to the covered M ion. The metal density could also affect the rigidity of the carbon support. The mechanism for O_2 activation proposed in Chapters 2 and 3 requires some movement of the carbon support atoms, which may become more difficult with less metal density. Beyond the carbon support itself, the supercells studied in this dissertation are on planar sheets with 15 Å of vacuum on both sides but other structures such as hollow tubes or supported planar sheets could alter the stability of the M ion and affect binding energies.[3, 4] Thus, although spectroscopic analysis often suggests that the most common motif of M-N-C is a transition metal bound to 4 pyridinic N, the environment surrounding the transition metal ion could greatly affect the activity of the site. These considerations could be explored computationally and would be useful in understanding if there are better motifs for O_2 activation.

5.2.3 Investigation of the Metal Free N-C Catalyst for O_2 Activation

As discussed in Chapter 4, the N-C is active for the oxidative dehydrogenation of 2-propanol. The N-C has been speculated to be active for O_2 activation reactions for many years now but is often overlooked as earth-abundant M-N-C catalysts are typically reported to have higher activities. Even if catalysts are active with transition metals, it is important to further study the metal-free N-C for activity since a significant portion of the M-N-C activity may be related to the N-C. Determination of the N species (i.e., pyridinic, pyrrolic, or graphitic) responsible for the activity during the oxidative dehydrogenation of 2-propanol would be essential for further development of metal-free catalysts for O_2 activation reactions involving alcohols. Previously, the N speciation has been investigated by XPS and a similar study could be done for this catalyst system.[5] Further computational DFT should be used to find a reaction mechanism since mechanisms for O_2 activation on these catalysts without an applied potential have not been extensively explored. Titrating sites using inhibitors like NH_3 in the gas phase or ketone in the liquid phase could assist in the quantification of the active sites. The co-feeding of NH_3 during the gas-phase oxidative dehydrogenation of 2-propanol caused complete inhibition of the Co-N-C, apparently deactivating the N-C steady-state activity as well. Computational calculations in Chapter 4 could not account for the coverage of either the Co ion or the surrounding carbon support and thus further work should investigate the reason NH_3 caused deactivation.

5.3 References

1. Whitcomb, C. A.; Sviripa, A.; Schapowal, M. I.; Mamedov, K.; Unocic, R. R.; Paolucci, C.; Davis, R. J., Mechanistic Insights on the Low-Temperature Oxidation of CO Catalyzed by Isolated Co Ions in N-Doped Carbon. *ACS Catalysis* **2022,** *12* (24), 15529-15540.

2. Kropp, T.; Mavrikakis, M., Transition Metal Atoms Embedded in Graphene: How Nitrogen Doping Increases CO Oxidation Activity. *ACS Catal.* **2019**, (9), 6864-6868.

3. Gerber, I. C.; Serp, P., A Theory/Experience Description of Support Effects in Carbon-Supported Catalysts. *Chem. Rev.* **2020**, (120), 1250-1349.

4. Maibam, A.; Govindaraja, T.; Selvaraj, K.; Krishnamurty, S., Dinitrogen Activation on Graphene Anchored Single Atom Catalysts: Local Site Activity or Surface Phenomena. *J. Phys. Chem. C*, **2019** *123* (45), 27492-27500.

5. Lu, X.; He, J.; Huang, L.; Qin, J.; Ma, Y.; Liu, X.; Zhao, W.; Liu, B.; Zhang, Z., Synergetic Roles of Pyridinic Nitrogen and Carbonyl Sites in Nitrogen-Doped Carbon for the Metal-Free Transfer Hydrogenation Reactions. *Appl. Catal. B: Environ.* **2023,** *324*.

Appendix A Additional Information for Chapter 2: Mechanistic Insights on the Low-Temperature Oxidation of CO Catalyzed by Isolated Co Ions in N-Doped Carbon

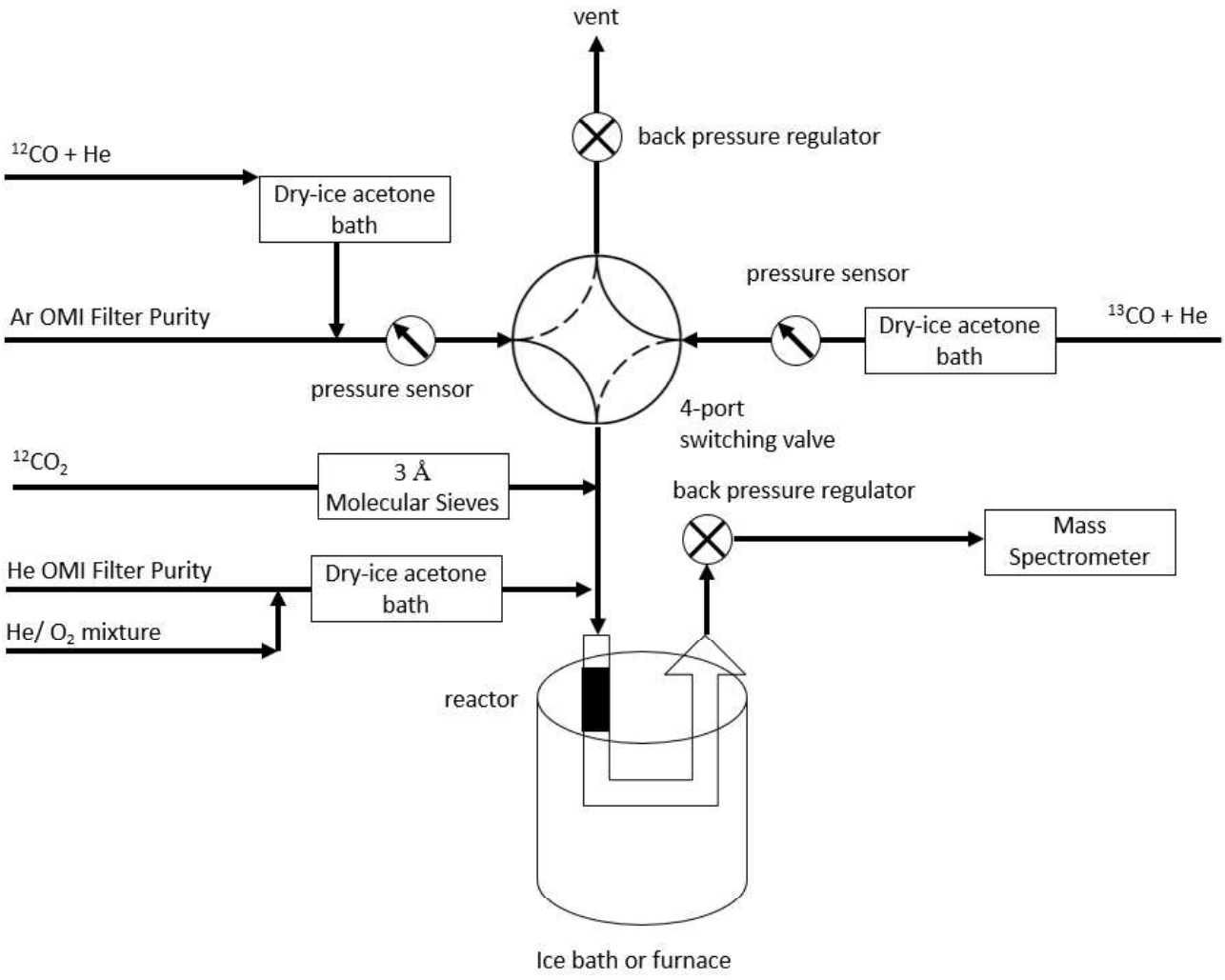

Appendix Fig. A1. Setup of the reactor system for both steady state reactions and steady-state isotopic transient kinetic analysis (SSITKA).
All gases were purified prior to the reactor. Silica traps in dry-ice acetone were placed on the CO lines to remove trace water and carbonyls that may be present in the cylinders and lines. The CO_2 line was purified with 3 Å molecular sieves. Backpressure regulators were used to control the pressure in both lines when doing the SSITKA experiments.

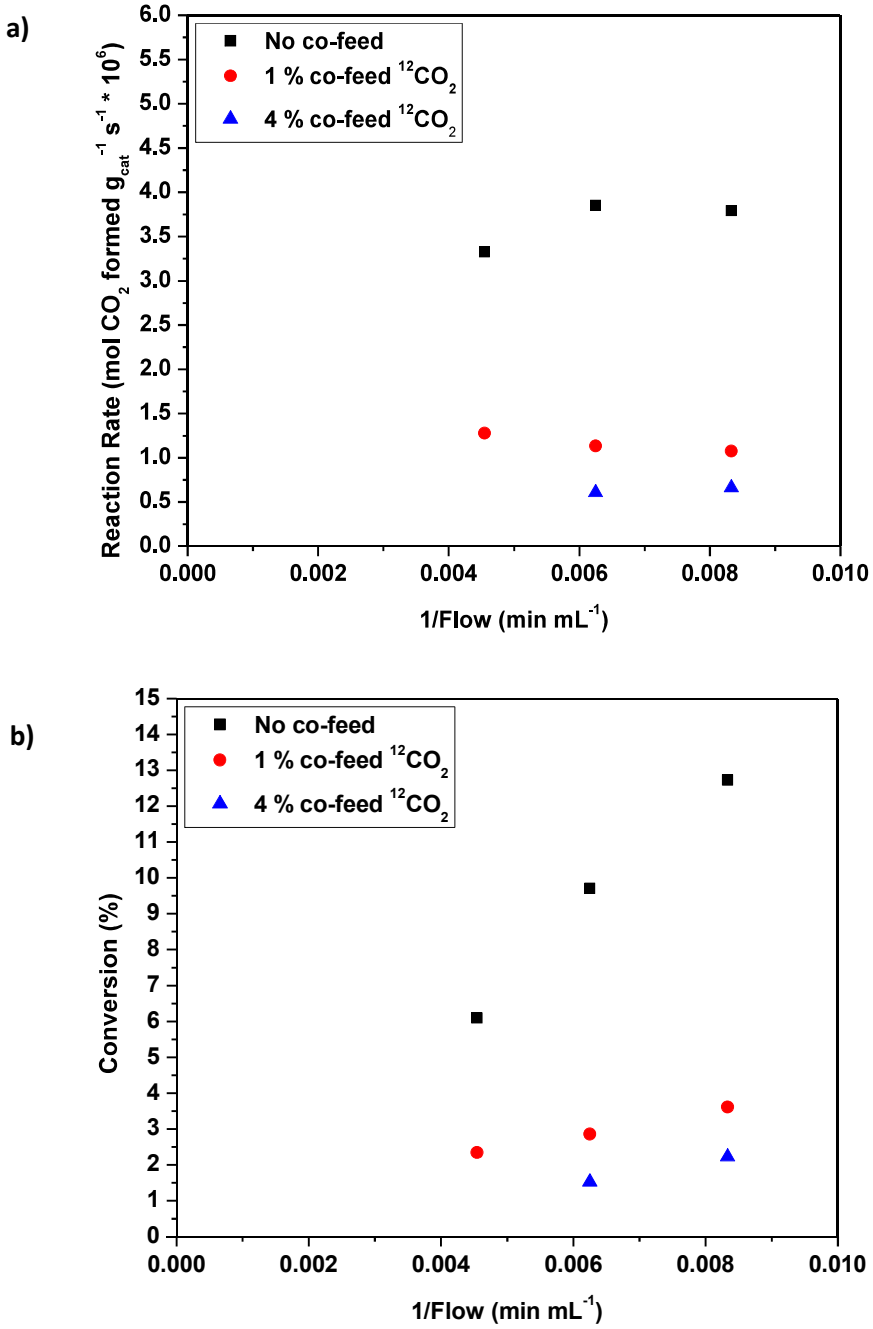

Appendix Fig. A2. The effect of flow rate on the reaction rate and conversion during SSITKA. Results from experiments without cofed CO_2 were averaged over 3 switches back and forth from labeled and unlabeled CO, utilizing signals from $^{12}CO_2$ and $^{13}CO_2$. Results from experiments with cofed $^{12}CO_2$ were analyzed from the $^{13}CO_2$ signal only since there was excess $^{12}CO_2$.

Appendix Table A1. Effect of cell size and number of Co on vdW-DF computed binding energies of CO and O_2.

Binding Energy (kJ mol^{-1})	8.5 x 9.8 Å Cell, One Co	17 x 10 Å Cell, Two Co	17 x 20 Å Cell, One Co
CO	-57	-60	-54
O_2	-73	-73	-78

Appendix Table A2. Tabulated CO oxidation gas phase reaction energies by functional.

Functional	Experimental NIST[a]	PBE-D3	RPBE	BEEF	SCAN	HSE06	vdW-DF	vdW-DF2
Gas Phase Reaction Energy (kJ mol^{-1})	-566	-630	-590	-584	-610	-615	-563	-560

a) The NIST value was calculated from https://webbook.nist.gov/

Appendix Table A3. Binding energy dependence on functional for $CoN_{(0-4)}$ structures.

Structure	PBE-D3 (kJ mol^{-1})		RPBE (kJ mol^{-1})		BEEF (kJ mol^{-1})		SCAN (kJ mol^{-1})		vdW-DF (kJ mol^{-1})		vdW-DF2 (kJ mol^{-1})	
	CO	O_2	CO	O_2	CO	O_2	CO	O_2	CO	O_2	CO	O_2
N0	-182	-157	-144	-122	-146	-132	-155	-92	-153	-159	-145	-172
N1	-210	-160	-167	-122	-166	-128	-146	-58	-164	-148	-149	-156
N2	-177	-112	-135	-76	-136	-89	-145	-73	-133	-104	-120	-112
N3	-163	-86	-126	-50	-123	-67	-122	-58	-122	-80	-111	-88
N4	-92	-73	-56	-57	-58	-58	-67	-60	-57	-73	-50	-82

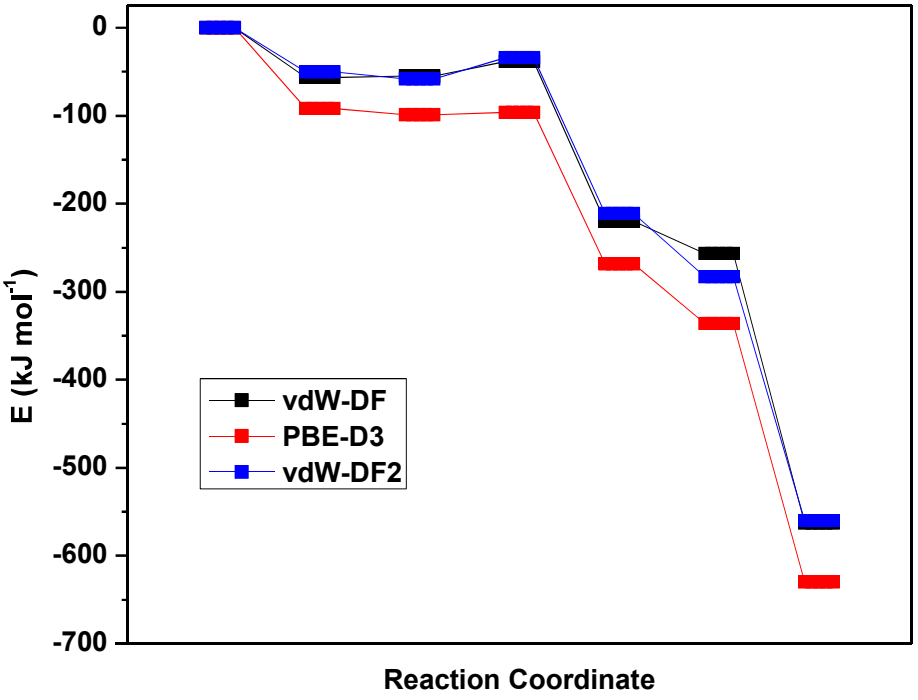

Appendix Fig. A3. Comparison of potential energy diagrams for the oxidation of CO over Co-N-C with three different functionals.

The reported vdW-DF diagram from the main text is compared to the often-used PBE-D3 functional as well as another version of the van der Waals functional (vdW-DF2).[1]

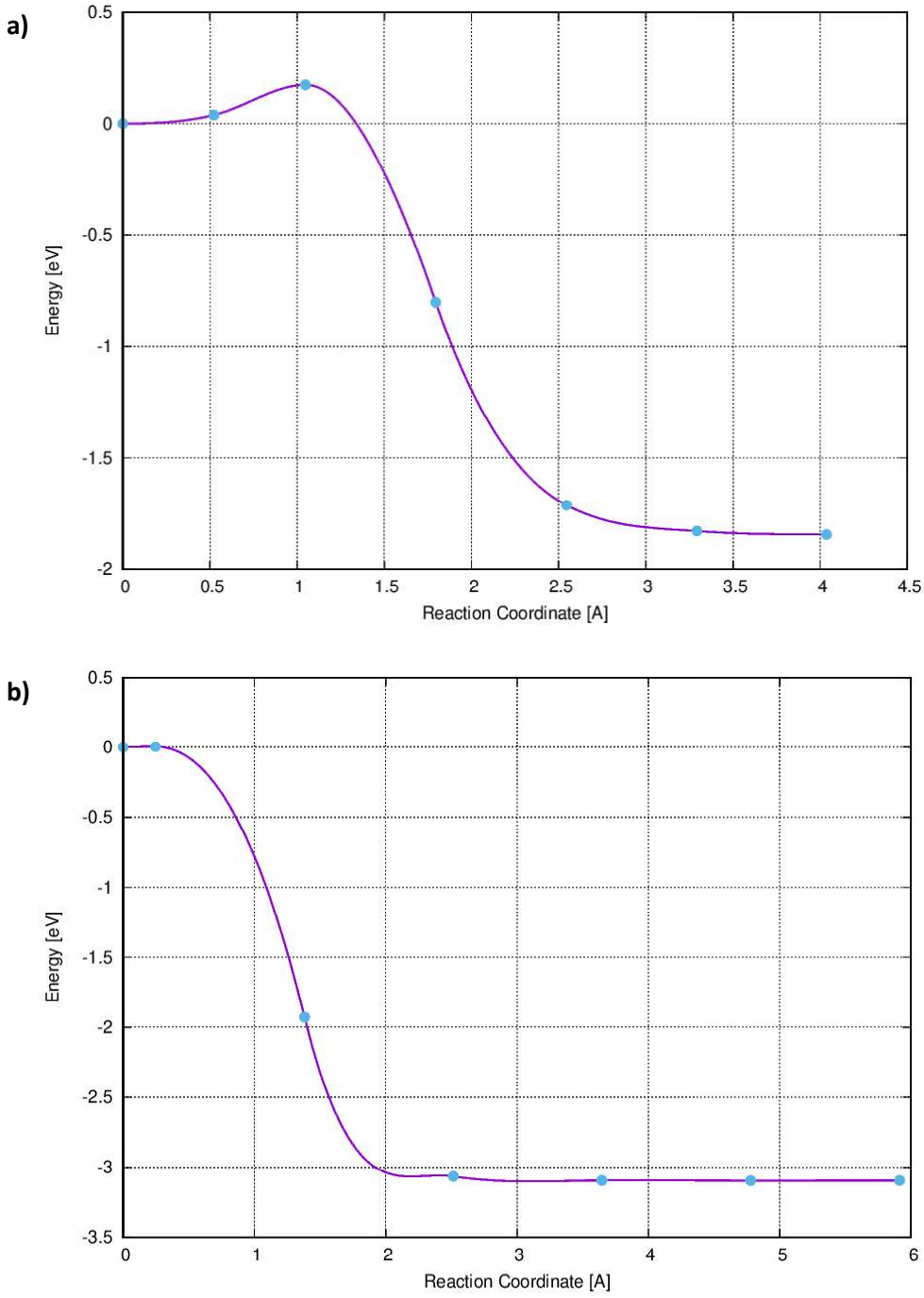

Appendix Fig. A4. Climbing image nudged elastic band calculations for TS1 and TS2.
a) The CI-NEB for TS1 in the reaction path calculated with vdW-DF. b) The CI-NEB for TS2 in the reaction path calculated with vdW-DF.

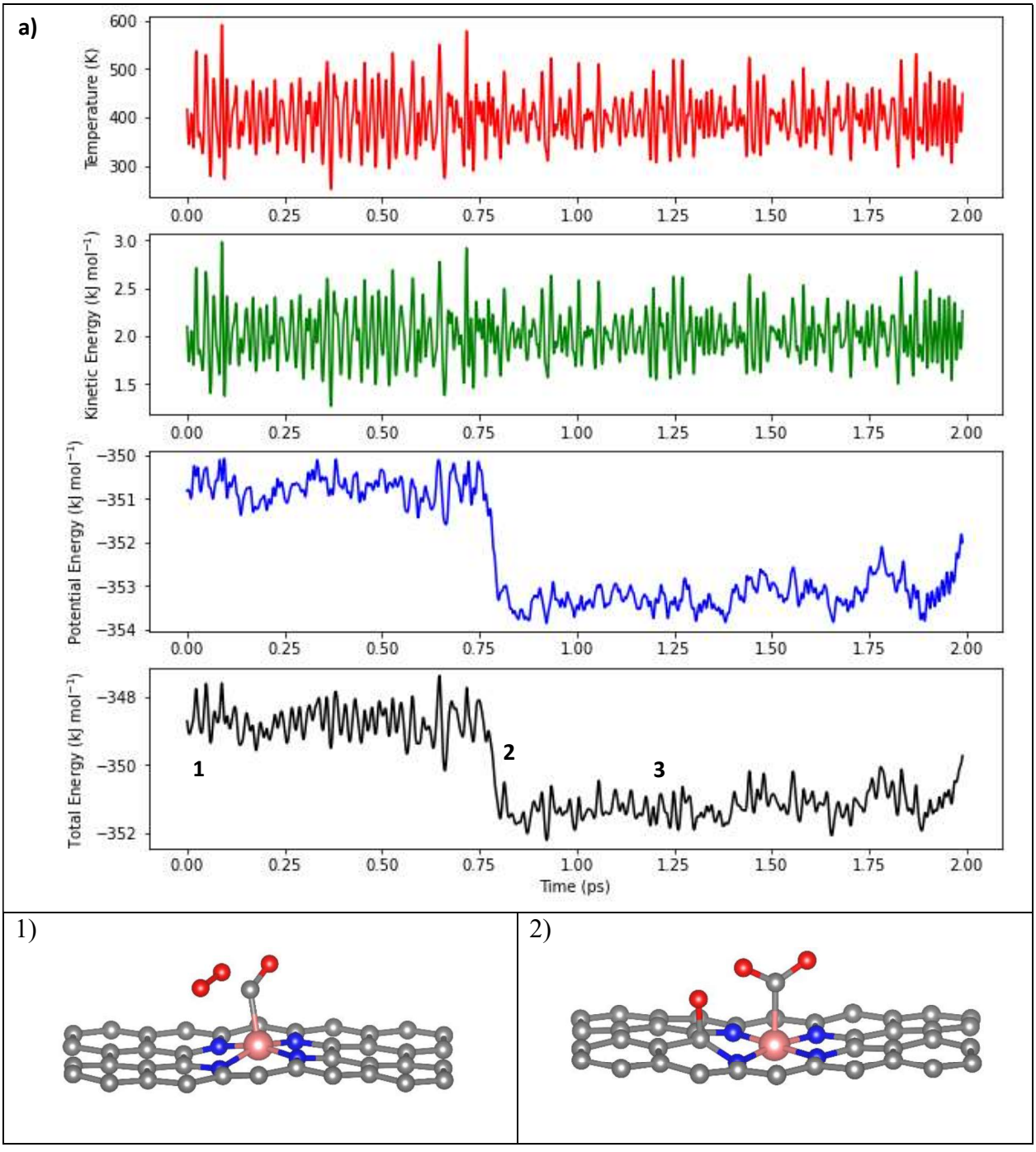
a)
Temperature (K)
Kinetic Energy (kJ mol⁻¹)
Potential Energy (kJ mol⁻¹)
Total Energy (kJ mol⁻¹)
Time (ps)
1
2
3
1)
2)

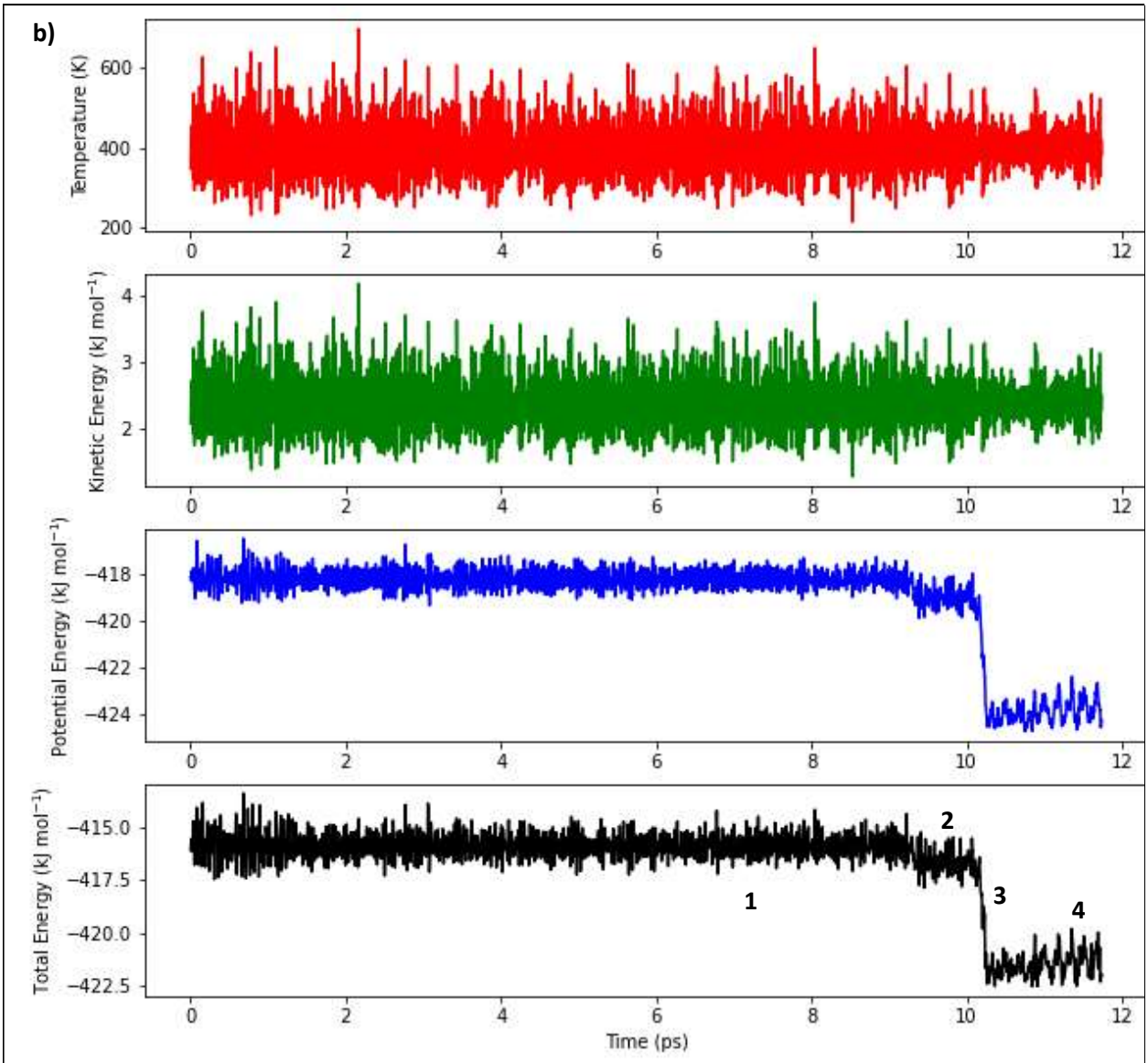
b)
Temperature (K)
Kinetic Energy (kJ mol⁻¹)
Potential Energy (kJ mol⁻¹)
Total Energy (kJ mol⁻¹)
Time (ps)
1
2
3
4

1)

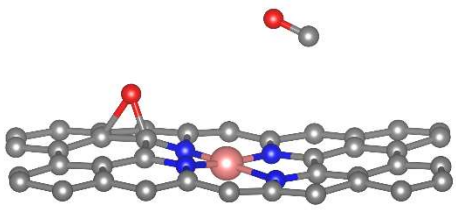

2)

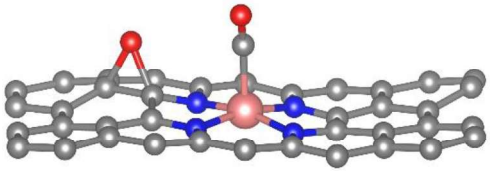

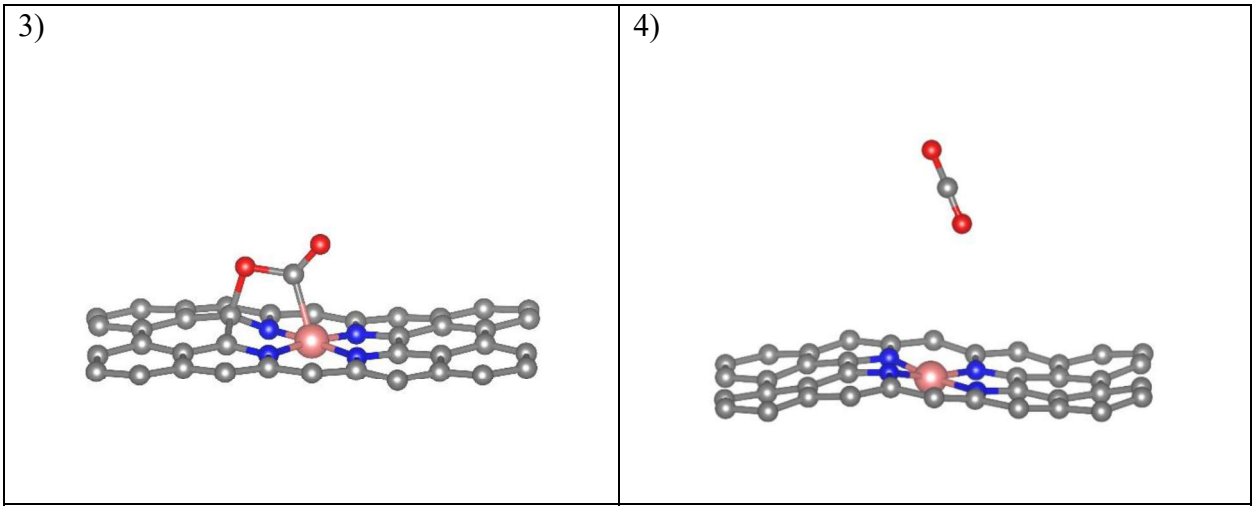

Appendix Fig. A5. Temperature, kinetic, potential, total free energies, and structural snapshots during 398 K NVT ab initio molecular dynamics simulations.

a) One CO and one O_2 molecule were added to the vacuum above the structure and weakly interact with each other as shown in image 1. Image 2 is during the transition state and the large drop in total energy occurs when CO_2 is formed. Image 3 is when the CO_2 desorbs and leaves behind a structure with O* that is then used in part b. b) One CO is added to the structure from the first AIMD simulation while the product CO_2 is removed, resulting in image 1. In image 2, the CO molecule binds to the Co sites before interacting with O* in image 3 during the large drop in total energy. Image 4 is after CO_2 desorbs and turns over the catalyst. Trajectory files attached in other supplemental materials.

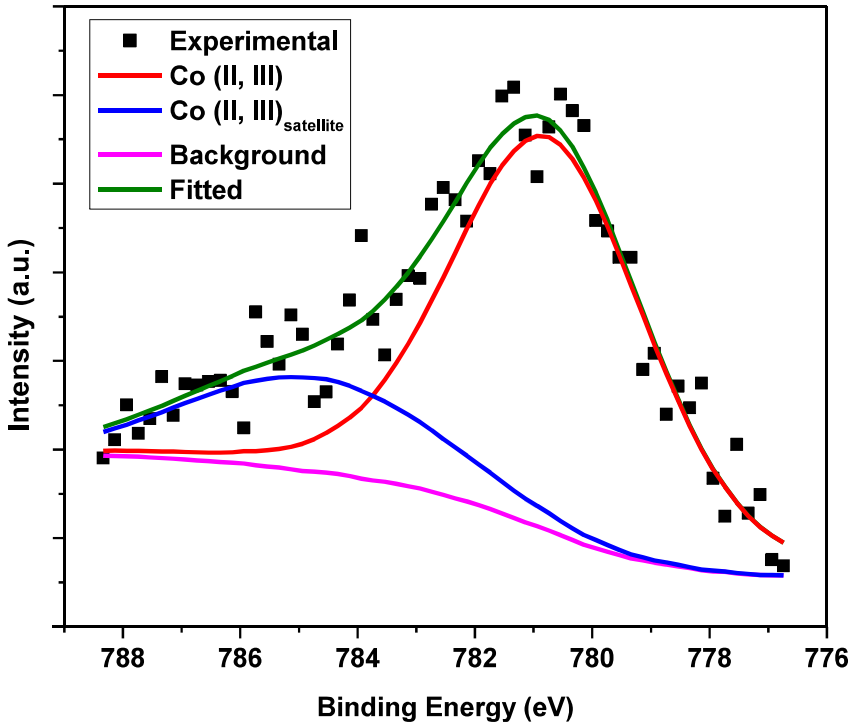

Appendix Fig. A6. X-ray photoelectron spectrum of the Co $2p_{3/2}$ region.
The presence of the satellite peak at ~785.9 eV with a major peak at ~780.9 eV is consistent with a Co^{2+} oxidation state.

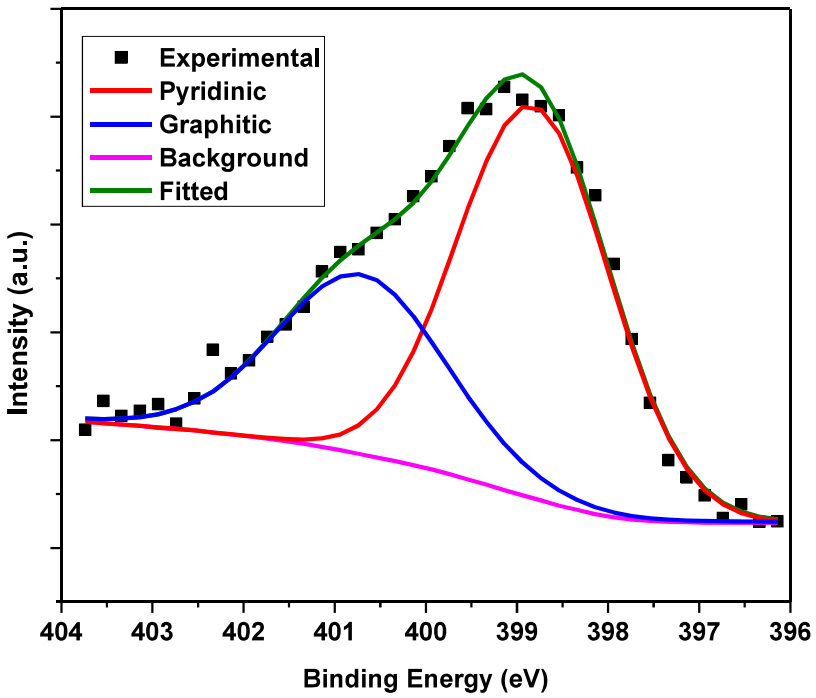

Appendix Fig. A7. X-ray photoelectron spectrum of the N 1 s region.
The two major peaks at 399.0 eV and 401.0 eV are indicative of N bound in a pyridinic and graphitic mode, respectively. The pyridinic peak is often assigned to the N coordinated to the transition metal ion.

Appendix Table A4. Core level binding energies and compositions determined from XPS. [a]

Sample	Area	Binding energies (eV)			Relative amount (mol %)				
		Co	N_I[b]	N_{II}[c]	Co	N_I[b]	N_{II}[c]	O	C
Co-N-C	1	781.1	398.9	400.8	0.24	2.3	1.4	2.7	93
	2	781.2	399.0	401.1	0.22	2.3	0.8	5.1	92
	3	780.9	399.0	401.1	0.28	3.0	1.1	3.3	92
	Avg	-	-	-	0.25	2.5	1.1	3.7	92
	σ	-	-	-	0.02	0.3	0.2	1	0.5

a) The Co $2p_{3/2}$ and N 1s spectra are presented in Figs. A6 and A7 respectively.
b) The N_I peak at ~399.0 eV was assigned to pyridinic N.
c) The N_{II} peak at ~401.0 eV was assigned to graphitic N.

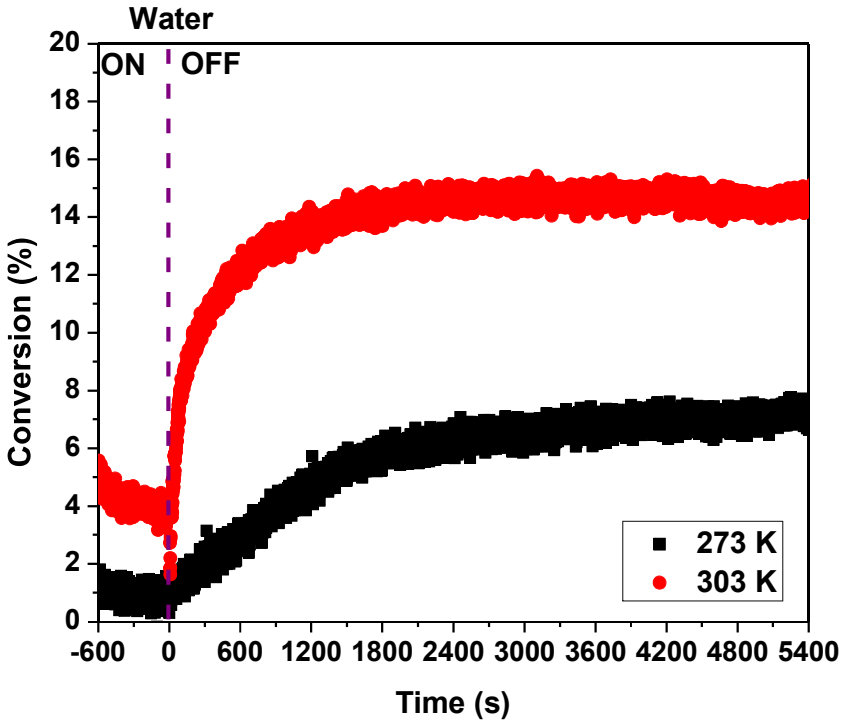

Appendix Fig. A8. The influence of co-fed water on the oxidation of CO over Co-N-C catalyst (prior to acid treatment).

The reaction was performed with 160 cm^3 min^{-1} total flow at 3 atm, 1 % CO, 1 % O_2, 1 % Ar, and balance He with 10 mg of catalyst. The balance He was adjusted to maintain a constant total flow rate in the presence or absence of 0.05 vol % water provided by a water saturator. The O_2 and CO were purified with silica traps in a dry-ice acetone bath while the He and Ar lines were purified with an OMI Filter.

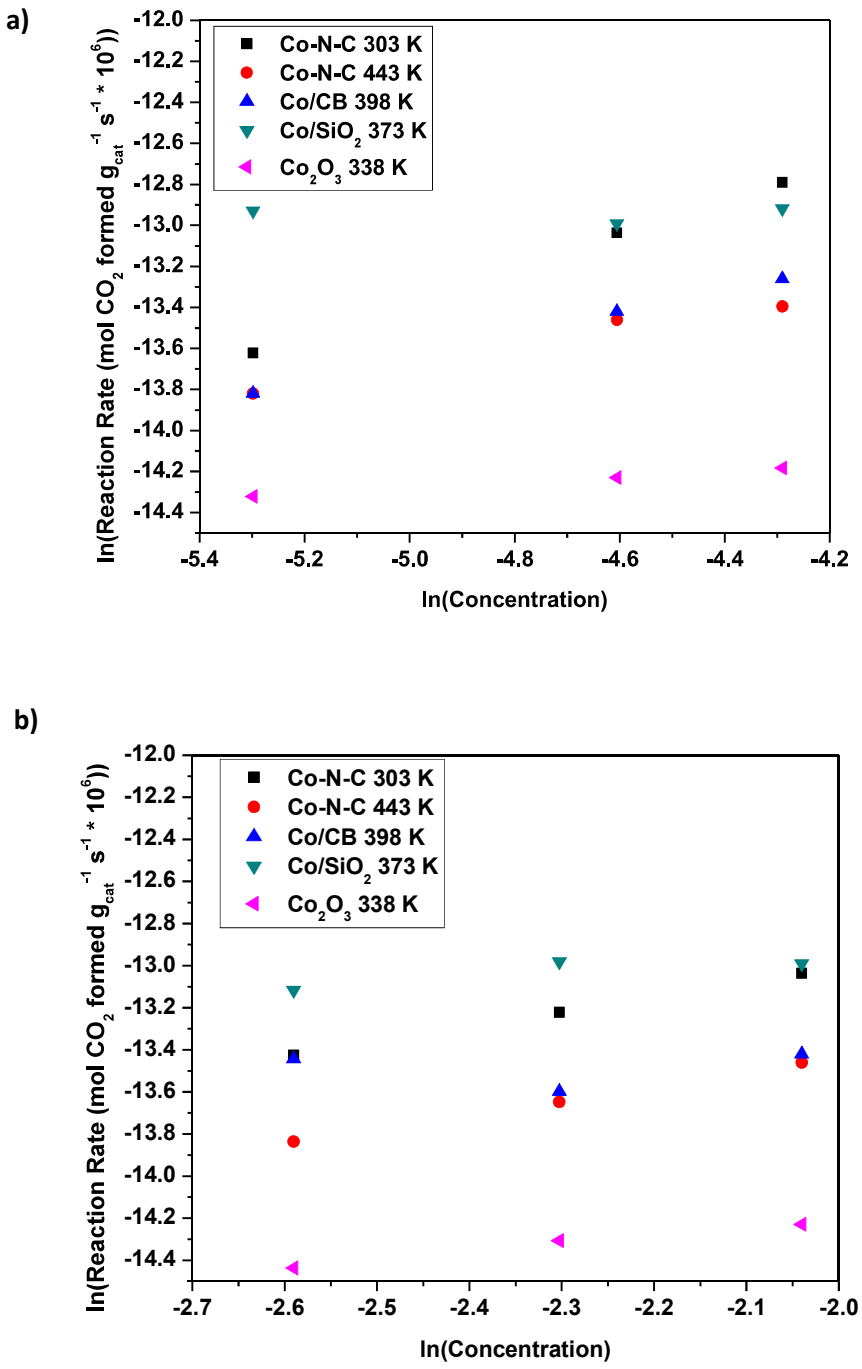

Appendix Fig. A9. Reaction order plots for both reactants on various Co-containing catalysts. a) Plot of the effect of the concentration (mol %) of CO on the reaction rate for various Co containing catalysts while holding the partial pressure (from 1.5 to 4.5 kPa) of O_2 constant at 1 %. b) Plot of the effect of the concentration of O_2 on the reaction rate for various Co containing catalysts while holding the partial pressure (from 1.5 to 4.5 kPa) of CO constant at 1 %. The temperatures were adjusted to remain under differential conditions.

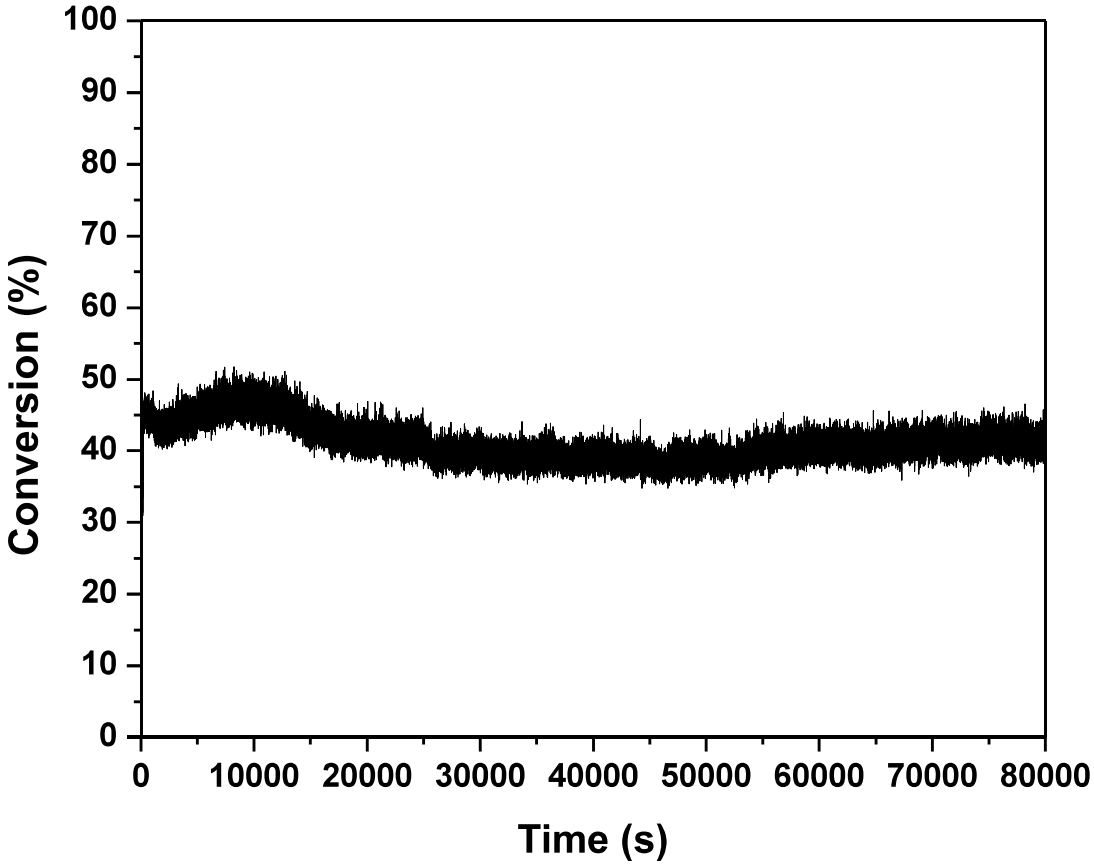

Appendix Fig. A10. Activity of the single atom Co-N-C catalyst for CO oxidation at dry-ice acetone temperatures (196 K).

The reaction was run with 160 cm^3 total flow, 1 % CO, 1 % O_2, 1 % Ar, and balance He at 3 atm and with 30 mg of catalyst. The O_2 and CO lines were purified with silica traps in a dry-ice acetone bath while the He and Ar lines were purified with an OMI Filter. Even with low loadings of catalyst and low gas phase concentrations of reactants, differential conditions were not able to be reached.

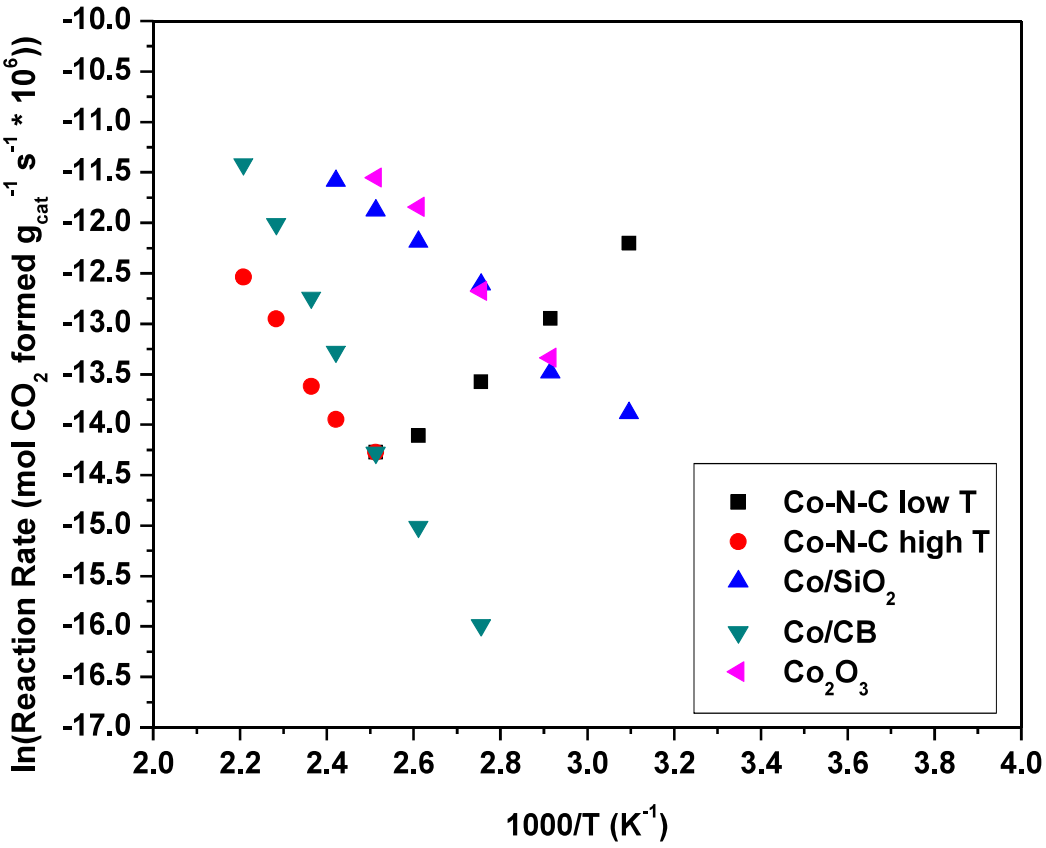

Appendix Fig. A11. Arrhenius-type plots for the CO oxidation reaction on various Co-containing catalysts.

The reaction was run with 100 mg of Co-N-C diluted in SiC and with 160 cm^3 total flow, 1 % CO, 13 % O_2, 1 % Ar, and balance He at 3 atm. The O_2 and CO lines were purified with silica traps in a dry-ice acetone bath while the He and Ar lines were purified with an OMI Filter. All points were collected once steady state was reached at each temperature. Points were collected at alternating high and low temperatures.

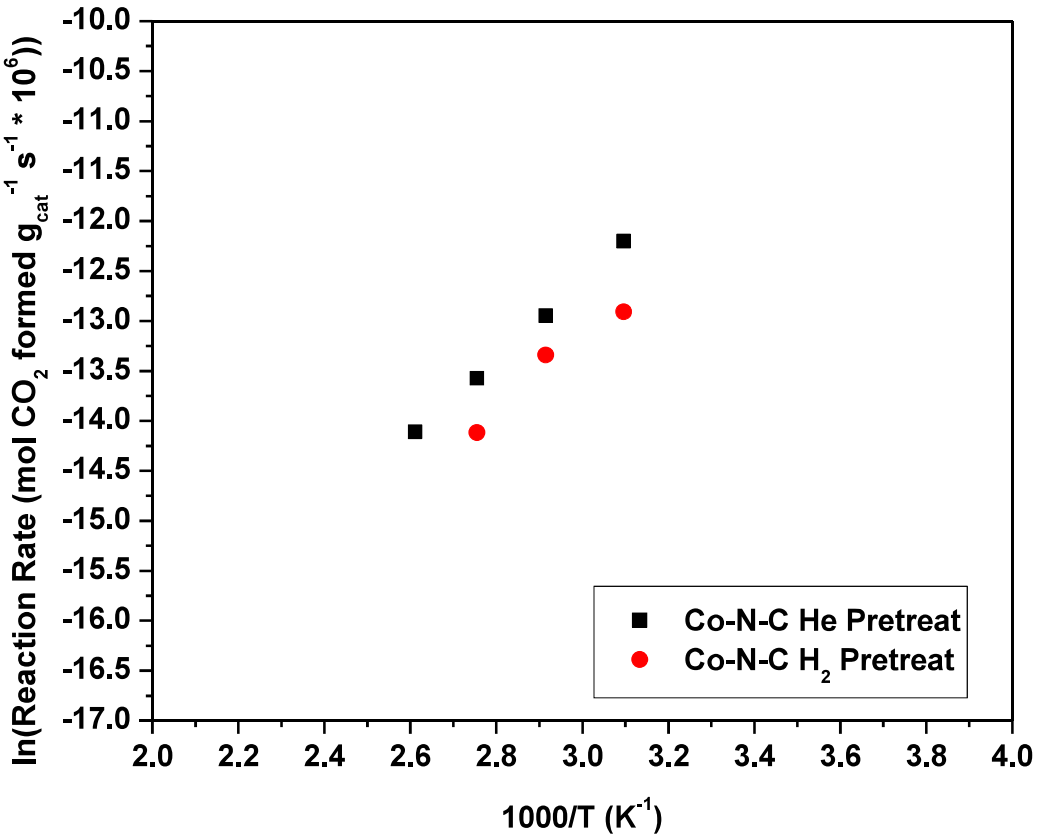

Appendix Fig. A12. Arrhenius-type plot for the low temperature regime of the CO oxidation reaction on Co-N-C after various high temperature pre-treatments.
Pretreatments were done on the same loaded catalyst without removal. Each pretreatment was run at 673 K under pure flow of He or 5 % H_2/Ar. The reaction was run with 100 mg of Co-N-C diluted in SiC and with 160 cm^3 total flow, 1 % CO, 13 % O_2, 1 % Ar, and balance He at 3 atm. The O_2 and CO lines were purified with silica traps in a dry-ice acetone bath while the He and Ar lines were purified with an OMI Filter.

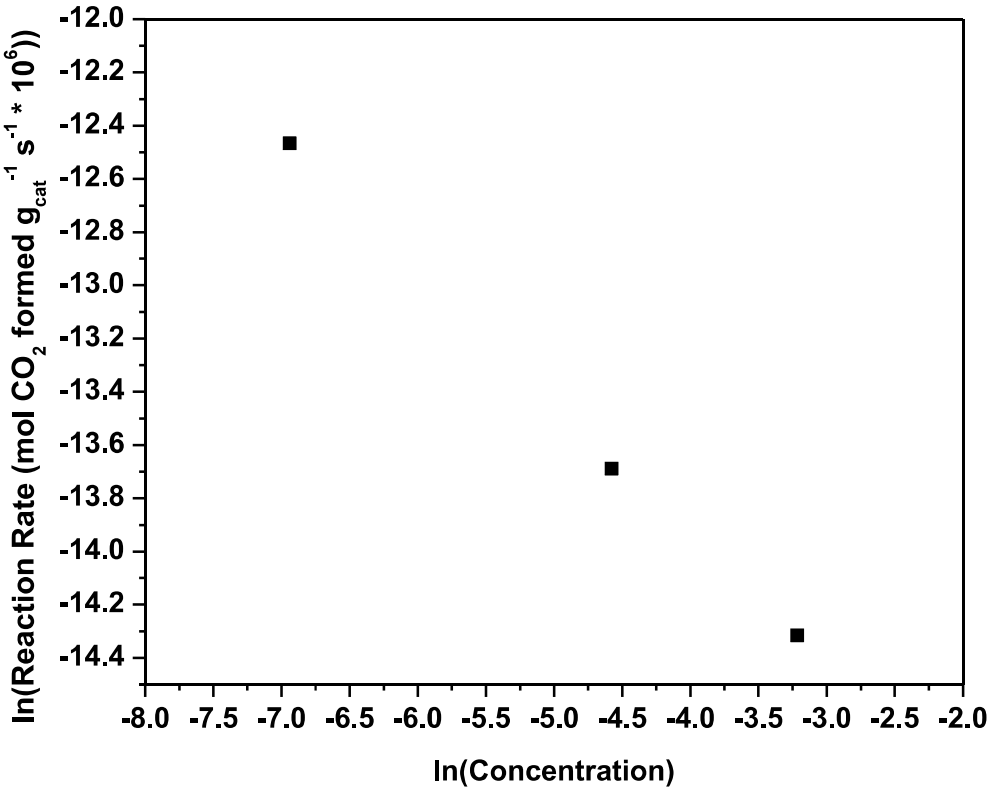

Appendix Fig. A13. Reaction order plots for CO_2 on the Co-N-C catalyst.
The points were collected during the SSITKA experiment as each co-fed level of $^{12}CO_2$ while keeping the partial pressure of CO and O_2 constant. The points were taken during the 160 cm^3 min^{-1} flow rate and 3 atm (He:CO:O_2:Ar = 85:1:1:1). The reaction rates were determined by the conversion of ^{13}CO to $^{13}CO_2$.

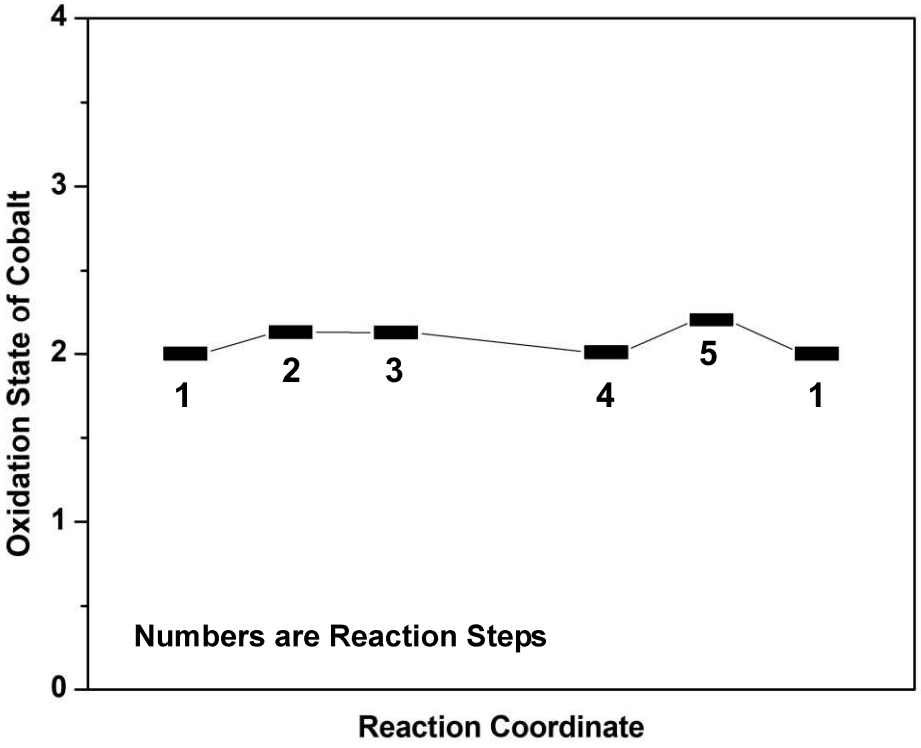

Appendix Fig. A14. Bader charges plotted over the course of the reaction coordinate in Fig. 2.8. Bader charges were computed using the method developed by Henkelman et al.[2, 3] The charges were referenced to a linear interpolation between the charge of the known 2+ state of the bare Co-N-C catalyst and a $Co^{3+}F_3$ structure from the Materials Project database (mp-561038).[4] The $Co^{3+}F_3$ has a triagonal R3c space group crystal structure.

References

1. Lee, K.; Murray, É. D.; Kong, L.; Lundqvist, B. I.; Langreth, D. C., Higher-Accuracy van der Waals Density Functional. *Phys. Rev. B* **2010,** *82*, 3-6.

2. Henkelman, G.; Uberuaga, B. P.; Josson, H., A Climbing Image Nudged Elastic Band Method for Finding Saddle Points and Minimum Energy Paths and Minimum Energy Paths. *J.Chem. Phys.* **2000,** *113*.

3. Henkelman, G.; Josson, H., Improved Tangent Estimate in the Nudged Elastic Band Method for Finding Minimum Energy Paths and Saddle Points. *J. Chem. Phys.* **2000,** *133*.

4. Jain, A.; Ong, S. P.; Hautier, G.; Chen, W.; Richards, W. D.; Dacek, S.; Cholia, S.; Gunter, D.; Skinner, D.; Ceder, G.; Persson, K. A., Commentary: The Materials Project: A Materials Genome Approach to Accelerating Materials Innovation. *APL Mater.* **2013**, (1), 011002.

Appendix B Additional Information for Chapter 3: Low Temperature CO Oxidation over Rh Supported on N-Doped Carbon

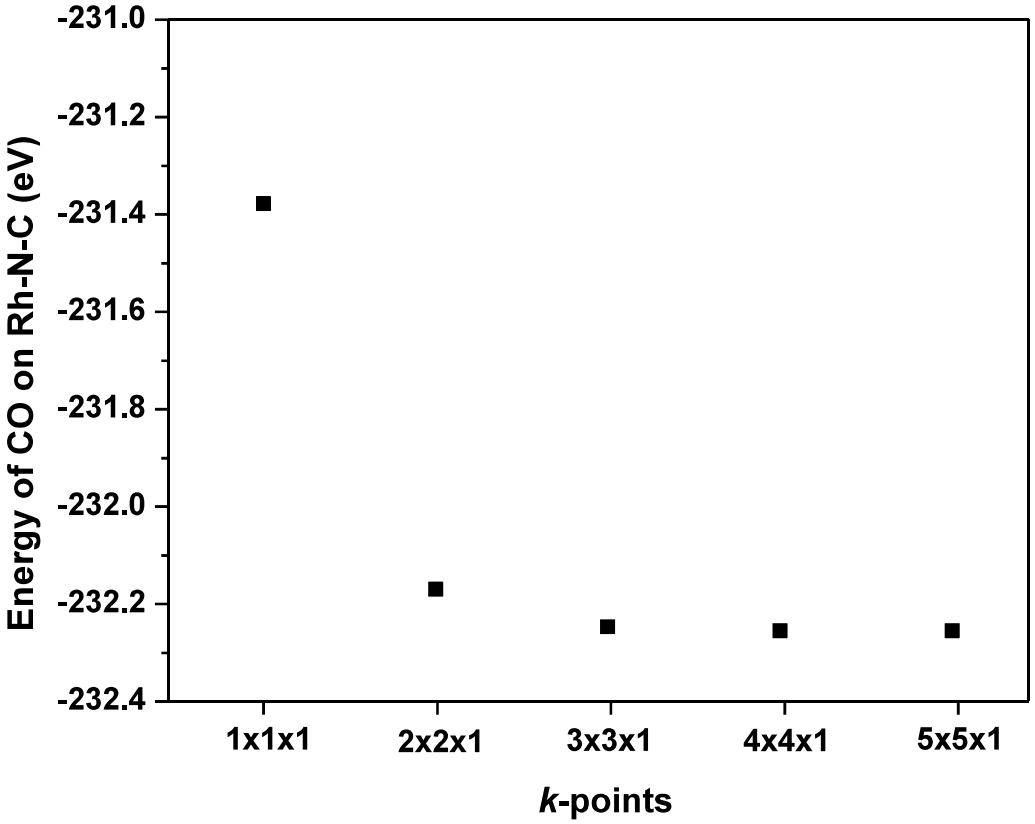

Appendix Fig. B1. Optimization of the Monkhorst-Pack *k*-point mesh for the small-cell (higher density of M) using vdW-DF.

Appendix Table B1. Comparison of Binding Energy for CO and O_2 from our PBE calculations versus PBE literature values

Element		Binding Energy	Literature Binding Energy[1]
Ag	BE_{CO}	0	0
	BE_{O2}	-13	-9
Au	BE_{CO}	-1	-1
	BE_{O2}	-22	-14
Co	BE_{CO}	-73	-77
	BE_{O2}	-61	-69
Cr	BE_{CO}	-90	-105
	BE_{O2}	-182	-198
Cu	BE_{CO}	0	-1
	BE_{O2}	-8	-10
Fe	BE_{CO}	-146	-78
	BE_{O2}	-73	-94
Ir	BE_{CO}	-104	-114
	BE_{O2}	-40	-48
Mn	BE_{CO}	-102	-108
	BE_{O2}	-124	-130
Ni	BE_{CO}	-1	-2
	BE_{O2}	-6	-7
Pd	BE_{CO}	-1	-1
	BE_{O2}	-5	-4
Pt	BE_{CO}	-1	-2
	BE_{O2}	-4	-4
Rh	BE_{CO}	-73	-82
	BE_{O2}	-54	-57
Ru	BE_{CO}	-262	-260
	BE_{O2}	-177	-171

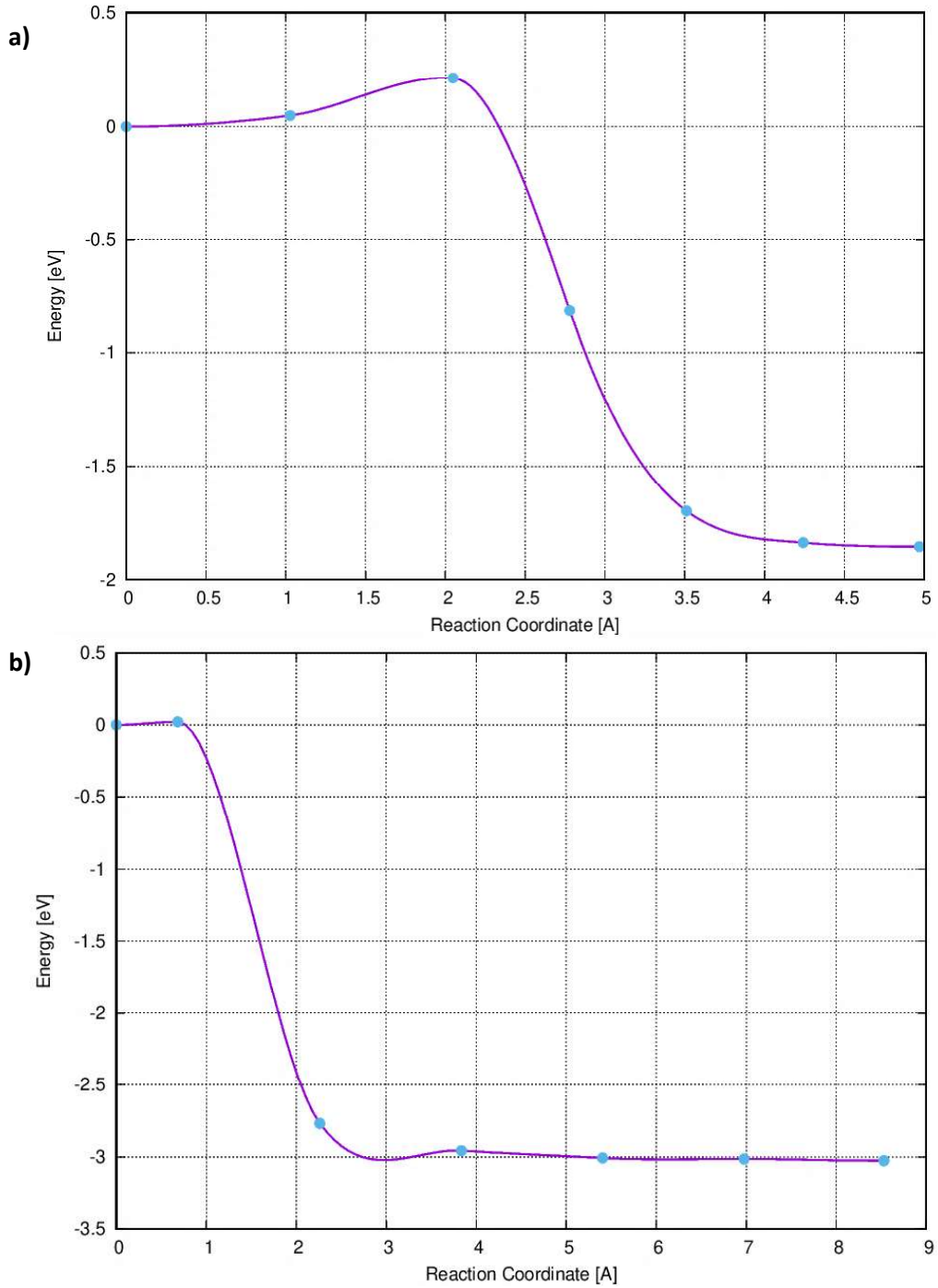

Appendix Fig. B2. Climbing image nudged elastic band calculations for TS1 and TS2.
Plots for CI-NEB for TS1 (a) and TS1 (b). a and b were calculated with vdW-DF and NUPDOWN set to 0.

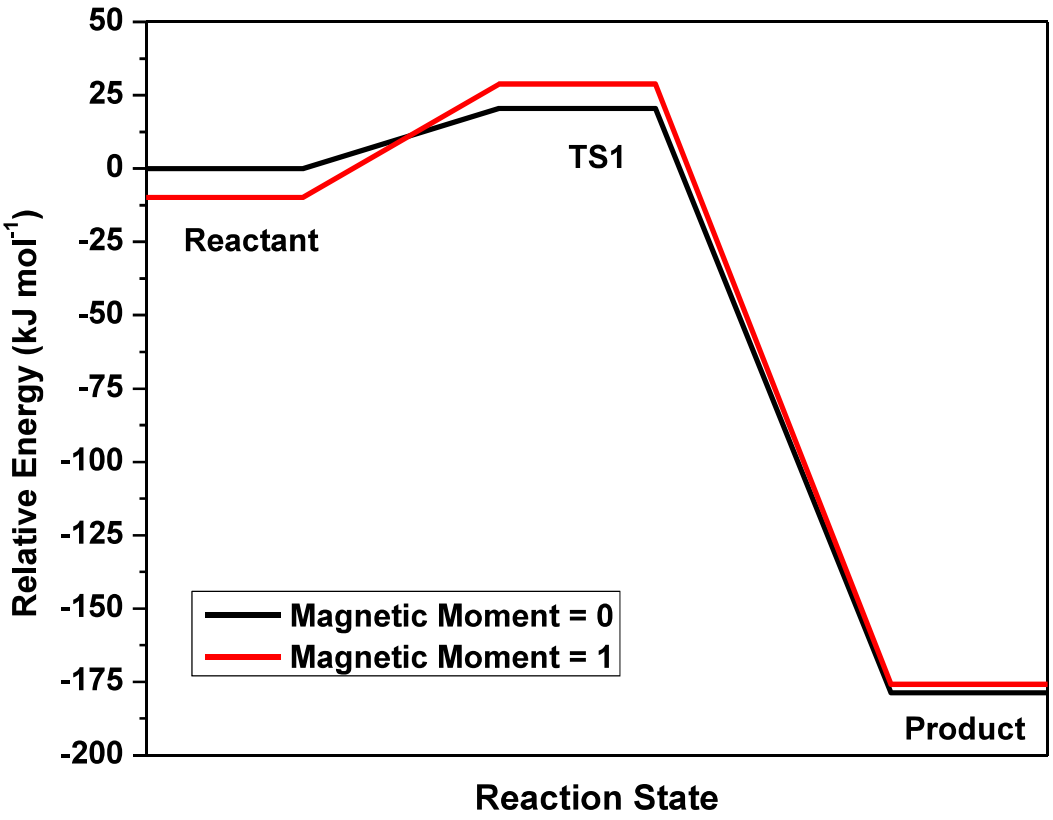

Appendix Fig. B3. Spin optimization for CI-NEB 1.
Geometry optimization of the reactant and product state with a magnetic moment of 0 or 1 for the CI-NEB were presented in Appendix Fig. B2 a. All of the points for the reaction states are relative to the reactant energy with a magnetic moment of 0.

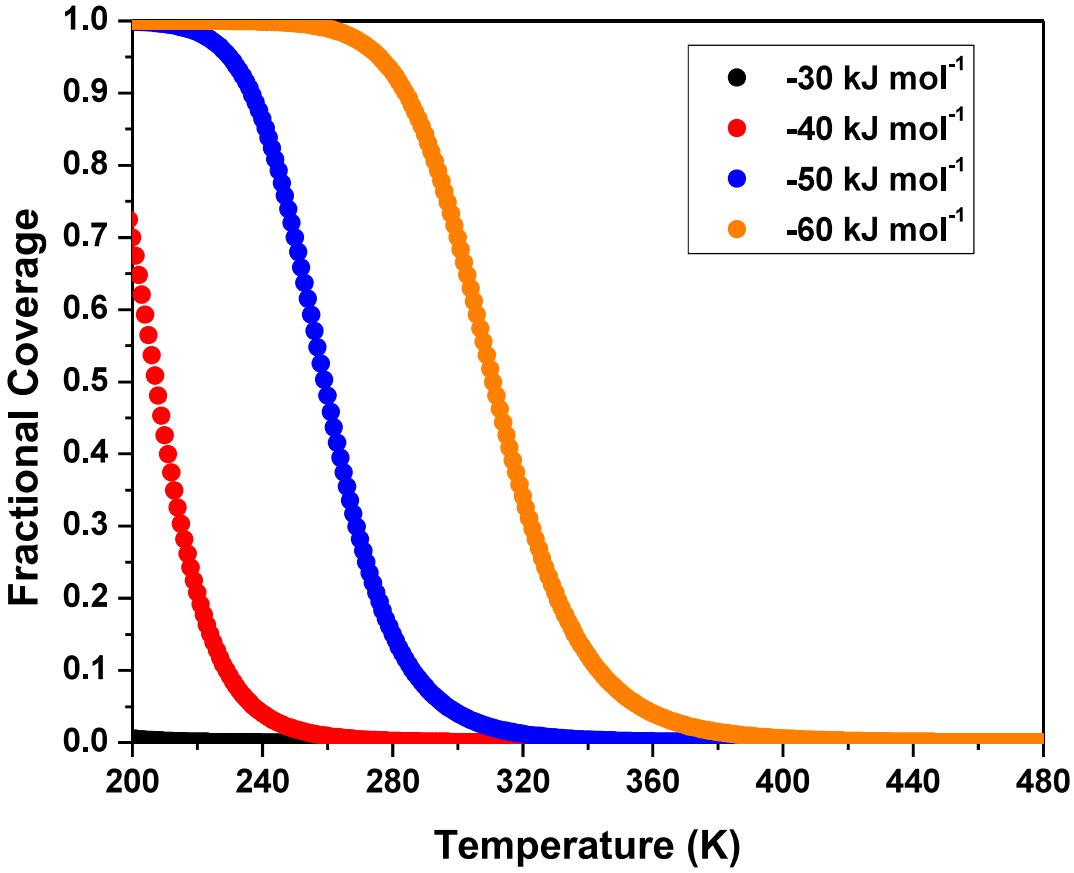

Appendix Fig. B4. Coverage of CO plotted as a function of temperature based on theoretical binding energy.

Pressure was fixed at 1 bar and the standard entropy of adsorption was assumed to be -0.19 kJ mol^{-1}. Previous reports on variation in the binding energy based on functional choice led us to expand our criterion by 10 kJ mol^{-1}, indicating that -30 kJ mol^{-1} would be the cutoff for binding energy of adsorption of CO.[2]

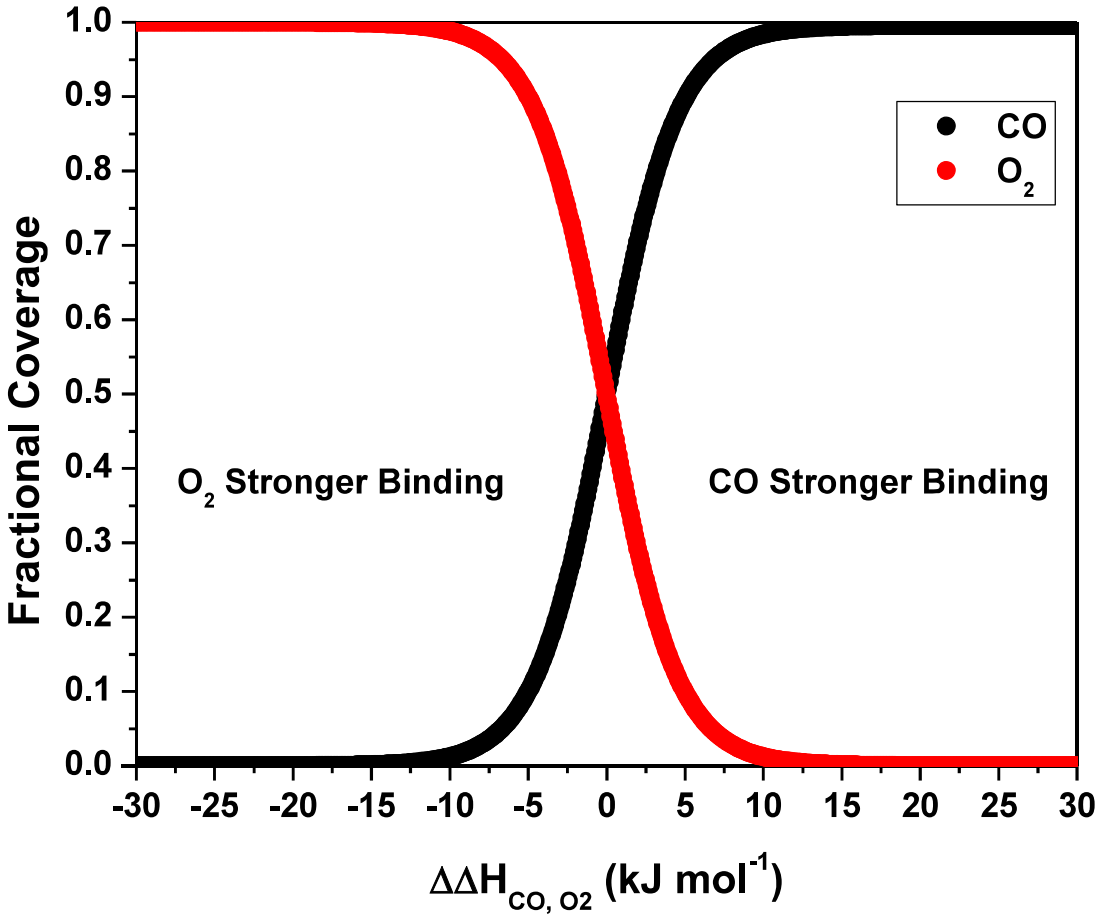

Appendix Fig. B5. Coverage of CO and O_2 as a function of the difference in enthalpy of binding energy.

The $\Delta\Delta H_{CO,O2}$ term is defined as $\Delta H_{O2} - \Delta H_{CO}$ where ΔH_{CO} is fixed at -67 kJ mol^{-1} and the binding energy of O_2 is varied. The temperature is set at 273 K with pressures of CO and O_2 each set to 1 bar. The standard entropy of adsorption is assumed to be -0.19 kJ mol^{-1}. This analysis combined with previous reports for ~10 kJ mol^{-1} variation in the binding energies based on functional and cell size suggest -30 kJ mol^{-1} would be the cutoff for the difference in O_2 and CO binding energies.[2]

Cr		Mn		Fe		Co		Ni		Cu		Zn		Ga	
CO	2.0	CO	1.1	CO	0.1	CO	0.7	CO	0	CO	1.1	CO	0	CO	0.3
O_2	2.0	O_2	3.0	O_2	1.8	O_2	1.1	O_2	1.9	O_2	2.8	O_2	1.5	O_2	1.0
Magnetic States from vdW-DF optimizations				Ru		Rh		Pd				Cd			
				CO	0	CO	0	CO	0			CO	0		
				O_2	-1.3	O_2	1.0	O_2	1.8			O_2	1.3		
						Ir		Pt		Au					
						CO	0	CO	0	CO	0				
						O_2	1.0	O_2	1.8	O_2	1.7				

Appendix Fig. B6. Magnetic states of Rh during calculations of CO and O_2 binding energy.

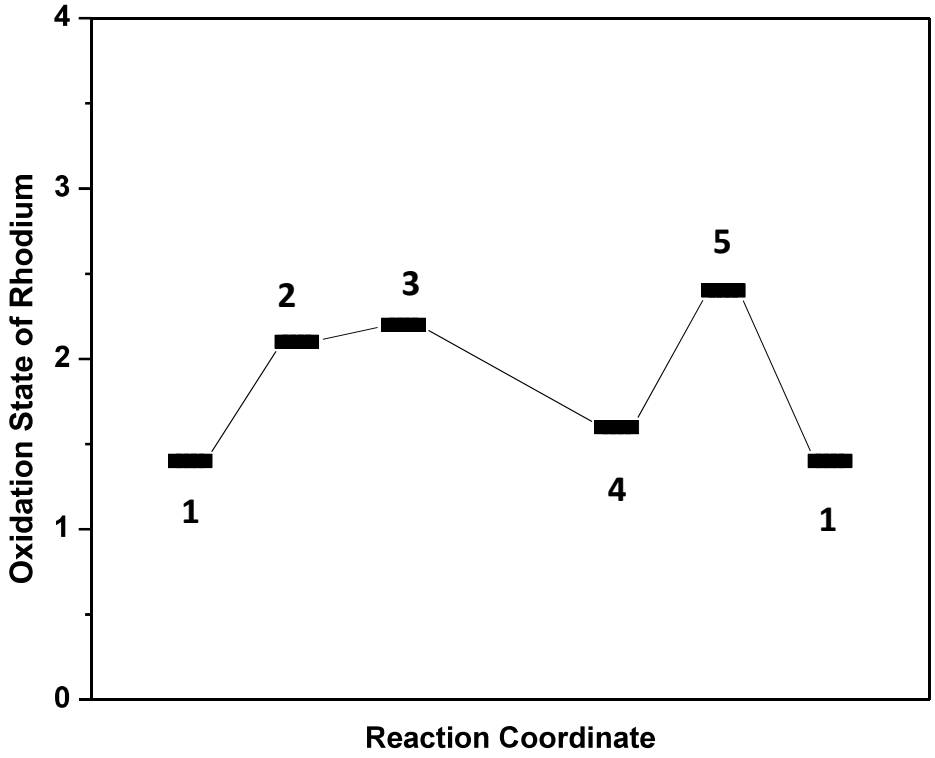

Appendix Fig. B7. Bader charges plotted over the reaction coordinate in Fig. 3.4.
The Bader charges were computed using the method developed by Henkelman et al.[3, 4] An interpolation was conducted between Rh metal, carbonylchlorobis(triphenylphosphine)rhodium (Rh 1+)[5], and Rh 3+ from Rh oxide in the Materials Project database.[6] These points were fit and the oxidation states were referenced to the curve.

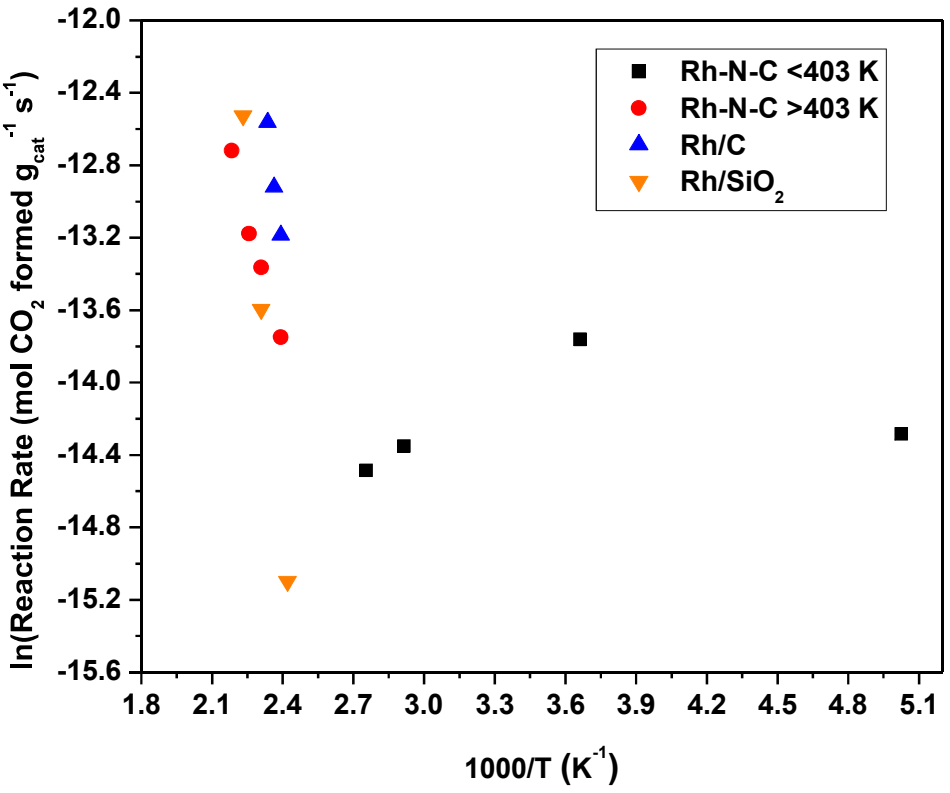

Appendix Fig. B8. Arrhenius-type plots for CO oxidation on various Rh-containing catalysts. The reaction was run with 0.2 g of catalyst diluted in SiC and with 160 cm^3 total flow, 1 % CO, 2 % O_2, and balance He at 3 atm. The O_2 and CO were purified with silica traps in a dry-ice acetone bath while the He was purified with an OMI filter. All of the points were collected at steady-state and were collected by alternating between low and high temperature.

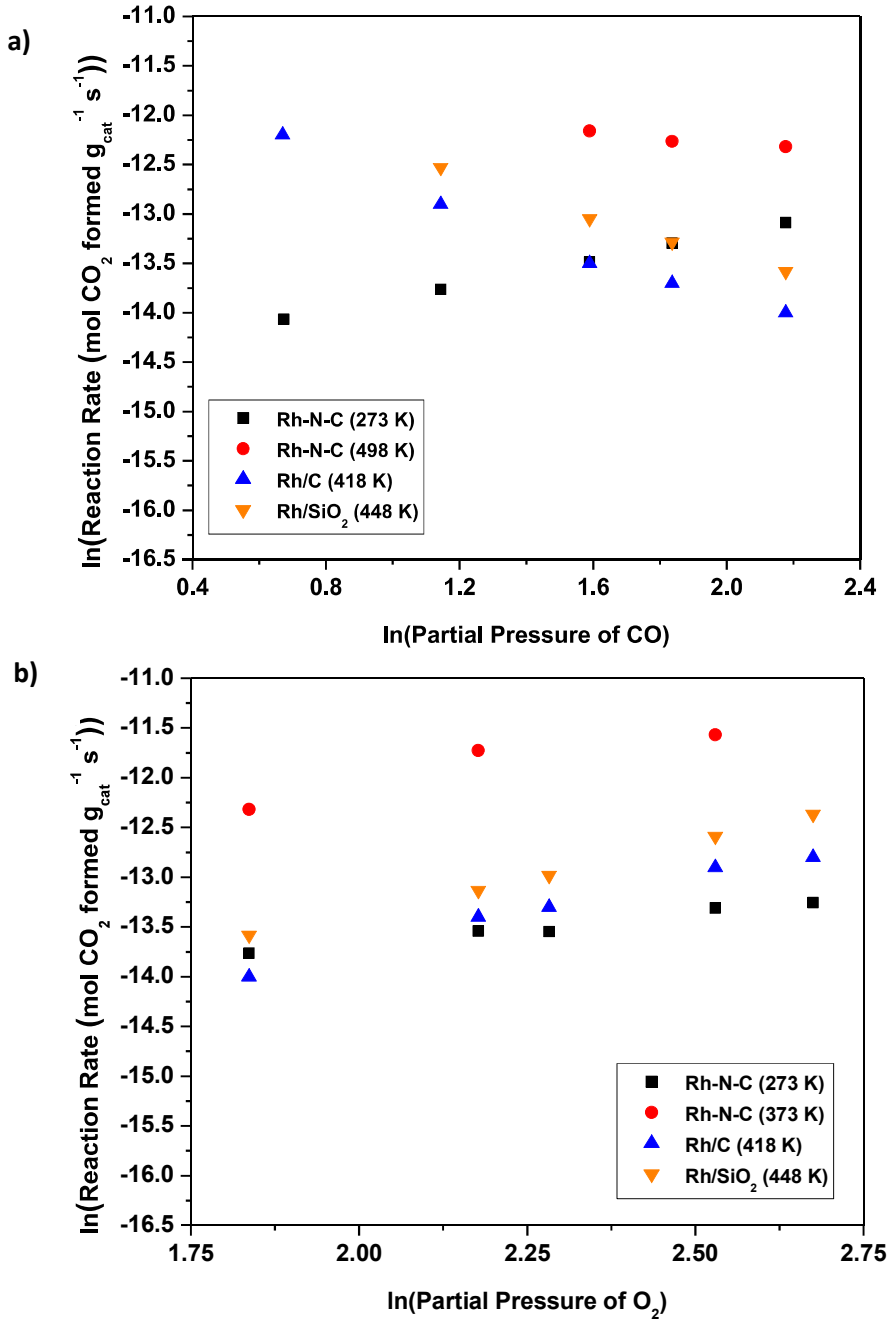

Appendix Fig. B9. Reaction order plots for both CO and O_2 on various Rh-containing catalysts during the CO oxidation reaction.

a) Plot of the effect of the partial pressure of CO on the reaction rate for various Rh containing catalysts by varying the partial pressure (2.0 to 8.8 kPa) of CO and holding the O_2 constant at 6.3 kPa

b) Plot of the effect of the partial pressure of O_2 on the reaction rate for various Rh containing catalysts by varying the partial pressure (6.3 to 14.5 kPa) of O_2 and holding the CO constant

at 8.8 kPa for all catalysts except the Rh-N-C which collected at 3.1 kPa. The temperatures were adjusted to give < 40 % conversion.

References

1. Kropp, T.; Mavrikakis, M., Transition Metal Atoms Embedded in Graphene: How Nitrogen Doping Increases CO Oxidation Activity. *ACS Catal.* **2019** (9), 6864-6868.

2. Whitcomb, C. A.; Sviripa, A.; Schapowal, M. I.; Mamedov, K.; Unocic, R. R.; Paolucci, C.; Davis, R. J., Mechanistic Insights on the Low-Temperature Oxidation of CO Catalyzed by Isolated Co Ions in N-Doped Carbon. *ACS Catalysis* **2022,** *12* (24), 15529-15540.

3. Tang, W.; Sanville, E.; Henkelman, G., A Grid-Based Bader Analysis Algorithm Without Lattice Bias. **2009,** *21*.

4. Sanville, E.; Kenny, S. D.; Smith, R.; Henkelman, G., Improved Grid-Based Algorithm for Bader Charge Allocation. *J. Comp. Chem.* **2007**, *28* (5), 899-908.

5. Shimizu, Y.; Mitsuhashi, H.; Caspi, E., A New Practical Synthesis of 1-dehydro-3-keto Steroids of the A/B Cis Series. *Tetrahedron Lett.* **1966,** *7* (34), 4113-4116.

6. Jain, A.; Ong, S. P.; Hautier, G.; Chen, W.; Richards, W. D.; Dacek, S.; Cholia, S.; Gunter, D.; Skinner, D.; Ceder, G.; Persson, K. A., Commentary: The Materials Project: A Materials Genome Approach to Accelerating Materials Innovation. *APL Mater.* **2013**, (1), 011002.

Appendix C Additional Information for Chapter 4: Aerobic Oxidation of 2-Propanol Over Co Containing Catalysts

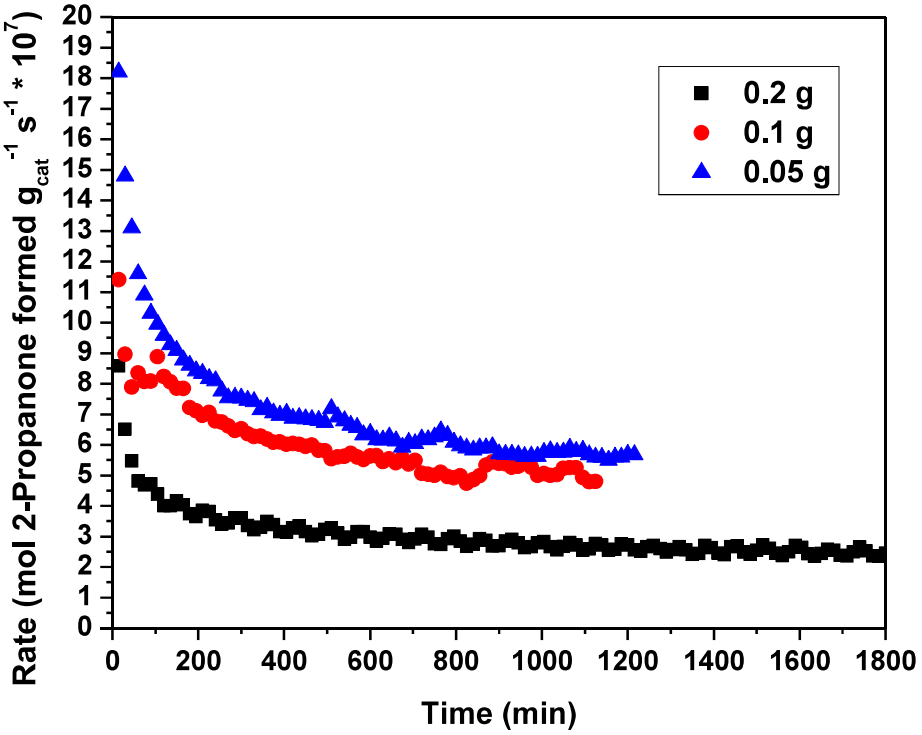

Appendix Fig. C1. Rates of reaction for the gas phase oxidative dehydrogenation of 2-propanol over various reactor loadings of Co-N-C.
Each catalyst was thermally treated in He at 673 K before starting the reactor upon cooling to 473 K and switching the gas flow to the reactants. The reaction was run with the reported amount of catalyst diluted in SiC with 43 cm^3 min^{-1} total gas flow, 6.7 % 2-propanol, 14 % O_2, and balance He at atmospheric pressure. The selectivity was > 95 % to 2-propanone throughout the run.

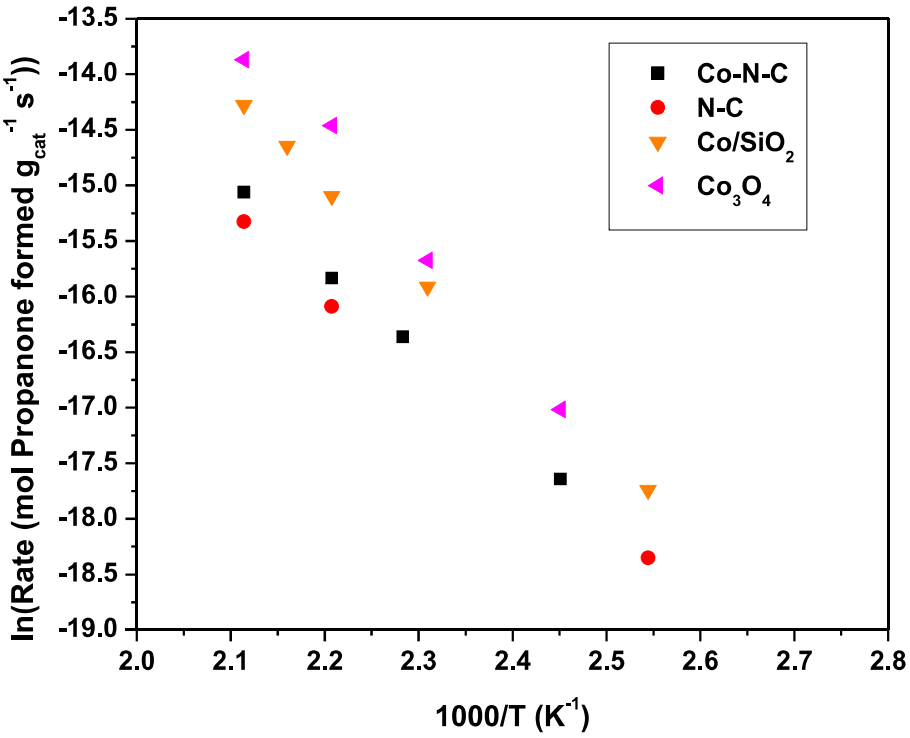

Appendix Fig. C2. Arrhenius-type plots for the gas phase oxidative dehydrogenation of 2-propanol on various Co-containing catalysts.

The reaction was run with 200 mg of catalyst diluted in SiC and with 43 cm^3 min^{-1} total flow, 6.7 % 2-propanol, 14 % O_2, 72.3 % N_2, and balance He at atmospheric pressure. The He was purified with an OMI Filter. All points were collected once steady state was reached at each temperature. Points were collected at alternating high and low temperatures.

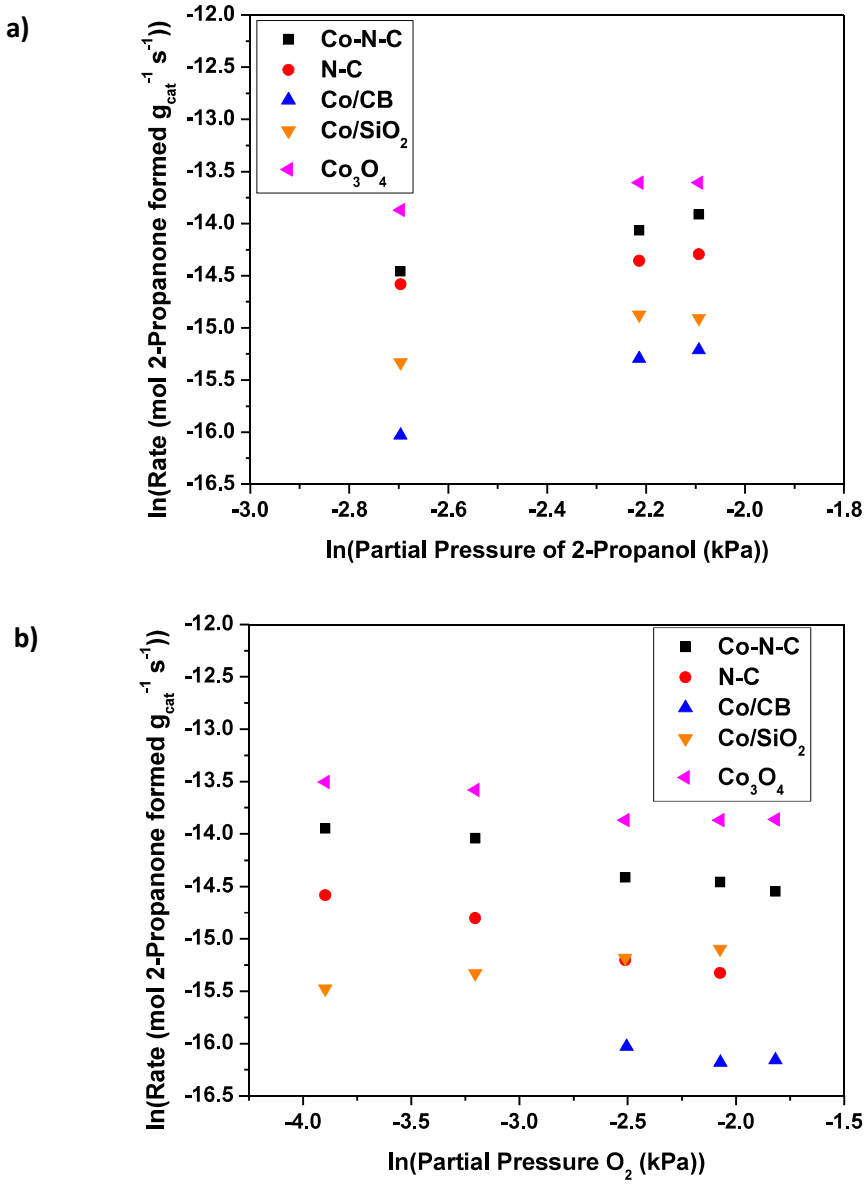

Appendix Fig. C3. Reaction order plots for both gas phase reactants on various Co-containing catalysts.

a) Plot of the effect of the partial pressure of 2-propanol (from 6.8 to 12.5 kPa) on the reaction rate for various Co and containing and control catalysts while holding the partial pressure of O_2 constant at 12.6 kPa. b) Plot of the effect of the partial pressure of O_2 (from 2.0 to 16.4 kPa) on the reaction rate for various Co containing and control catalysts while holding the partial pressure of 2-propanol constant at 6.7 kPa. The temperature was kept constant at 473 K.

a)

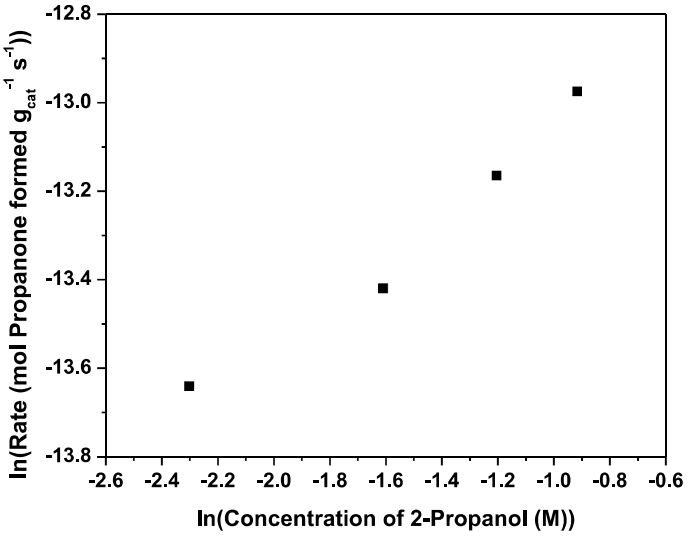

b)

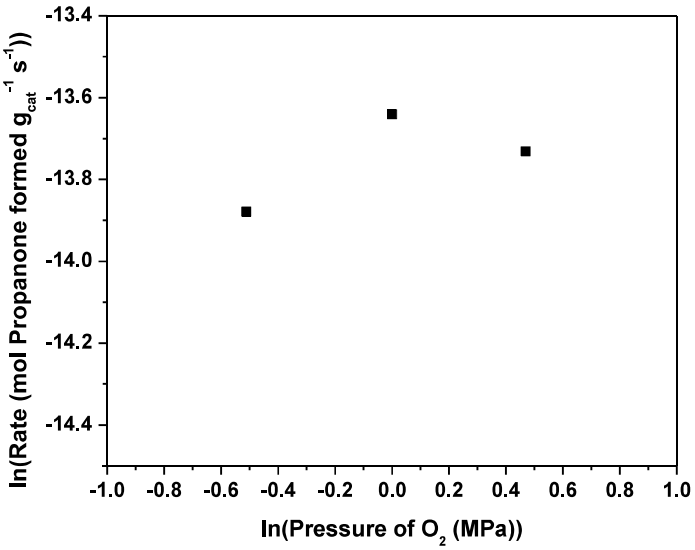

Appendix Fig. C4. Reaction order plots for both reactants on Co-N-C in the liquid phase.
a) Plot of the effect of the concentration of 2-propanol (0.1 to 0.4 M) on the reaction rate for various Co and containing and control catalysts while holding the pressure of O_2 constant at 1 MPa. b) Plot of the effect of the pressure of O_2 (0.6 MPa to 1.6 MPa) on the reaction rate for various Co containing and control catalysts while holding the concentration of 2-propanol constant at 0.1 M. The temperature was kept constant at 388 K.